UNLOCKING LOW-POWER STIMULATED EMISSION DEPLETION SUPER-RESOLUTION MICROSCOPY BY USING UPCONVERSION NANOCRYSTALS

By

Yujia Liu

Department of Physics and Astronomy

Supervisors:

Prof. James A. Piper,

Dr. Yiqing Lu

MACQUARIE University
SYDNEY·AUSTRALIA

FACULTY OF SCIENCE AND ENGINEERING

This thesis is presented for the degree of Doctor of Philosophy

October 2017

I certify that the work in this thesis has not previously been submitted for a degree nor has it been submitted as part of requirements for a degree to any other university or institution other than Macquarie University.

I also certify that the thesis is an original piece of research and it was authored by myself. Help and assistance that I have received in the course of my research work and in the preparation of the thesis itself has, where appropriate, been acknowledged.

In addition, I certify that all information sources and literature used in the course of this research is also indicated where appropriate in this record of my thesis.

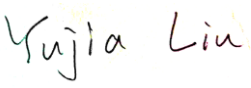

Yujia Liu 18-Oct-2017

Acknowledgements

I spent seven years in three universities for my PhD, 2 years in Shanghai Jiao Tong University, 2.5 years in Peking University and 2.5 years in Macquarie University as a Cotutelle PhD student.

During the seven years, I had been supervised by five supervisors, Jim Piper, Dayong Jin and Yiqing Lu from Macquarie University and Qiushi Ren, Peng Xi from Shanghai Jiao Tong University originally. Firstly, I do want to thank all these five supervisors for their kindly support during my PhD. I feel so lucky to have such five great mentors and very grateful to them for their enormous efforts on guiding me throughout my PhD study to reach the completion of this thesis. This thesis – and even my PhD program at Macquarie – would not have been possible without them. Jim is a professor of great personal charisma, always considerate, patient and encouraging. He has been always inspiring and supportive to me. I really appreciate his sincere help and thoughtful suggestions on my PhD program and on my life. Jin is a strongly self-motived person that I learned a lot from him. I have learned much from observing him how to manage and run the group, build up the network, and treat and train the students. I thank him to share the philosophy and experiences of tackling the difficulties and maximizing the opportunities. Lu has been both a friend and a supervisor to me. Actually when I joined Macquarie, he was in his final year for his PhD here and we had so many collaborations on different projects to prove our ideas. I'll always remember the shared experience. Qiushi Ren and Peng Xi are two humble experts and I respect very much on their support for my Cotutelle programme.

I have received a lot of support from many people during my PhD candidature. In particular, I want to thank Xianlin Zheng, Jie Lu, Jiangbo Zhao, Deming Liu, Run Zhang, Xavier Vidal, Shihui Wen, Fan Wang, Chenshuo Ma as well as other peers from our group of Adcanced Cytometry Labs and CNBP @ MQ. I had wonderful teamwork experiences with them. Many Macquarie colleagues, including Wei Deng, Jipeng Lin and others, gave me many valuable academic advice. Walther Adendorff, Benny Wang and other people from METS assisted me with many parts for my system. I also want to thank our collaborators, the Peking University group and Olympus people. Their knowledge and

experience added great value to my projects. I sincerely appreciate the generous help from all these nice people.

I am glad to acknowledge the financial support I have received from Macquarie University, Shanghai Jiao Tong University and Peking University. Their support offered me many opportunities to expand my research experiences.

I present the special acknowledgements to my parents and relatives. Your love and support helped me over the downtime. I would never have walked here without your efforts.

Finally, I'd like to thank my wife, Yang Li for her backing up over years during my PhD time. I always feel so lucky to have you in my life.

List of Publications

[1] **Liu Y**, Ding Y, Alonas E et al, Achieving λ/10 resolution CW STED nanoscopy with a Ti: Sapphire oscillator[J]. *PloS ONE*, 2012, 7(6): e40003.

I led the major experimental work, including system design and setup, alignment and evaluation, and data acquisition.

[2] **Liu Y**, Lu Y, Yang X, et al. Amplified stimulated emission in upconversion nanoparticles for super-resolution nanoscopy[J]. *Nature*, 2017, doi:10.1038/nature21366.

I did major contributions to this work, including building the dual-laser confocal/STED system, coordinating sample preparation, conducting major optical experiments, and participating in data analysis, preparation of the manuscript and figures.

[3] Lu Y, Zhao J, Zhang R, Liu Y et al, Tunable lifetime multiplexing using luminescent nanocrystals[J]. *Nature Photonics*, 2014, 8(1): 32-36.

My contribution to the paper is to design and setup a single nanocrystal lifetime measurement confocal microscope, and to demonstrate the lifetime decoding on the selected Tm/Yb doped nanocrystals.

[4] Zhao J, Jin D, Schartner EP, Lu Y, Liu Y et al, Single-nanocrystal sensitivity achieved by enhanced upconversion luminescence[J]. *Nature Nanotechnology*, 2013, 8(10): 729-734.

My contribution to this project is centred on the demonstration of security inks using upconversion nanocrystals. In detail, I managed to inject upconversion nanocrystals into the commercial ink cartridges to mix thoroughly with the pigment, and design the security patterns to precisely print them on paper. I laminated the paper samples and mounted them on glass slides, and performed image scanning using the orthogonal scanning automated microscope (OSAM) developed in our group

([1]-[4] are closely related to my PhD program)

[5] Xie H, **Liu Y**, Jin D et al, Analytical description of high-aperture STED resolution with 0–2π vortex phase modulation[J]. *JOSA A*, 2013, 30(8): 1640-1645.

[6] Wang W, **Liu Y**, Xi P et al, Origin and effect of high-order dispersion in ultrashort pulse multiphoton microscopy in the 10 fs regime[J]. *Applied Optics*, 2010, 49(35): 6703-6709.

[7] Yang X, Xie H, Alonas E, **Liu Y** et al, Mirror enhanced axial narrowing super-resolution microscopy[J]. *Light: Science and Applications*, 2016, 5(6): e16134..

[8] Yang X, Tzeng YK, Zhu Z, Huang Z, Chen X, **Liu Y** et al, Sub-diffraction imaging of nitrogen-vacancy centers in diamond by stimulated emission depletion and structured illumination[J]. *RSC Advances*, 2014, 4(22): 11305-11310.

([5]-[8] are from other projects during my PhD candidature)

Abstract

Optical microscopy capable of real-time 3-dimentional imaging for live cells has facilitated modern biological research, especially with the recent development of a series of novel super-resolution techniques that overcome the diffraction limit associated with conventional optical microscopes. Among them, stimulated emission depletion (STED) nanoscopy is the first and optically most straightforward method to effectively break the resolution barrier for far-field microscopes. It has been demonstrated that STED can achieve 3-D imaging even at video rate. However the very high optical intensities required for depletion remain a key challenge for STED to be applied to live biological cells and tissues.

This thesis explores the potential to use luminescent probes with long decay lifetimes to lower the optical depletion intensity requirement in STED. In particular, lanthanide-doped upconversion nanomaterials involving multiple intermediate excited states with lifetimes on the microsecond-to-millisecond timescale have been investigated. Such materials have found broad applications in biosensing and imaging due to their unique feature of non-photobleaching and non-photoblinking. Here, their photon upconversion process and depletion capability have been carefully studied, in order to apply them to achieve STED super-resolution imaging at lowered intensity. The thesis is composed of the following research:

Firstly, a continuous-wave STED (CW STED) microscope based on a Ti:Sapphire oscillator was established to achieve ~71 nm super-resolution on 20 nm fluorescent nanoparticles. Three components of cellular skeleton and RNA were imaged in fixed cells with super-resolution. This result shows that the CW mode operation reduces the system complexity and cost; however, it cannot relieve the extreme intensity requirement in STED to achieve super resolution for live cell imaging.

Secondly, we explored and realized super-resolution imaging via an intermediate-level depletion mechanism using $NaYF_4$:Yb^{3+}/Tm^{3+} upconversion nanocrystals. Measurement of the depletion efficiency from upconversion nanocrystals with variable doping concentrations showed that the saturation intensity reduces substantially at increased Tm^{3+}

doping concentration. In comparison to conventional organic dyes, the depletion intensity requirement for 8% Tm^{3+}-doped samples is reduced by two orders of magnitude, allowing us to achieve moderate super-resolution on these highly-doped samples at much lower depletion intensities.

Thirdly, the mechanism underpinning efficient depletion on highly doped upconversion nanocrystals was studied in detail. We found that the Tm-Tm cross-relaxation rates in the Yb-Tm photon upconversion system increase significantly at high Tm doping concentration. This leads to a photon-avalanche-like process to efficiently establish population inversion on the intermediate excited levels, enabling amplified stimulated emission to depletion/inhibit upconversion luminescence using largely reduced intensity. Meanwhile, for low doping concentration samples, the cross-relaxation rates are not sufficient to achieve photon-avalanche-enhanced stimulated emission depletion.

The results embodied in this thesis demonstrate the capability to achieve low-power operation of STED using upconversion nanocrystals for super-resolution imaging for live cells. It suggest that novel luminescence nanoprobes may hold the key to next-generation optical nanoscopy. We further explored the lifetime tunability of upconversion nanocrystals for multiplexed imaging and molecular localization at high throughput, with preliminary results suggesting that upconversion nanoparticles with the same emission wavelengths can be effectively distinguished based on lifetime coding. It is expected that the new bio-friendly upconversion-STED method may find broad applications in life sciences.

Key words: optical super-resolution microscopy, stimulated emission, lanthanide, upconversion nanoparticles, photon avalanche

Contents

List of Acronyms (in Alphabetic Order)

AFM	Atomic Force Microscope
APD	Avalanche PhotoDiode
CLSM	Confocal Laser Scanning Microscope
CR	Cross Relaxation
CW STED	Continuous Wavelength STimulated Emission Depletion
FCS	Fluorescence Correlation Spectroscopy
FPALM	Fluorescence Photo-Activated Localization Microscopy
FRET	Fluorescence Resonance Energy Transfer
FSM	Fluorescent Speckle Microscopy
FWHM	Full-Width at Half-Maximum
GSD	Ground State Depletion
HEp2	Human Epidermoid carcinoma strain-2
hRSV	human Respiratory Syncytial Virus
HWP	Half-Wave Plate
I^5M	Incoherent Interference Illumination Image Interference Microscopy
LSM	Light Sheet Microscopy
LSFM	Light Sheet Fluorescence Microscopy
MMF	Multi-Mode Fiber
MOI	Multiplicity Of Infection
NA	Numerical Aperture
OA	Oleic Acid
PALM	Photo-Activated Localization Microscopy
PA	Photon Avalanche

PBS	Phosphate-Buffered Saline
PDT	PhotoDynamic Therapy
PSF	Point Spread Function
PMF	Polarization-Maintaining Fiber
PMT	PhotoMultiplier Tube
QWP	Quarter-Wave Plate
RESOLFT	REversible Saturable OpticaL Fluorescence Transitions
R-L Algorithm	Richardson-Lucy Algorithm
RNA	RiboNucleic Acid
SA	StreptAvidin
SEM	Scanning Electron Microscope
SIM	Structured-Illumination Microscopy
SLO	StreptoLysin O
SMF	Single-Mode Fiber
SNOM	Scanning Near-field Optical Microscope
SSIM	Saturated Structured-Illumination Microscopy
STED	STimulated Emission Depletion
STM	Scanning Tunneling Microscope
STORM	STochastic Optical Reconstruction Microscopy
TEM	Transmission Electron Microscope
TPE	Two-Photon Excitation
UCNPs	Up-Conversion Nano-Particles
VPP	Vortex Phase Plate

Chapter 1: Introduction

This thesis focuses on the development of novel super-resolution microscopy incorporating advanced rare-earth dopant upconversion luminescence material in the spatial and temporal domain. By exploiting a phenomenon akin to photon avalanche in highly doped $NaYF_4$:Yb,Tm nanocrystals, the blue (455 nm) upconversion emission of Tm^{3+} can be substantially suppressed by illumination with a stimulated emission depletion beam at a wavelength targeting an intermediate state in the Tm^{3+} upconversion process. This enables super-resolution microscopy by way of a new form of stimulated emission depletion, in the process solving a key challenge of the current STED super-resolution techniques by significantly alleviating the depletion intensity requirement.

This chapter provides an overview of advanced fluorescent microscopy techniques. It covers the motivations, fundamental knowledge and key advantages of using lanthanide-based luminescent nanocrystals as nanoscopy probes, and an up-to-date review of progress in the related areas of the super-resolution nanoscopy including instrumentation and applications. A brief introduction to fluorescent molecular probes and luminescent nanoparticles is given, with a focus on upconversion nanocrystals and the concept for STED-based super-resolution using lanthanide-doped nanomaterials. A detailed thesis outline is provided at the end of this chapter.

1.1 Optical Microscopy

1.1.1 Optical Fluorescent Microscopy

Following the previous developments of wide-field optical microscopy by Zeiss and Abbe some 150 years ago[1], optical microscopy has become an indispensable tool of modern biology. Current generation optical microscopy plays a fundamental role in studies of biological cells and subcellular components including location and detection of functional targets, with a plethora of applications investigating the positions, movements,

and interactions of cellular elements.

A wide range of other instruments for high resolution imaging like Electron Microscopy (EM)[2,3], Atomic Force Microscopy (AFM)[4] and Scanning Force Microscopy (SFM)[5], have also been developed over past decades. Some of these can achieve resolution on the order of fractions of a nanometre. But the limitations of these high resolution imaging methods are also as well known, arguably the most important being the inability to image live cells due to the destructive nature of specimen preparation[6]. Though new development on EM could achieve live cell imaging, the method could not be widely applied[7,8].

In contrast to these techniques, far-field optical microscopy provides ease of use. Moreover there are almost no restrictions on the specimen because visible light passes through biological tissue with low scattering and absorption loss and without changing the sample. However, the major force behind its dominance in life sciences is the invention of immuno-labeling with fluorescent dyes and the subsequent discovery of 'native' expression of fluorescent proteins inside cells[9]. The greatest advantage achieved here is the high selectivity of observable targets and regions of interest. By using a specific binding antibody or DNA/RNA probe, nearly every region of interest inside a cell can be 'colored' with fluorescent markers[10]. In the case of fluorescent proteins, an additional DNA sequence, a plasmid, allows cells to express a target protein, tagged with a fluorescent protein[11]. Fluorescent markers, molecules which can emit light when excited by particular wavelengths, provide very large signal to noise ratio due to the Stokes shift of the emission wavelength with respect to the excitation wavelength. The combination of these techniques with optical microscopy provides a superior tool with diffraction limited resolution of 200 nm and high selectivity of observable structures[1,12,13]. However, since a lot of the details of interest inside the cell are of a scale less than the diffraction limit, increasing the resolving power of optical fluorescence microscopes has been a hot topic.

So considering all available imaging techniques, far-field fluorescent optical microscopy has become the most widely used for real-time bioanalysis in live cell imaging in modern biological research[14].

1.1.2 Resolution Challenge in Far-Field Optical Microscopy

As mentioned above, though optical microscopy is the most widely used in biological research, its usage for study of very small structures is constrained by what is known as the resolution limit.

In principle, the resolution limit in optical microscopy is due to the fundamental phenomenon in physics called diffraction. Diffraction refers to various phenomena which occur when a wave encounters an obstacle or a slit. In classical physics, the diffraction phenomenon is described as the interference of waves according to the Huygens Fresnel principle. These characteristic behaviors are exhibited when a wave encounters an obstacle or a slit that is comparable in size to its wavelength. Similar effects occur when a light wave travels through a medium with a varying refractive index, or when a sound wave travels through a medium with varying acoustic impedance. Diffraction occurs with all waves, including sound waves, water waves, and electromagnetic waves such as light.

While diffraction occurs whenever propagating waves encounter such changes, its effects are generally most pronounced for waves whose wavelength is roughly comparable to the dimensions of the diffracting object or slit. If the obstructing object provides multiple, closely spaced openings, a complex pattern of varying intensity can result. The light has the property of both particle and wave. The wave property will naturally lead to diffraction phenomenon during transmission.

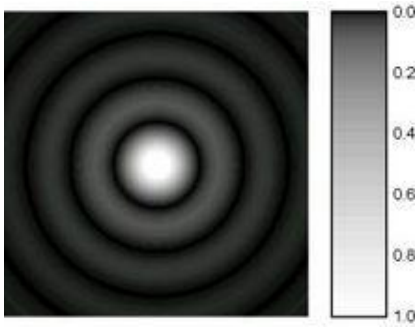

FIGURE 1-1 Optical diffraction pattern

So for light wave in optical microscopy, considering the objective as consisting of diffraction gratings, the object diffracts the illuminating light. And point light source will not

be focused into a point image on the image plane but appearing as an extended intensity distribution like a series of concentric rings, known as the Airy diffraction pattern, as shown in Fig 1-1. And this extended intensity distribution is called a “point spread function”, which actually presents the resolving power of an optical imaging system.

The spatial resolution of light microscopes is ultimately limited by diffraction. Diffraction prevents focusing a beam of light into a spot substantially smaller than half a wavelength in size. Similarly, diffraction causes the image of a point-like emitter, such as a single fluorescent molecule, to appear as an extended intensity distribution in the image plane. An image of an extended object taken with a fluorescence microscope is equivalent to the superposition of images of point sources composing the object. The image of a point source, the point-spread function (PSF), therefore describes the imaging properties of these linear systems. To form the observed image of an object, every point of the object is blurred to have a shape given by the PSF, and the size of the PSF describes the resolution of an imaging system. This resolution is commonly defined by the full width at half maximum (FWHM) of the PSF. In the 19th century, E.Abbe described this effect analytically and defined the resolution limit as the minimal distance allowing for sub-diffraction points to be differentiated[1]. And according to Ernst Abbe's diffraction theory, the formula for maximum resolution of an optical far-field microscope can be described as follows:

$$r = \lambda / 2n\sin(\alpha) = \lambda / 2NA \tag{1.1}$$

where λ is the wavelength of light and NA is the numerical aperture of the utilized objective lens. The term NA = nsin(α) describes the maximal angle α of incident light which contributes to the focused light spot. Since the wavelength spectrum of visible light ranges from 380 nm up to 750 nm and the commonly utilized value of NA is 1.4, the resolution of an optical far-field light microscope is limited to ~200nm.

Nevertheless, in Abbe's first article on the microscope, he already anticipates the possibility of new developments that are not covered by his theory and that might enhance the resolving capabilities of optical microscopes beyond the limits that he derived. Driven by the need for high resolution imaging, a new generation of optical microscopy based on limited excitation or collection volume have emerged over the past 60 years[14,15].

1.2 Modern Far-field Microscopy

1.2.1 Confocal Microscopy

Invented by Minsky in 1955, the confocal optical microscope has rapidly become the most popular advanced microscope in biology due to its optical sectioning capability along z-axis[16]. A milestone in confocal microscopy development was the introduction of the confocal laser scanning microscope (CLSM) in the 1980s[17]. Lasers became readily available and were from then on used as high intensity excitation sources. In CLSM, scanning of the beam instead of the specimen led to a faster acquisition time and less artifacts due to vibration[18]. In comparison with the wide-field microscope, the confocal microscope no longer relies on cameras to get the image but use a scanning method for point fluorescent intensity and image reconstruction to get the final image, as shown in Fig 1-2.

In a confocal laser scanning microscope, a laser beam passes through a small circular aperture and then is focused by an objective lens into a small (ideally diffraction limited) focal volume within or on the surface of a specimen[18,19]. In biological applications especially, the specimen may be fluorescent. Scattered and reflected laser light as well as any fluorescent light from the illuminated spot passes back through the objective lens. A beam splitter separates off some portion of the light into the detection apparatus, which in fluorescence confocal microscopy will also have a filter that selectively passes the fluorescent wavelengths while blocking the original excitation wavelength. After passing through a pinhole, the light emitted from the sample is detected by a photo-detection device (usually a photomultiplier tube (PMT) or avalanche photodiode (APD)), transforming the light signal into an electrical signal that is recorded to give scan profiles, which can then be assembled to reconstruct the full image. The detector aperture obstructs the light that is not coming from the focal point, as shown by the dotted grey line in Fig 1-2. The out-of-focus light is suppressed: most of the returning light is blocked by the pinhole, which results in sharper images than those from conventional fluorescence microscopy techniques and permits one to obtain images of planes at various depths within the sample (sets of such images are also known as z stacks).

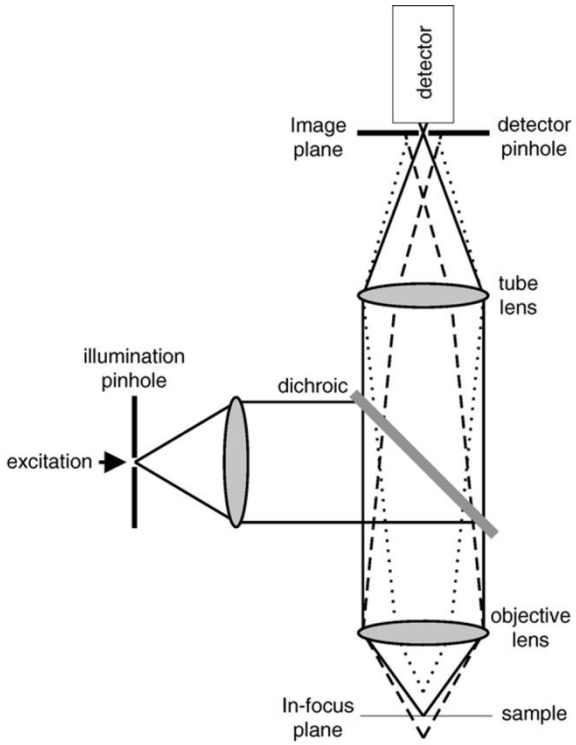

FIGURE 1-2 Schematic diagram of optical confocal fluorescent microscope: the solid line indicates the detection pathway and the dash line indicates the off-focus fluorescent pathway

As mentioned before, resolution in the microscope is directly related to the FWHM dimensions of the microscope's PSF, and it is common to measure this value experimentally in order to avoid the difficulty in attempting to identify intensity maxima in the Airy disk. In confocal fluorescence configurations, point-wise illumination scanning and point-wise detection are employed, so that only the fluorophores in the shared volume of the illumination and detection point spread functions are able to be detected. The intensity point spread function in the confocal case is, therefore, the product of the independent illumination intensity and detection intensity point spread functions. For confocal fluorescence, the lateral (and axial) extent of the point spread function is reduced by about 30 percent compared to that in the wide-field microscope. Because of the narrower intensity PSF, the separation of points required to produce acceptable contrast in the confocal microscope is reduced to a distance approximated by:

$$r_{lateral} = 0.41\lambda / NA \qquad (1.2)$$

Note the confocal resolution is $\sqrt{2}$ times better than for the wide field case, thus the

improvement of PSF for the confocal case is $1\text{-}1/\sqrt{2} \approx 30\%$ compared to widefield microscopy. A more detailed derivation of confocal microscopy resolution can be find on many classical optical textbooks and early published papers. For example, *L. Novotny and B. Hecht, Principles of Nano-Optics, Cambridge (2006),* in Chapter 4 ***Spatial resolution and position accuracy***, give an explicit analysis of resolution in confocal and wide-field microscopy.

A variety of equations are presented in the literature that pertain to different models for calculating axial resolution for various microscope configurations. Those most applicable to fluorescence emission are similar in form to the expressions evaluating depth of field, and demonstrate that axial resolution is proportional to the wavelength and refractive index of the specimen medium, and inversely proportional to the square of the numerical aperture. Consequently, the numerical aperture of the microscope objective has a much greater effect on axial resolution than does the emission wavelength. One equation commonly used to describe axial resolution for the confocal configuration is given below[20], with η representing the index of refraction, and the other variables as specified previously:

$$r_{axial} = 1.4\lambda \cdot \eta / NA^2 \tag{1.3}$$

Though the resolution of CLSM is enhanced compared to conventional wide field microscopes, the lateral resolution is still a few hundreds of nanometers and micron scale for z-axis[21]. The resolution is still not capable of resolving many sub-cellular structures of interest.

1.2.2 Multi-Photon Microscopy

Two-photon excitation microscopy (also referred to as non-linear, multiphoton, or two-photon laser scanning microscopy) employs two-photon absorption[22], a concept first described by Maria Goeppert-Mayer(1906–1972) in her doctoral dissertation in 1931[23,24], and first observed in 1961 in a CaF_2:Eu^{2+} crystal using laser excitation by Wolfgang Kaiser[25]. Isaac Abella showed in 1962 in cesium vapor that two-photon excitation of single atoms is possible[26].

The concept of two-photon excitation is based on the idea that two photons of

comparably lower energy than needed for one photon excitation can also excite a fluorophore in one quantum event. Each photon carries approximately half the energy necessary to excite the molecule. An excitation results in the subsequent emission of a fluorescence photon, typically at a higher energy than either of the two excitatory photons, as shown in Fig 1-3. At room temperature, two-photon absorption occurs on attosecond (10^{-18}s) time scale[27], and the probability of the near-simultaneous absorption of two photons is extremely low. Therefore a high flux of excitation photons is typically required, usually from a femtosecond laser[28].

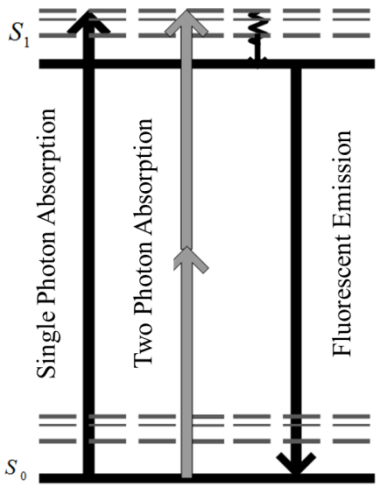

FIGURE 1-3 The Jablonski diagram of two photon excitation progress

The most commonly used fluorophores in biology have excitation spectra in the 400-500 nm range, whereas the laser used to excite the two-photon fluorescence lies in the ~700-1000 nm (infrared) range. The use of infrared light to excite fluorophores in light-scattering tissue has added benefits, for example, these lower-energy excitation photons are less likely to cause damage outside the focal volume. Compared to the confocal microscope, photon detection is much more effective since even scattered photons contribute to the usable signal in confocal microscopy. Due to the limitation of the excited volume, the PSF is substantially lower than that in single-photon excitation. As a result, the resolution is improved, allowing for thin optical sections to be cut.

Unfortunately, in practice the image resolution obtained with two-photon excitation is not better than that achieved in a well-aligned confocal microscope[29,30]. The utilization

of longer excitation wavelengths (such as red or infrared, instead of ultraviolet or blue), although an advantageous aspect of two-photon excitation, actually results in a larger resolution spot. So in theory the 2P microscopy should give a better sectioning result comparing to confocal microscopy while in practice they are roughly on the same level. If a biological structure can't be resolved in the confocal microscope, it will similarly not be resolved in a two-photon excitation laser-scanning microscope. While this point is well understood by microscopists experienced in these techniques, prospective users in the biomedical research community often assume that the advantages of two-photon excitation include increased resolution. And the so-called deeper penetration is not realized in practice either, since the anti-Stokes shift results in short wavelength emission which has poor transmission through biological tissue.

1.2.3 4Pi and I^5M microscopy

Recapitulating, the PSF of the far-field microscope in the axial direction is significantly larger than its lateral counterparts due to the asymmetry in focusing. The focusing angle of an objective lens is technically limited to about 70°. If the angle could be increased to the full solid angle of 4π, the focal spot would be spherically symmetric. This condition can be substantially achieved by fusing the apertures of two opposing lenses by interference. Constructive interference in the focal point results in a pronounced intensity maximum that is narrower than that of a single lens. The axial resolution can even be further enhanced with coherent detection. Based on this idea, two kinds of modern microscopy had been invented: one is named 4Pi-microscopy, and the other one is I^5M microscopy (Incoherent Interference Illumination Image Interference Microscopy)[31-33].

In 4Pi-microscopy, the sample is illuminated by focusing excitation light through both objective lenses in a coherent manner onto the same spot and/or by coherently detecting the emerging fluorescence light through both lenses as shown in Fig 1-4a. Being equivalent to an increase in the aperture of the system, the constructive interference of the two focused light fields produces an illumination/detection PSF which features a central peak that is 3–4 times narrower than the focal spot of a single lens with the largest aperture angle available[33]. In the favored Two Photon Excitation(2PE) ‘type C’ mode of 4Pi-microscopy, the fluorescence light field produced by 2PE in a 4Pi illumination focus is

collected by both lenses and coherently added at a common point that is usually defined by a pinhole[34]. With the proper phase difference (multiples of 2π) at the detector, the detection-PSF is modified much in the same way as the excitation-PSF (Fig 1-4c). The effective PSF of the system (Fig 1-4d) features sidelobes that are <25% of the main maximum. A resolution enhanced image then could be obtained by scanning either the sample or the beams.

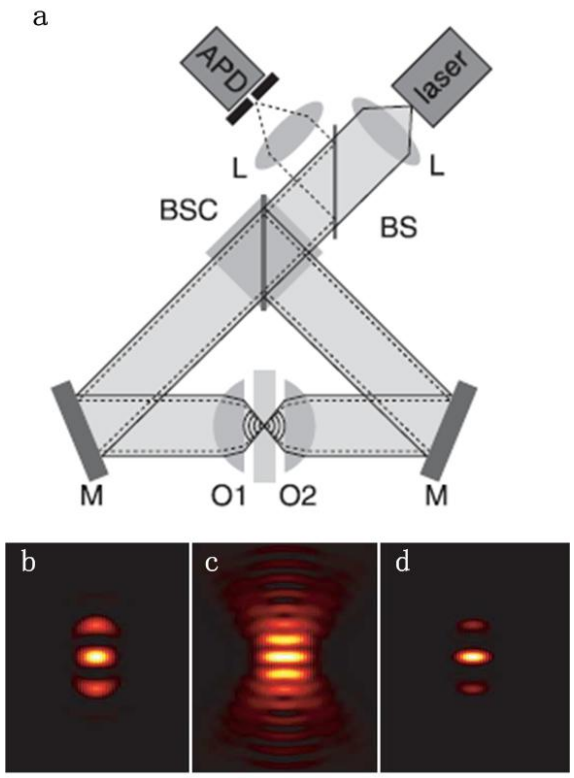

FIGURE 1-4 The schematic diagram of two photon 4Pi-C microscope:(a)The schematic diagram of two-photon 4Pi-C microscopy; (b)Excitation PSF of two-photon 4Pi-C microscopy; (c)Detection PSF of two-photon 4Pi-C microscopy; (d)Effective PSF of two-photon 4Pi-C microscopy[31]

In I^5M, the laser is replaced by a spatially incoherent light source such as an arc lamp and the sample is preferably Köhler-illuminated via both objective lenses (Fig. 1-5a), thereby making xy-scanning redundant[31]. Ideally, an azimuthal polarizer in the pupil plane of the lenses polarizes the excitation light perpendicular to the radial direction. The interfering light produces a laterally homogenous axial interference pattern whose modulation rapidly decreases to a constant intensity outside the common focal plane of the lenses (Fig 1-5c). The fluorescence is collected as in a 4Pi-microscope(of type C), i.e. by

combining the spherical wavefronts originating from a sample point in the focal plane and by subsequently adding them at the same point of detection, typically at a CCD camera. Combined with the described excitation pattern, the detection PSF leads to an effective PSF as shown in Fig 1-5e. The spherical wavefront detection imprints a spherical lobe structure in the effective PSF of the I^5M.

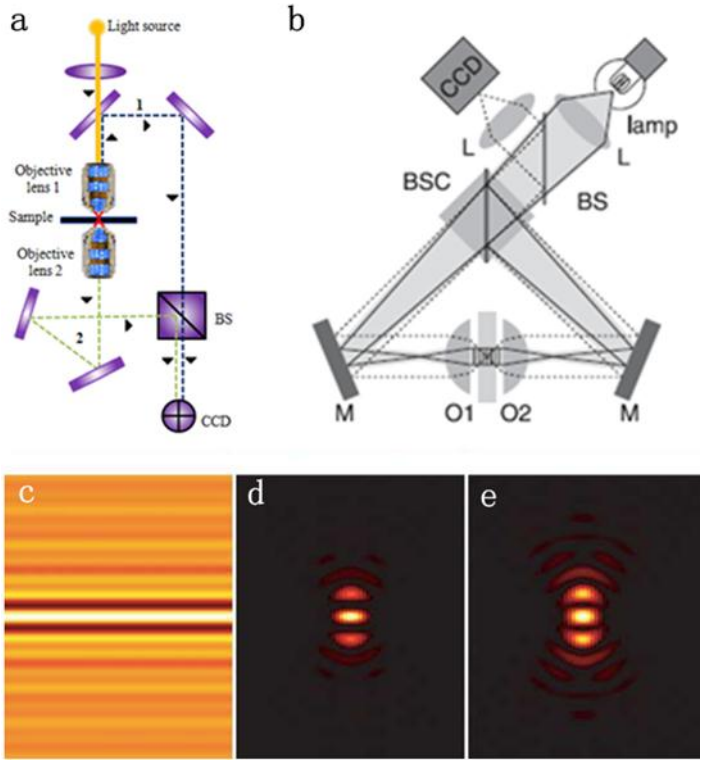

FIGURE 1-5 The schematic diagram of I5M microscopy:(a)The schematic diagram of I^2M microscopy; (b)The schematic diagram of I^5M microscopy; (c)Excitation PSF of I^5M; (d)Detection PSF of I^5M; (e)Effective PSF of I^5M[31]

The effective PSFs of both systems feature a sharp central spot of about 100 nm FWHM axial widths accompanied by axially shifted side-maxima[31]. Unfortunately, these sidelobes lead to invalid replications in the image, commonly referred to as ‘ghost images’. The removal of these ghost images is crucial for an unambiguous interpretation of the recorded structure. Comparing to conventional confocal microscopies, 4Pi and I^5M microscopy can improve resolution but the enhancement is not enough to break through the diffraction barrier. And the requirement of thin samples also limits the application.

1.2.4 Light Sheet Microscopy

Besides compensating the NA or limited the excitation volume or collection volume, other ways have been found to improve axial resolution by abandoning the standard epi-fluorescent pathway. Of these, light sheet microscopy is perhaps the most successful one[35,36].

Light sheet fluorescence microscopy (LSFM) is a fluorescence microscopy technique delivering intermediate optical resolution, but good optical sectioning capabilities and high speed, especially for living cell imaging. The perpendicular pathway design and low NA objective with long working distance allow more space for sample, especially for thick samples like tissue. In contrast to epi-fluorescence microscopy only a thin slice (usually a few hundred nanometers to a few micrometers) of the sample is illuminated perpendicularly to the direction of observation. For illumination, a laser light-sheet is used, i.e. a laser beam which is focused only in one direction (e.g. using a cylindrical lens). A second method uses a circular beam scanned in one direction to create the light sheet. As only the actually observed section is illuminated, this method reduces the photo damage and stress induced on a living sample[36]. Also the improved optical sectioning capability reduces the background signal and thus creates images with higher contrast, compared to confocal microscopy[35]. Because LSFM scans samples by using a plane of light instead of a point, it can acquire images at 100 to 1000 times faster than those offered by point-scanning methods[36].

LSFM has several important advantages over confocal microscopy, especially for studying living organisms. Most important is that it greatly reduces photobleaching of fluorescent probes and light-induced damage to the specimen. This is because the laser beam is spread out as a sheet rather than being focused onto a small area as a point. Also, no fluorescence is stimulated in regions of the sample not directly exposed to the light sheet. Furthermore, the sheet is applied to each layer of the specimen for a very short period of time, with a single image taking only milliseconds to acquire. Consequently, the specimen isn’t exposed to laser light at a high enough intensity or for a sufficiently long period of time for it to suffer any phototoxic effects or for the fluorescent probes to fade.

In this type of microscopy, the illumination is done perpendicularly to the direction of

observation (as shown in Fig 1-6). The expanded beam of a laser is focused in only one direction by a cylindrical lens, or by a combination of a cylindrical lens and a microscope objective as the latter is available in better optical quality and with higher numerical aperture than the first. This way a thin sheet of light or lightsheet is created in the focal region that can be used to excite fluorescence only in a thin slice (usually a few micrometers thin) of the sample. The fluorescence light emitted from the lightsheet is then collected perpendicularly with a standard microscope objective and projected onto an imaging sensor (usually a CCD, electron multiplying CCD or CMOS camera).

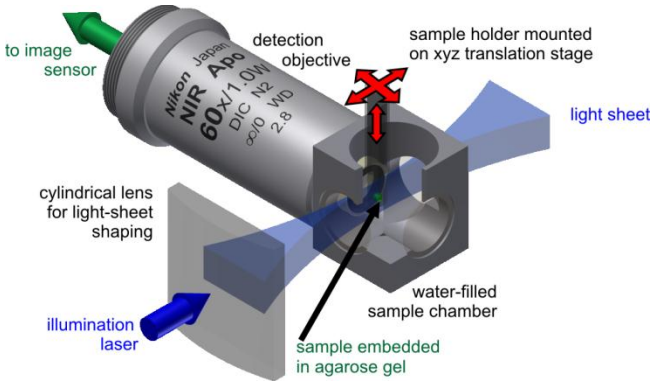

FIGURE 1-6 The schematic diagram of light sheet microscopy. The blue arrow indicates the excitation transmission direction, while the green arrow indicates the florescent collection direction. The excitation pathway is perpendicular to fluorescent pathway[37]

The sample chamber for LSM is suitable for large region scanning and live tissue imaging[38], while the resolution is still on equivalent level as confocal microscopy, which is limited by diffraction as well[39].

1.3 Super-Resolution Microscopy

Though recent developments of optical microscopy have improved the resolution to a degree, resolution of fluorescence microscopy remains limited by diffraction. Driven by the demand for resolving sub-cellular elements and processes, so-called “super-resolution microscopy” has emerged over the past 20 years, enabling the diffraction limit to be overcome so that imaging of structures on the nanoscale can be achieved[40-46]. The use of super-resolution imaging techniques in cell biology has yielded a wealth of information

regarding sub-cellular elements and processes that were invisible to conventional imaging[47-53]. This fundamental breakthrough has been recognized by award of the 2014 Nobel Prize in Chemistry to William E. Moerner, Eric Betzig and Stefan Hell.

The key advance in breaking the diffraction limit to obtain much higher image resolution requires not only advanced optical techniques, but also utilization of the methods of fluorophore photo-chemistry. And in the past two decades, two major branches of super-resolution microscopy, consisting of several different technologies have been reported to effectively break the diffraction barrier and reach the real nanometer level resolution[43]. The key idea is the same for both, that is, how to control the fluorescent emission between on and off states. The key point of the first branch is based on sub-diffraction-limit pattern excitation and the second on single molecule localization.

1.3.1 Super-resolution Fluorescence Microscopy by Spatially Patterned Excitation

In this category of techniques, a patterned field of light is applied to the sample to manipulate its fluorescence emission. This spatial modulation can be implemented either in a "positive" or "negative" manner. In the positive case, the light field used to excite the sample and generate fluorescence is directly patterned. In contrast, the negative patterning approach enlists the help of an additional patterned light field to suppress the population of molecules that can fluoresce in the sample[40,43]. In both of these approaches, the spatial information encoded into the illumination pattern allows neighboring fluorophores to be distinguished from each other, leading to enhanced spatial resolution. We refer to this approach, mainly including STED, RESOLFT, and SSIM(SIM), as super-resolution microscopy by spatially patterned excitation or the “patterned excitation” approach[41,46,54,55].

1.3.1.1 Negative Patterning: Stimulated Emission Depletion(STED)

The concept of STED microscopy was first proposed in 1994 and subsequently demonstrated experimentally[41]. In STED microscopy, the patterned illumination prevents fluorophores from emitting fluorescent photons. This suppression is achieved by stimulated emission: when an excited-state fluorophore encounters a photon that matches

the energy difference between the excited and the ground state, it can be brought back to the ground state through stimulated emission before spontaneous fluorescence emission occurs, as shown in Fig 1-7[40].

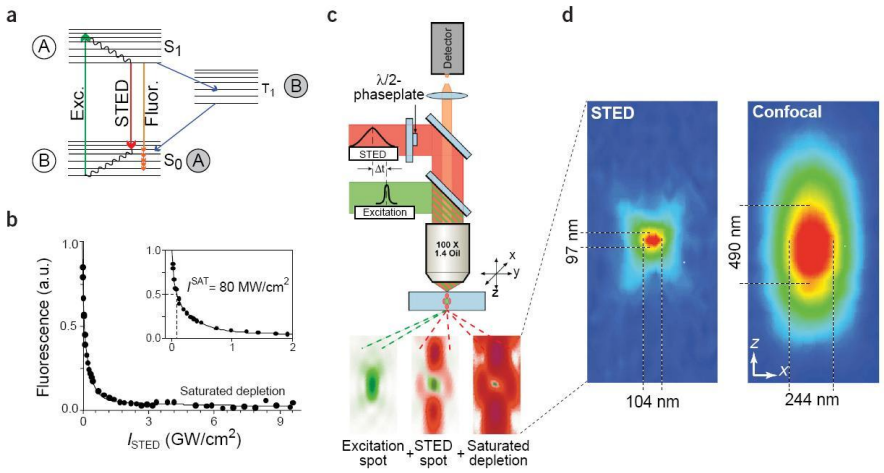

FIGURE 1-7 The chematic diagram of STED microscopy. (a)Jablonski diagram of STED progress; (b)Ratio of left fluorescent intensity vs depletion intensity curve; (c)Schematic diagram of STED microscopy; (d)PSFs of confocal and STED system[40]

This process effectively depletes excited-state fluorophores capable of fluorescence emission. In order to use STED to sharpen the excitation PSF, the STED laser needs to have a pattern with zero intensity at the center of the excitation laser focus and nonzero intensity at the periphery[56] . Typically, the diffraction spot of the excitation beam of a scanning microscope is overlapped with a doughnut-shaped spot of longer wavelength to instantly de-excite markers from their fluorescent state to the ground state by stimulated emission. Thus, effective molecular excitation is confined to the doughnut center. The higher the intensity of the doughnut, the narrower the spot becomes from which fluorescence may originate. Scanning a sharpened spot through the specimen renders images with sub-diffraction resolution.

However, this spatial pattern is also limited by the diffraction of light. Therefore, the effect of STED alone is not sufficient for sub-diffraction-limit imaging. The key to achieving super resolution is the nonlinear dependence of the depleted population on the STED laser intensity when the saturated depletion level is approached: If the local intensity of the STED laser is higher than a certain level, essentially all spontaneous fluorescence

emission is suppressed. By raising the STED laser power, the saturated depletion region expands without strongly affecting fluorescence emission at the focal point because the STED laser intensity is nearly zero at this point[57]. Consequently, the fluorescence signal can be observed only in a smaller region around the focal point, reducing the effective width of the PSF (Fig 1-7d). The size of this region, and thus the resolution of the microscope, scales approximately with the inverse square root of the intensity of the depletion light (or $\delta \approx \Delta/\sqrt{1/(1+I_{dep}/I_{sat}}$, wherein δ is the resolution, Δ is the diffraction-limited focal spotsize, measured as the full width at half maximum intensity, and I_{dep} is the intensity of the depletion laser). Super-resolution images are then obtained by scanning this "sharpened" PSF in the sample[56,57].

The pattern of the STED laser is typically generated by inserting a phase mask into the light path to modulate its phase-spatial distribution. One such phase mask generates a donut-shaped STED pattern in the xy plane. In principle, this approach allows unlimited resolution improvement given an infinitely strong depletion light source. In practice, a number of factors influence the resolution of STED microscopy: wavelength, cross-section, non-linear depletion efficiency, fluorescent lifetime and optical aberrations:

(1) According to Einstein's theory of stimulated emission, the STED beam has equal probability of stimulated absorption and emission effect on molecules. The wavelength of the STED beam should be longer than that of the fluorescence to achieve effective depletion and reduce the possibility of re-excitation[56]. Usually the wavelength should be close to the tail region of fluorescence emission spectrum. Considering that the absorption cross-section is also related with the wavelength, the further the wavelength is red-shifted, the smaller the stimulated emission cross-section will be. Eventually, there's a balance in choosing the proper depletion wavelength.

(2) The nonlinear depletion effect is the core of STED and non-linear saturation should be taken into consideration[56]. With I_{dep} increasing, the number of molecules in excited state S_1 can be eliminated strictly and FWHM of the PSF is shrunk substantially. However, photo-bleaching and photo-damage will increase rapidly with increasing intensity of the depletion beam, and imaging quality will decrease as the signal to noise ratio also affects resolving power. Therefore, resolving power of the system is limited by the stability of

molecules.

(3) Typical STED relies on ultra-short pulse lasers with appropriate temporal delay between excitation pulses and depletion pulses, wherein the delay is within the fluorescent lifetime to achieve saturated depletion. Considering the common fluorescent markers, the fluorescent lifetime is usually on nanosecond level and this leads to challenging pulse synchronization and high intensity requirements for the depletion beam. In later research, CW STED was demonstrated, but even higher depletion intensity is required[58]. Even for the advanced technique, for example, time-Gated STED (G-STED, time gating method is applied in signal collection to reduce re-excitation noise caused by depletion beam so that the signal to noise ratio is raised and less depletion power is required), which combines pulse and CW laser sources together, the depletion intensity requirement remains hundreds of MW/cm^2 to achieve sub-50 nm resolution[59].

(4) Optical aberrations arising from different refractive indices of target sample and coverslip, and the oil (immersion) layer and microscope objective, do apply further limitations to ultimate resolution of confocal microscopy including for STED-based super-resolution. These issues have been dealt with extensively by a series of published papers over the past 2 decades, most recently the chapter by Egner and Hell in the Handbook of Biological Confocal Microscopy, 3rd Edition, Ed: James P Pawley, Springer New York 2006.

In general, STED microscopy has reached a remarkable resolution of 6 nm using strong depletion intensity to image fluorescent defects in NV center diamonds, which almost never photo-bleach. On biological samples, STED imaging has achieved a resolution of 20 nm when using organic dyes and 50–70 nm resolution when using fluorescent proteins. But the intense depletion intensity requirements in most cases cause severe thermal damage to biological samples, and the cost of the STED system is high, so that it is not really suitable for live cell imaging. This limits the popularity of STED nanoscopy in biology.

1.3.1.2 Negative Patterning: RESOLFT Microscopy

As the key to high resolution is the switching of the markers, STED is only one member of the family of targeted switching methods. In general, resolution beyond the diffraction

limit can be achieved by utilizing a marker that can be toggled between two inter-connected states A and B, one of which is bright (meaning that it provides a detectable signal) and the other dark. One of the transitions, say A → B has to be light driven but then the reverse process A ← B may be spontaneous. This generalization is known as the REversible Saturable Optical Linear Fluorescent Transitions (RESOLFT) concept[60]. Again the key ingredient is the marker. Alternative RESOLFT implementations have been demonstrated so far with standard fluorescent dyes (GSD) and photo switchable proteins[54,55,61].

In GSD microscopy fluorescent markers are used. In one condition the marker can freely be excited from the ground state and returns spontaneously via emission of a fluorescence photon. However if light of appropriate wavelength is additionally applied the dye can be excited to a long-lived dark state, i.e. a state where no fluorescence occurs. As long as the molecule is in the long-lived dark state (e.g. a triplet state), it can't be excited from the ground state, as shown in Fig 1-8. Switching between these two states (bright and dark) by applying light fulfills all preconditions for the RESOLFT concept and sub-diffraction imaging and images with very high resolution can be obtained[62]. For successful realization, GSD microscopy requires either special fluorophores with high triplet yield or removal of oxygen by use of various mounting medium such as Moviol or Vectashield. To date the GSD microscopy has achieved a resolution of 7.6 nm in 2009[63].

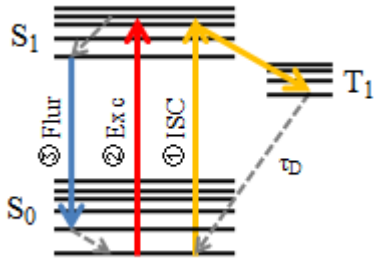

FIGURE 1-8 Jablonski diagram of GSD. S_0 is ground state, S_1 is the first excited state and T_1 is the triple state. The markers under GSD progress are excited (red arrow) to higher excited state and then fall back to T_1 state (yellow arrow). After much longer time τ_D, the markers fall back to the ground state, since τ_D indicates the lifetime on T_1 which lasts much longer than that on S_1. While normal markers will fall to S_0 by spontaneous emission (blue arrow) with shorter lifetime.

Some fluorescent proteins can be switched on and off by light of appropriate wavelength, and they can be used in a RESOLFT-type microscope. During illumination

with light, these proteins change their conformation. In the process they gain or lose their ability to emit fluorescence. The fluorescing state corresponds to state A, the non-fluorescing to state B and the RESOLFT concept applies again. The reversible transition (e.g. from B back to A) takes place either spontaneously or is driven by light. Inducing conformational changes in proteins can be achieved already at much lower switching light intensities as compared to stimulated emission or ground state depletion (even on W/cm ²)[64,65].

Just as with proteins, some organic dyes can change their structure upon illumination. The ability to fluoresce of such organic dyes can be turned on and off through visible light. Again the applied light intensities can be quite low (some at 100 W/cm²)[66].

Considering all RESOLFT cases, the off state can be the ground state of a fluorophores as in the case of STED, the triplet state as in ground-state-depletion microscopy, or the dark state of a reversibly photo-switchable fluorophores[66]. The gain in spatial resolution of RESOLFT nanoscopy is achieved in the same way as in STED, which uses a depletion laser to drive fluorophores at the periphery of the excitation into a dark state. With saturated depletion, the size of the effective PSF, δ_{eff}, becomes

$$\delta_{eff} \approx \Delta / \sqrt{1/(1+I/I_s)} \tag{1.4}$$

where δ is the diffraction-limited size of the PSF, I is the peak intensity of the depletion laser and I_s is the saturation intensity for the fluorophore. Super resolution can be achieved when the degree of saturation, I/I_s, becomes much larger than unity[60]. Unlike STED, which features a high Is value ($\sim 10^7$ W/cm^2) and thus requires an intense depletion laser (often>10^9 W/cm^2), an optical transition that has a lower I_s value can be chosen for RESOLFT, allowing super-resolution imaging at a much lower depletion laser intensity[60]. For example, RESOLFT has been demonstrated using a reversibly photo switchable fluorescent protein, as FP595, which leads to a resolution better than 100 nm at a depletion laser intensity of 600 W/cm$^{2[67]}$.

Though in some RESOLFT cases, the depletion intensity can be reduced to kw/cm^2 or even lower, it cannot be widely applied to all fluorescent markers, only very specific markers, and this limitation prevents the broad application of RESOLFT nanoscopy.

1.3.1.3 Positive Patterning; SIM and SSIM

While RESOLFT, or negative patterning super-resolution imaging, is conceived in the context of laser-scanning microscopy and is designed to directly minimize the size of a scanned focal point, *positive* patterning super-resolution imaging actually brings theoretically unlimited resolution to a wide-field (non-scanning) microscope by using a nonlinear fluorescence response together with a periodic illumination pattern that fills the field of view.

The reason that positive structured illumination can provide resolution increases is that it renders otherwise unresolvable high-resolution information visible in the form of low-resolution Moiré fringes. A Moiré pattern is a secondary and visually evident superimposed pattern created, for example, when two identical (usually transparent) patterns on a flat or curved surface (such as closely spaced straight lines drawn radiating from a point or taking the form of a grid) are overlaid while displaced or rotated a small amount from one another. And the strength of this effect is proportional to the spatial frequency of the pattern.

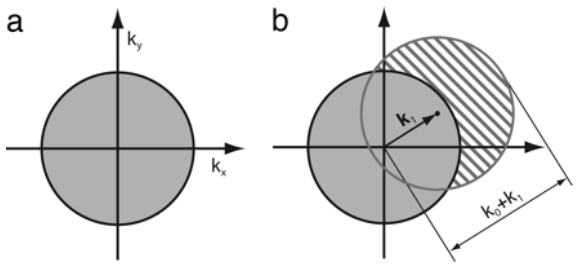

FIGURE 1-9 The schematic of SIM. (a) Detected frequency field for normal microscope; (b)Extended frequency detection field in SIM

The classical resolution limit specifies a maximum spatial frequency k_0 that can be observed through the microscope. For a light microscope, $k_0 = 2NA/\lambda_{em}$, where λ_{em} is the observation wavelength and NA is the numerical aperture of the objective lens. If the frequency content of the sample is described in a 2D frequency space, then this limit defines an "observable region" (a circle with radius k_0 around the origin), as shown in Fig 1-9a. Information outside of this region is fundamentally unobservable in the conventional microscope. The goal of resolution extension is to render some of that information

observable, that is, to enlarge the observable region.

Structured-Illumination Microscopy (SIM) extends resolution beyond the diffraction limit by moving information into the observable region, from elsewhere in frequency space, in the form of moiré fringes[45]. Moiré fringes are produced by frequency mixing whenever two signals are multiplied. SIM improves image resolution by using positive patterning of the excitation light, which is typically a sinusoidal pattern created by combining (i.e., interfering) two light beams. As a result, an image snapshot of the sample becomes the product of the sample structure itself and this excitation pattern. A final image is then computationally reconstructed from multiple snapshots collected by scanning and rotating the pattern[45]. In this process, the additional spatial modulation from the excitation pattern brings enhanced spatial resolution into the reconstructed image. In this case, the multiplication is the one inherent in fluorescence: the observed emission intensity is the product of the local density of fluorescent dye (i.e., the sample) and the local intensity of excitation light.

If the illumination contains a spatial frequency k_1, then each sample frequency k gives rise to moiré fringes at the difference frequency $k–k_1$. Those fringes will be observable in the microscope if $|k–k_1| < k_0$, that is, if k lies within a circle of radius k_0 around k_1 (Fig 1-9b). Thus, the information within that circle has been made indirectly observable, and it can be extracted by using a phase-shift method. The new information increases the highest observable spatial frequency (the resolution) from k_0 to k_0+k_1. Thus, to maximize the resolution, it is desirable for the illumination to contain as high spatial frequencies k_1 as possible. Unfortunately, the set of spatial frequencies that can be generated in a light field is limited by diffraction in the same way as the set of frequencies that can be observed. Thus, k_1 cannot be made larger than $2NA/\lambda_{exc} \approx k_0$, so the new resolution limit $k_0 + k_1$ can be at most $\approx 2k_0$. Hence, normal linear SIM can extend resolution only by a factor of ≈ 2. In another words, SIM can improve optical resolution but only half that of the standard diffraction limit, still insufficient to resolve sub-cellular structures[68,69].

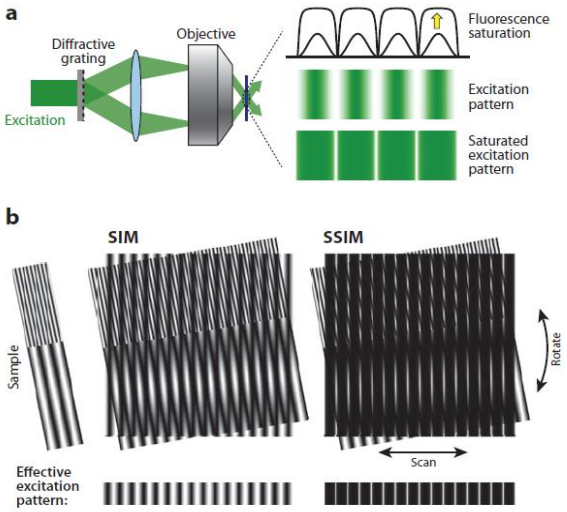

FIGURE 1-10 The schematic diagram of SSIM. (a)The schematic diagram of saturated excitation pattern in SSIM; (b)The comparison of excitation patterns of SIM and SSIM

As is true for the depletion light pattern used in STED, the illumination pattern created by interference is also limited by diffraction. Therefore, when the fluorescence signal scales linearly with the intensity of the excitation light, SIM results only in a doubling of spatial resolution. However, as with the negative patterning approach, the saturating response of the fluorophores can also be exploited here to further enhance the resolution. Saturated SIM (SSIM) utilizes this phenomenon to create sharp dark regions where the excitation pattern has zero intensity, providing image resolution significantly beyond the diffraction limit[70].

Such a non-linearity would cause the effective illumination pattern to contain harmonics with spatial frequencies that are multiples of k_1. A component with frequency $2k_1$ would extend resolution by twice as much as the linear method, a $3k_1$ component by three times as much, etc. If the nonlinearity can be described by a polynomial of order s, it will give rise to s–1 new harmonics. A nonlinearity that is non-polynomial (i.e., has an infinite Taylor series) thus produces an infinite number of harmonics, corresponding to theoretically infinite resolution. The resolution in practice will be finite, of course, but bounded only by practical issues of signal-to-noise ratio and photo stability, not by any fundamental limit[71].

In the normal fluorescence process, a fluorophore molecule in its electronic ground

state S_0 is excited to the first excited state S_1 by absorbing a photon at λ_{exc} and decays back to S_0 after an average time τ (the fluorescence lifetime) as it emits a photon at λ_{em}. Clearly, on average each molecule can emit at most one photon per lifetime τ. Thus, it cannot respond linearly to illumination intensities above one photon per absorption cross section per lifetime. If the sample is illuminated by a sinusoidal light pattern with a peak intensity that is near or above this threshold, then the pattern of emission rate per fluorophore takes on a non-sinusoidal shape (Fig 1-10a), which contains the desired series of harmonics with higher spatial frequency than the illumination pattern itself.

If a sample is illuminated with such a distorted pattern, the observed image will be a superposition of several information components, each displaced in frequency space by an amount corresponding to the spatial frequency of each Fourier component of the pattern (Fig 1-10). The number of pattern harmonics, and thus the number of contributing information components, is infinite, in principle. In practice, however, only a finite number of information components are strong enough to rise above the noise level[71].

So SSIM also requires shifting the illumination pattern multiple times, effectively limiting the temporal resolution of the technique. In addition there is a need for very photo stable fluorophores due to the saturating conditions. These conditions also induce photo-damage to the sample that restricts the possible applications in which SSIM may be used.

The main problems with SSIM are that, in this incarnation, saturating excitation powers cause more photo damage and lower fluorophore photo stability, and sample drift must be kept to below the resolving distance. The former limitation might be solved by using a different nonlinearity (such as stimulated emission depletion or reversible photo activation, both of which are used in other sub-diffraction imaging schemes); the latter limits live-cell imaging and may require faster frame rates or the use of additional markers for drift subtraction[44]. Nevertheless, SSIM is a strong contender for further application in the field of super-resolution microscopy.

1.3.2 Super-Resolution Fluorescence Microscopy by Single-Molecule Switching Localizing with High Precision

Images not only consist of size of PSF and fluorescent markers but also position of individual objects. A biological structure is ultimately defined by the positions of the molecules that build up the structure. Similarly, a fluorescence image is defined by the spatial coordinates of the fluorophores that generate the image. It is thus conceivable that super-resolution fluorescence microscopy can also be achieved by determining the position of each fluorescent probe in a sample with high precision[43,52,72].

Single molecule localization and reconstruction microscopy, also referred to as pointillist microscopy, encompasses an array of techniques that provide enhanced resolution by localizing single molecules that are separated by more than the resolution limit. Localizing involves finding the center (i.e., position) of the molecule from an image of its PSF; a localization precision as small as 1 nm has been demonstrated for single fluorescent molecules. Single molecule techniques rely on the manipulation of the optical properties of the labeled molecules within the specimen to achieve a higher localization precision and consequently a higher resolution. In order for molecules to be a localized with high precision, they need to be distinctly (spatially or temporally) separated. And different condition is required due to different single molecule localization methods.

This can be achieved in two ways: (1) by labeling the specimen with a very low density of fluorophores wherein the molecules to be localized are distinctly separated; this concept is utilized in fluorescent speckle microscopy (FSM) and other techniques that exploit fluorescence intermittency[73]. Other methods have exploited stepwise photo bleaching to localize single molecules, although these methods have required small numbers of probe molecules to be located within a diffraction-limited area[74,75]. The localization of diffusing probe molecules that become fluorescent as they bind to a target molecule and subsequently photo bleaching has also been demonstrated, although control over the density of fluorescent molecules in this approach still requires the adjustment of the concentration of probe molecules; (2) by using photo-activatable and/or photo-switchable fluorophores that can be switched between the bright and dark states thereby providing an optical control over the fluorescent properties of the targeted sample[76,77].

In a typical wide-field fluorescence microscopy setup, all the fluorescent molecules are visible at the same time, which leads to diffraction-limited blurring of the sample as a result of the overlap of PSFs of the different molecules. When only a few molecules are visible such that the PSFs of the molecules do not overlap, the molecules will be well separated and distinct from one another. In such a scenario, the positions (centers) of the molecules can be identified (this is also referred to as localizing a molecule)with a very high precision. An object can be localized with greater precision (smaller error) than the diffracted-limited resolution. The two-dimensional localization precision (σ_{xy}) of a fluorescent object is given by

$$\sigma_{xy}^2 = \frac{s^2 + q^2/12}{N} + \frac{8\pi s^4 b^2}{q^2 N^2} \tag{1.5}$$

where

s is the standard deviation of the PSF (which is proportional to the resolution)

N is the total number of photons collected (not photons per pixel)

q is the effective size of an image pixel within the sample focal plane

b is the background noise per pixel (not background intensity)

Thus, single fluorescent molecules can be localized with greatest precision, and the localization precision can be improved by increasing the number of detected photons and decreasing the background.

But being able to localize a single molecule does not directly translate into super-resolution imaging of a fluorescently labeled biological sample, which can contain thousands of fluorophores inside of the diffraction-limited region. The fluorescence emission from these molecules will overlap severely enough that the overall image appears as a completely featureless blur. At first sight, it might seem impossible to distinguish these molecules individually. However, if the fluorescence emission from these molecules is controlled such that only one molecule is emitting at a time, individual molecules can then be imaged and localized. This is the idea behind a recently developed super-resolution imaging method called PALM[52], or FPALM[53] and STORM[48].

1.3.2.1 PALM and FPALM

In 2006, Photo-Activation Localization Microscopy (PALM) was demonstrated, wherein a random stimulation method is used to improve optical resolving power[52]. A fluorescent molecule in one Airy disk can be activated individually and then bleached permanently by the exact same order, so that single-molecule fluorescence microscopy is used to compute and map the precise position of each molecule center, and after several cycles a final image is compiled. Special fluorescent molecules are also the key to success in PALM. PA-GFP is widely applied in PALM because of its key property that fluorescence is only observed after activation by light of 405 nm wavelength co-existing with excitation beam. FPALM (Fluorescence Photo-activation Localization Microscopy) technology was also demonstrated in 2006, and is similar to PALM[53].

The specific procedure is as shown in Fig 1-11: First, a few proteins tagged by PA-GFP are activated with low intensity (milliwatt per square centimeter) activation laser beam. Then, continuous-wave excitation turns on and the few activated markers start to fluoresce. By calculating and positioning the centers of these molecules, precise location can be obtained. Excitation is required for sufficient time for the excited molecules to be permanently bleached so that they cannot participate in the following excitation cycle, and the signal to noise ratio of the next cycle is not be influenced by former cycles. Thus the accurate position of each molecule can be fitted according to real image results, and repeating the activation-excitation-bleaching cycle enables the final image to be synthesized[52,78].

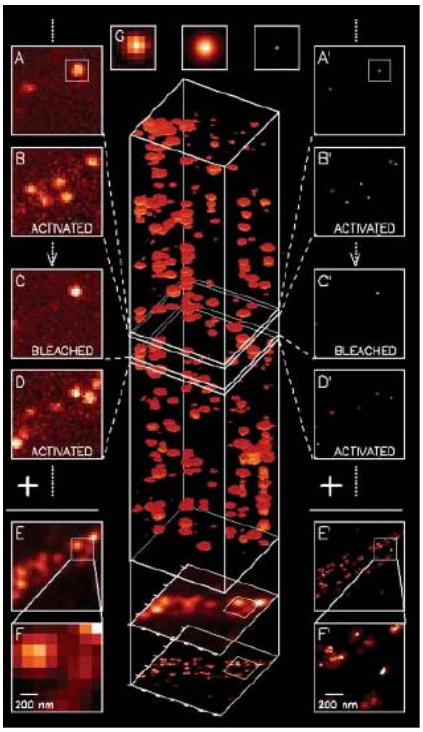

FIGURE 1-11 The schematic diagram of PALM. (A)(B)(C)Attach PA-GFP fluorescent markers to the target and activate very few markers with pulse mode 405 nm laser, then use 561 nm laser to excite these markers to fluoresce. Keep excitation until the activated markers get bleached; (D)Repeat the A, B, C process until all markers get bleached; (E)(F)Overlap all results together to get the final result which is diffraction limited; (G)The left sub-figure indicates the actual imaging result of one individual marker. The central one indicates the ideal PSF. The right one is the result after fitting. (A')(B')(C')(D')(E')(F') shows the fitting results respectively[52]

1.3.2.2 STORM

Quite similar to PALM, STochastical Optical Reconstruction Microscopy (STORM) was first reported in 2006 as well[48]. STORM was originally described using Cy5 and Cy3 dyes attached to nucleic acids or proteins. In this technique, Cy3 and Cy5 proteins cascaded together as a source could be activated repeatedly: illumination with different wavelengths makes Cy5 experience the process "activated and excited→emission→ bleached→recovery→activated" hundreds of times, until permanent bleaching is achieved. Sub-diffraction resolution can be obtained after stochastically stimulating fluorescent molecules to locate the exact center of each element available.

The approach is: first, a 30 W/cm^2 red beam (633 nm) illuminates the sample in order to force all the Cy5 into the dark state; second, 1 W/cm^2 532 nm green beam activates

several Cy3 to pull Cy5 from non-fluorescence state to bright state in order to restore the capacity of fluorescence emission; at this time 633 nm excites a few fluorescent molecules to make them emit and then go back to the non-fluorescent state again, preparing for the next cycle. To be emphasized, each Cy5 can be activated several times in STORM until it is completely bleached, so one point of orientation is the result of multiple measurements because each Cy5-Cy3 pair can be measured again and again. It can be concluded that STORM contains several PALM processes, since in PALM a single point is located only once. An accurate position depends on the number of photons emitted from single molecule, so when the molecule experiences 20 or more cycles, resolution is up to 20 nm after fitting. From the perspective of statistics, STORM allows higher location precision than PALM[79].

However, the advantage of single-molecule switching localizing microscopy is also its disadvantage: only few molecules or even a single molecule participate in each cycle. Although localization ability improves substantially, imaging speed drops and the field of view shrinks due to the transformation from high-accurate positioning by single-molecule imaging technique to sub-diffraction microscopy. The imaging speed is usually over seconds, and it typically takes several hours or even days to detect molecules. This severely limits the application of PALM/FPALM/STORM to biology.

1.4 Towards live-cell super-resolution imaging

The breakthroughs above in optical super-resolution imaging have brought exciting times in cell biology, because non-destructive live-cell imaging with molecular resolution (1−5 nm) is now closer to reality.

However, not all of the super-resolution techniques have the same potential towards that goal, which requires sufficient speed for real-time imaging in the first place. By analysing the working principles of different types of super-resolution techniques, it is widely perceived that the single molecule localization branch, including PALM and STORM, is not possible for real-time imaging, due to the statistic/stochastic nature of their operation that requires complicated processes of curve fitting, center localization and image reconstruction to get the final results[79]. Likewise, the positive patterned excitation

method, including SIM and SSIM relies on intensive post-processing of the raw data, for example via Fourier transform, which becomes increasingly complicated and time-consuming if a significant factor of resolution enhancement is desired. Besides real-time imaging speed, optical sectioning capability is also required to achieve super-resolution imaging in live cells, in order to address an arbitrary focal plane in the interior of a sample. The single-molecule switching methods and the structure illumination methods do not provide this capability, unless nonlinear multiphoton absorption is employed[80]. This limitation accounts for the fact that live cell recordings with these methods have so far been largely limited to the plasma membrane[81].

Compared to other major super-resolution techniques, STED is highly favored by biologists due to its fast imaging speed. In addition, the phase modulation for the doughnut beam can be realized in 3D, for example in the iso-STED method, so that super-resolution results can be achieved for both the lateral and the axial directions simultaneously[82]. STED has been shown to allow real-time super-resolution imaging, for example, in tracking of single synaptic vesicles in cultured hippocampal neurons and revealing of the anatomy and dynamics of syntaxin-I clusters in PC12 cells[83].

However, the key limitation with STED is the extreme optical intensities typically needed for achieving stimulated emission so as to deplete the fluorescence around the focus, which power level is destructive for the majority of live samples. Additionally, the complexity and costs for installation and maintenance of high-power lasers in biological labs is a barrier to this technology being widely used[84].

For STED, given a fixed laser power, the super resolution achievable in theory is largely determined by the depletion efficiency (which is typically represented by the saturation intensity) of the probes. Therefore, the power challenge in STED may be overcome if we can find new types of luminescent probes that can be switched (off) more efficiently via novel depletion pathways.

In this section, we first summarize the fluorescent probes that have been employed in STED. We then carry out theoretical analysis and simulation to study the typical pulsed STED process, which aims to identify the key probe properties that can be exploited to potentially bring down the depletion intensity requirement in STED. In particular, we study

the dependence of the depletion efficiency on the fluorescent/luminescent decay lifetime, and the cross-section for stimulation. The results suggest a possible new avenue to lowering the power requirement in STED.

1.4.1 Fluorescent probes for STED super-resolution microscopy

In the past, organic probes like fluorescent proteins (FPs) and small-molecule fluorophores have been widely used in STED microscopy, as well as two kinds of inorganic probes, quantum dots and NV centers[85,86].

For fluorescent proteins, simple FPs, such as green FP (GFP) and yellow FP (YFP), have been used in STED imaging[67,87]. As for small-molecule fluorophores , among regular fluorescent probes, ATTO and DY dyes have been widely used in STED imaging owing to their intense brightness and high photostability[58,88]. For biological samples, STED imaging has achieved a resolution of 20 nm when using organic dyes and 50–70 nm resolution when using fluorescent proteins[67,87,89]. Taking advantage of its ability to target arbitrary coordinates within a cell and to record many molecules from those coordinates in parallel, STED microscopy has been shown to capture the movement of synaptic vesicles inside living neurons at video rate[58,90].

Researchers have also used inorganic probes in STED microscopy, notably quantum dots (QDs)[91], the use of which as bioprobes has been demonstrated in several experiments over the past decade[92]. Thanks to their larger extinction coefficients, QDs generally yield stronger emission in comparison to molecular probes[93]. The shape of the emission band of QDs is symmetric, and the spectral peaks of emissions are highly dependent on the size of dots. QDs are inorganic semiconductor nanocrystals, typically composed of a cadmium selenide (CdSe) core and a zinc sulphide (ZnS) shell and whose excitons (excited electron-hole pairs) are confined in all three dimensions, which gives rise to characteristic fluorescent properties. For biological applications, QDs are coated with a passivating layer to improve solubility, and are conjugated to targeting biomolecules, such as antibodies or streptavidin (Fig 1-12a). As fluorescent probes, QDs are characterized by broad absorption profiles, high extinction coefficients and narrow and spectrally tunable emission profiles. Small CdSe QD cores (2.3 nm diameter) emit blue light, whereas larger

crystals (5.5 nm diameter) emit red light, producing size-dependent optical properties (Fig 1-12b)[91].

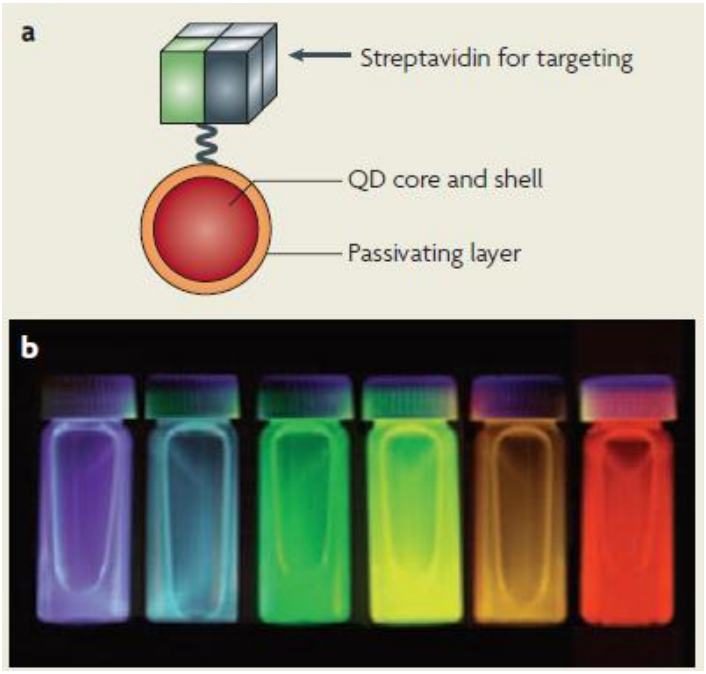

FIGURE 1-12 (a) For biological applications, QDs are coated with a passivating layer to improve solubility, and are conjugated to targeting biomolecules, such as antibodies or streptavidin, (b) The size-dependent optical properties of QDs [89]

The widely popular class of quantum-dot molecular labels could so far not be utilized as standard fluorescent probes in STED (stimulated emission depletion) nanoscopy. This is because broad quantum-dot excitation spectra extend deeply into the spectral bands used for STED, thus compromising the transient fluorescence depletion required for attaining super-resolution.

In addition, the characteristic blinking of QDs is a significant disadvantage which limits real-time applications. One could not count on the reliable fast tracking live process when the targets jump into the dark state. And without properly solving the photo blinking problem, the QDs are not even optimal for live cell imaging.

NV-center diamonds have also been used in STED super-resolution imaging. STED microscopy has reached a remarkable resolution of 5.8 nm using strong depletion intensity to image fluorescent defects in NV center diamonds[85], which almost never photo-bleach.

But one of the well-known disadvantages is the challenge of selectively labelling NV-center nanodiamonds to biological samples.

Despite past attempts using organic or inorganic probes, the depletion intensities over 10^8 W/cm^2 required for STED super-resolution are highly damaging to biological samples. The current-generation STED remains of limited suitability for application in biology.

1.4.2 Simulation of the STED process

To gain an understanding of which fluorescent materials and excitation-depletion concepts may offer the potential to achieve STED under conditions applicable to super resolution imaging of biological samples, it is helpful to undertake theoretical numerical simulation of the STED process.

Fig 1-13 displays the simplified energy levels of a typical fluorophore[57]. S_0 and S_1 are the ground and first excited singlet states, respectively. L_1 and L_3 are higher vibronic levels of these states while L_2 and L_0 are relaxed levels. The excitation of the dye takes place from L_0 to L_1, and fluorescence by the radiative transition L_2 to L_3. The transition S_1 to S_0 can also be induced by stimulated emission, which is of particular interest here. The transitions L_1 to L_2 and L_3 to L_0 are vibrational relaxations. In the discussion of stimulated emission we can ignore the triplet state.

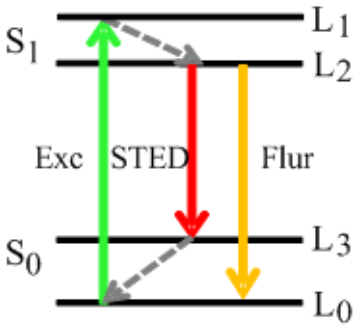

FIGURE 1-13 Simplified four-states stimulated emission depletion progress

Fig 1-13 also displays the transition rates. The rates of the spontaneous processes are given by the inverse of the lifetimes τ of the source states. The fluorescence rate is

$k_{FLUOR}=1/\tau_{FLUOR}$, the rate for vibrational decay is $k_{VIB}=1/\tau_{VIB}$, and the non-radiative quenching rate of S_0 is $Q=1/\tau_Q$.The rates for excitation and stimulated emission are given by the product of the photon fluxes of the beams and molecular cross sections, i.e. $h_{EXC}\sigma_{EXC}$ and $h_{STED}\sigma_{STED}$ for the excitation and stimulated emission, respectively. Typical values of σ_{EXC} and σ_{STED} are 10^{-16}–10^{-20} cm^2, respectively. The fluorescence lifetimes τ_{FLUOR} and τ_Q are on the order of 1 and 10 ns, respectively. The lifetimes of the vibrationally excited states are very short, $\tau_{VIB} \leq 1$ ps. Thus, the vibrational relaxation L_1 to L_2 and L_3 to L_0 are three orders of magnitude faster than fluorescence. The rapid vibrational decay causes the molecules in L_1 to relax to L_2 before emitting a photon. The state L_2 is the actual source of fluorescence photons, and the effective number of emitted fluorescence photons is directly proportional to the L_2 population. To a good approximation and at room temperature, L_2 represents a bottleneck every molecule has to pass before emitting a fluorescence photon.

The following set of differential equations describes the interplay between absorption, thermal quenching, vibrational relaxation, spontaneous, and stimulated emission. The equations also include re-excitation of the vibrationally excited ground state L_3 at λ_{STED}, and stimulated emission at the excitation wavelength λ_{EXC}. The n_i (i=0,1,2,3) stands for the population intensity of electrons on state L_i which also equals to the population intensity of excited molecules on the corresponding state.

$$\begin{cases} \dfrac{dn_0}{dt} = \dfrac{I_{EXC}\sigma_{01}}{h\nu_{EXC}}\left(n_1 - n_0\right) + \dfrac{1}{\tau_{VIBR}} n_3 \\ \dfrac{dn_1}{dt} = \dfrac{I_{EXC}\sigma_{01}}{h\nu_{EXC}}\left(n_0 - n_1\right) - \dfrac{1}{\tau_{VIBR}} n_1 \\ \dfrac{dn_2}{dt} = \dfrac{I_{STED}\sigma_{23}}{h\nu_{STED}}\left(n_3 - n_2\right) + \dfrac{1}{\tau_{VIBR}} n_1 - \left(\dfrac{1}{\tau_{FLUOR}} + Q\right) n_2 \\ \dfrac{dn_3}{dt} = \dfrac{I_{STED}\sigma_{23}}{h\nu_{STED}}\left(n_2 - n_3\right) - \dfrac{1}{\tau_{VIBR}} n_3 + \left(\dfrac{1}{\tau_{FLUOR}} + Q\right) n_2 \end{cases} \tag{1.6}$$

The equation could be solved by using Runge–Kutta method of order 4 in the isolated initialization conditions as follows:

$$\begin{cases} n_0\big|_{t=0} = 1 \\ n_i\big|_{t=0} = 0, i = 1,2,3. \end{cases} \tag{1.7}$$

And normalization condition of

$$\sum_{i=0}^{3} n_i = 1 \tag{1.8}$$

It is of interest to investigate the depletion process. The following parameters were chosen: pulse duration width for excitation and depletion beam τ_{FLUORE}=2 ns, Q=0.1 ns, τ_{VIB}=1 ps, λ_{EXC}=635 nm, λ_{STED}=760 nm, $\sigma_{01}=\sigma_{23}=10^{-16}$ cm^2.

Let us assume that the fluorescence molecules are already excited, i.e. $n_2(t=0)=1$, and the excitation pulse is switched off. The population probability of L_2 is time dependent when subjected to a stimulating pulse of 100 ps duration (FWHM), reaching its maximum at t=200 ps after the sub-picosecond excitation pulse has left the focal plane. We can safely neglect the triplet state of the dye since intersystem crossing is too slow to play a role on this time scale.

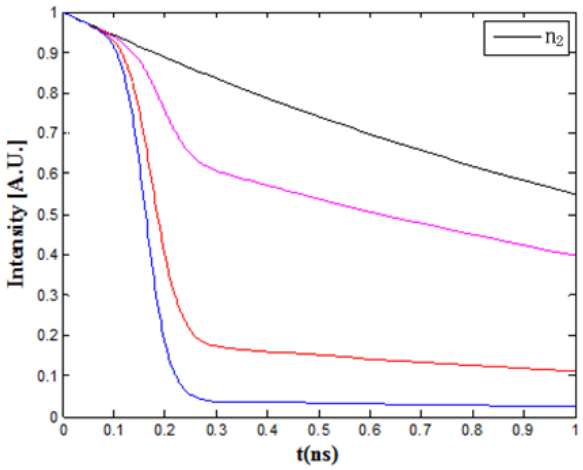

FIGURE 1-14 The intensity of molecules on the fluorescent sub-state changed with time. Black curve indicates the spontaneous emission. Magenta curve indicates STED intensity of 10 MW/cm^2. Red curve indicates STED intensity of 50 MW/cm^2. Blue curve indicates STED intensity of 100 MW/cm^2

As shown in Fig 1-14, curve black describes the regular fluorescence decay of L_2 with the STED beam switched off, and curves magenta/red/blue show how the STED beam depletes the population of L_2. For low intensities, as curve magenta with depletion intensity of 10 MW/cm^2, the depletion by stimulated emission is not complete. After the STED- pulse

has passed, the decrease of n_2 is governed by spontaneous emission and non-radiative quenching. For higher pulse intensities, as for the blue curve, depletion is strong, and for a peak intensity of 100 MW/cm^2, the state L_2 is depleted after 200 ps. As long as the pulse length is much shorter than the lifetime of the state L_2 and assuming that stimulated emission has not reached saturation, depletion increases with increasing numbers of stimulating photons in the pulse.

In the simulation, the frequency of photons and the intensity is fixed and determined by the practical condition in real scenario, while fluorescent lifetime and cross-section is determined by the probe itself and these two factors vary with different materials.

1.4.3 The key role of lifetime and cross-section in STED progress

To explore the role of lifetime in stimulated emission depletion, we conducted the controlled experiment by simulation. The wavelength of excitation and depletion remains to be 635 nm and 760 nm respectively. The fluorescent lifetime is extended to 2 us, which is three orders of magnitude of that in 1.5.1. Accordingly, the pulse duration time of excitation and depletion is extended to 100 ns. The vibration decay and non-radiative quenching rate stays the same. The cross section is fixed to be $\sigma_{01}=\sigma_{23}=10^{-16}$ cm^2. The excitation intensity is I_{EXC}=100 MW/cm^2. The depletion beam reaches its maximum at t=200 ns after the excitation pulse has left the focal plane.

Given the same initiation and normalization condition, increasing the depletion intensity I_{STED} from 0 to 100 MW/cm^2, we can get the simulation result of the time dependant population probability of state L_2, as shown in Fig 1-15.

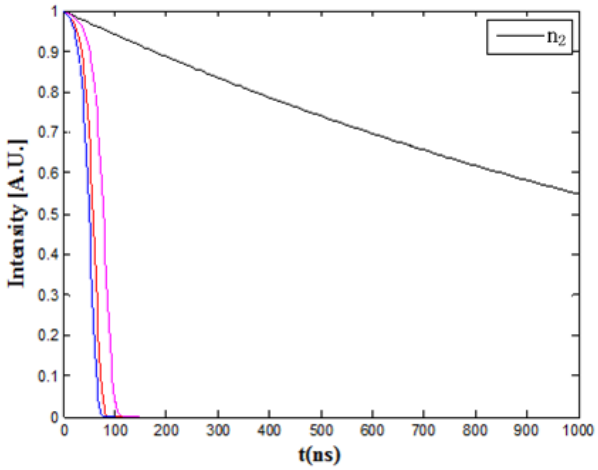

FIGURE 1-15 The intensity of molecules on the fluorescent sub-state changed with time under the condition of extended fluorescent lifetime on micro-second level. Black curve indicates the spontaneous emission. Magenta curve indicates STED intensity of 10 MW/cm^2. Red curve indicates STED intensity of 50 MW/cm^2. Blue curve indicates STED intensity of 100 MW/cm^2

Comparing the results to those under the condition of nanosecond level fluorescent lifetime, for any tested depletion intensity condition, the stimulated emission depletion rate becomes much faster. The controlled simulation results show that stimulation emission tends to occur much easier on the probes with longer fluorescent lifetime. This may provide the chance to reduce the intensity requirement in STED process. To make the simulation more complete the influence of cross section in the STED process was also examined with the conclusion that the duration of excitation and depletion is comparatively insensitive to cross-section at depletion power close to saturation.

After the study of fluorescent lifetime, we also study the role of cross-section in STED progress. To explore the role of cross-section in stimulated emission depletion, we conducted the controlled experiment by simulation. The wavelength of excitation and depletion remains to be 635 nm and 760 nm respectively, and the fluorescent lifetime is fixed at 2 ns, which is the same as that in section 1.5.1. The pulse duration time of the excitation and depletion laser is 100 ps. The vibration decay and non-radiative quenching rate stays the same. The excitation intensity is I_{EXC}=100 MW/cm^2. The depletion beam reaches its maximum at t=200 ps after the excitation pulse has left the focal plane and I_{STED}=50 MW/cm^2.

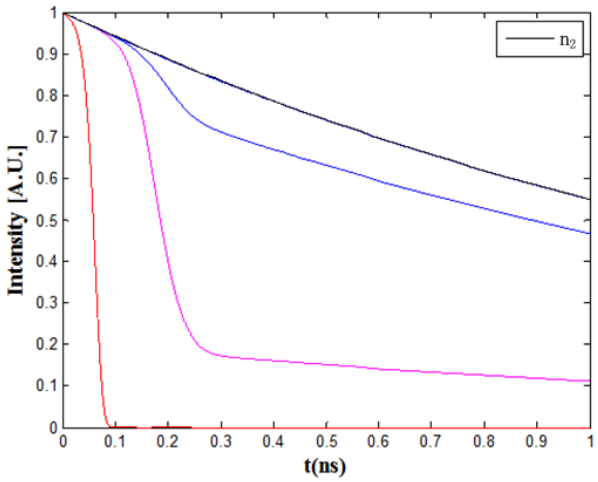

FIGURE 1-16 The intensity of molecules on the fluorescent sub-state changed with time under the condition of different stimulated absorption cross-section. Black curve indicates the spontaneous emission. Magenta curve indicates stimulated absorption cross-section of 10^{-16} cm^2. Blue curve indicates stimulated absorption cross-section of 10^{-17} cm^2. Red curve indicates stimulated absorption cross-section of 10^{-13} cm^2

Given the same initiation and normalization condition, by choosing different cross-section value $\sigma=10^{-17}$ cm^2, 10^{-16} cm^2, 10^{-13} cm^2 respectively, we simulate the time dependant population probability of state L_2, as shown in Fig 1-16.

1.4.4 Opportunity for low-power STED using lanthanide nanoparticles

From the simulation results above, it can be seen that if the probes exhibit longer lifetime and larger cross-section, stimulated emission depletion will be more likely to occur under identical optical conditions. Conventional fluorescent probes, such as organic dyes or quantum dots, have restrained lifetimes on the nanosecond timescale and fixed values of moderate cross-section. Therefore, they requires extreme intensity, typically 10^2-10^3 MW/cm^2, for effective stimulated emission depletion.

Long lifetime probes with large cross-sections are promising to largely reduce the power requirement in STED and achieve biocompatible super-resolution microscopy. However, it is generally the case for individual molecules that increase in the lifetime is accompanied by reduced cross-section, thereby substantially reducing the overall advantage of long lifetime. This challenge, however, may be overcome by using nanoparticles incorporating a large number of individual probes compactly, so that they

exhibit a large collective cross-section.

This hypothesis has prompted the present investigation of lanthanide-doped nanoparticles as a potential candidate to achieve low-power STED. Particular attention is paid to upconversion nanocrystals doped with trivalent lanthanide ions. These possess metastable energy levels in scaffold-like structures, and allow high doping concentrations that cannot be achieved in their bulk counterparts. Additionally, the rich energy levels provide flexibility to design separated luminescence and depletion pathways, which is hardly possible with conventional fluorescent probes.

1.4.5 Lanthanide-doped upconversion nanocrystal

Lanthanide-based upconversion nanocrystals are composed of an inorganic crystalline host matrix embedded with trivalent lanthanide ions (Ln^{3+}) (Fig 1-17). They are capable of absorbing longer wavelength illumination and emitting shorter wavelength luminescence[94-96]. But unlike two-photon absorption and second-harmonic generation, the photon upconversion process features sequential, rather than simultaneous, absorption of incident photons, which relies on the physical intermediate states between the ground state and the emitting state to act as energy reservoirs. These are underpinned by the ladder-like energy levels of trivalent lanthanide ions, whose $4f_n$ electronic configurations are split by appreciable electronic repulsion and spin–orbit coupling (Fig 1-17b)[94]. This attribute makes lanthanides the ideal candidates for photon upconversion.

The lanthanides' *4f* orbital electrons are partially filled and shielded by outer *5s* and *5p* electrons, giving rise to a weak electron–phonon coupling and hence sharp emission lines resulting from electronic transitions, compared to broad emission spectra of conventional fluorescent probes and quantum dots. Efficient photon upconversion greatly benefits from a crystalline host lattice featuring a low phonon energy environment. This effectively suppresses the non-radiative decay pathways due to multi-phonon relaxation in such ionic crystals. Using different lanthanide ions, upconversion emission can be precisely tuned to a particular wavelength spanning from the ultraviolet to the near-infrared region (Fig 1-17c)[94].

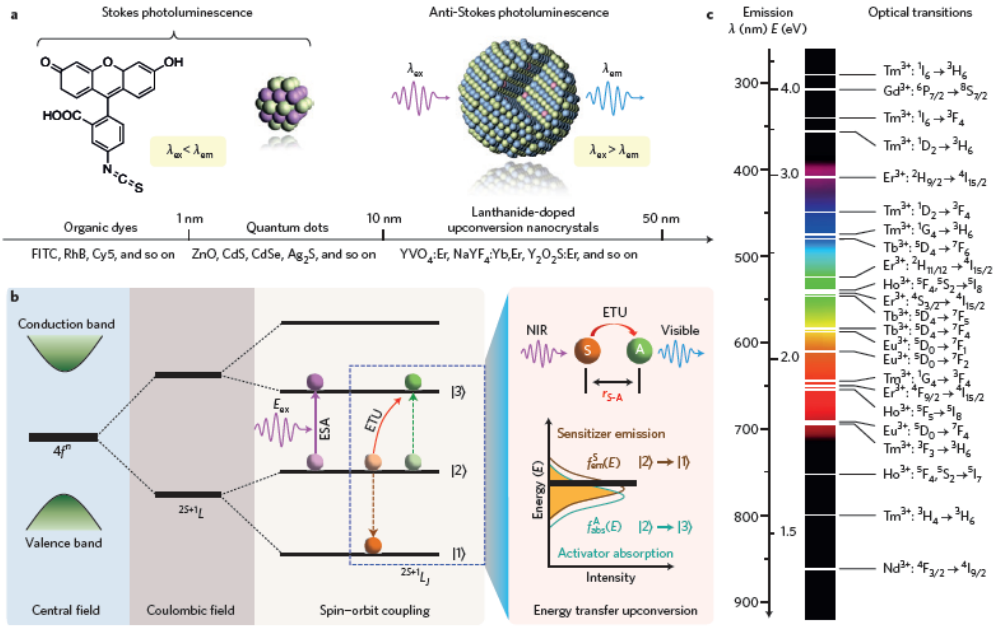

FIGURE 1-17 Lanthanide-doped nanoparticles and photon upconversion. (a)A comparison of three distinct classes of luminescent nanomaterials: organic dyes (left), semiconductor quantum dots (middle) and lanthanide-doped nanoparticles (right). (b)Electronic energy level diagrams of trivalent Ln^{3+} ions in relation to upconversion processes. The $4f_n$ electronic configuration splits into many energy sublevels due to the strong effects of the Coulombic interaction and spin–orbit coupling as well as weak crystal-field perturbation. (c)Typical Ln^{3+}-based upconversion emission bands covering a broad range of wavelengths from ultraviolet (~290 nm) to NIR (~880 nm) and their corresponding main optical transitions.[94]

Photon upconversion of lanthanides (for example, Er^{3+}, Tm^{3+} and Ho^{3+}) is typically realized by either excited-state absorption (ESA) or energy transfer upconversion (ETU), in which there are long-lived intermediate states to store the energy as shown below (Fig 1-18a and b). In comparison, in the absence of such intermediate states (for example, Tb^{3+}), photon upconversion will depend on cooperative sensitisation upconversion (CSU) (Fig 1-18c), or by energy migration (EM)-mediated upconversion within a core–shell structure (Fig 1-18d). Note that in the case of the energy migration approach, Tm^{3+} is generally employed as a ladder (L) to assist energy transfer (ET) from a sensitizer ion (S) to a migratory ion (M) and then an activator ion (A).

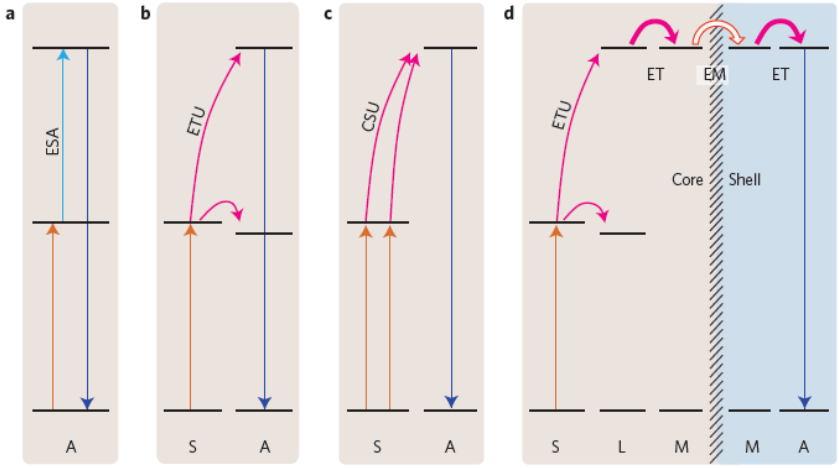

FIGURE 1-18 Photon upconversion of lanthanides

To obtain high-quality upconversion nanocrystals, many efforts have been devoted to developing facile synthetic methods, such as co-precipitation, thermal decomposition, hydro(solvo)thermal synthesis, sol–gel and microwave-assisted synthesis. As a result, a wealth of compounds ranging from oxides (for example, Y_2O_3, ZnO and $Yb_3Al_5O_{12}$) to fluorides (for example, CaF_2, $NaYF_4$ and $KMnF_3$) have been synthesized and studied as host materials, among which hexagonal-phase $NaYF_4$ was acknowledged to be one of the most efficient upconversion hosts[94]. The availability of these versatile, readily scalable methods builds up the solid foundation necessary to implement the commercialization of upconversion nanomaterials.

Research on upconversion nanocrystals has made significant progress over the past decade. Their unique merits, including multi-color emission capability under single-wavelength excitation, high signal-to-noise ratio, low cytotoxicity, long lifetime and high chemical- and photo-stability, are particularly attractive to biosensing and imaging. One limitation of upconversion nanocrystals however is the relatively low quantum efficiency (a few percent), but this can be offset using gated-detection system which take advantage of the long luminescence lifetime to give very high signal-to-background ratios.

1.5 Thesis Outline

Motivated by the above identified opportunities, my PhD program has been designed with to the aim of solving the key problem of high depletion intensities required for STED super-resolution microscopy, which seriously restricts application of STED microscopy in biology. The following result chapters 2 to 5, as the core of my PhD thesis, have been designed to explore new solutions for STED microscopy with the feathers of rare-earth upconversion nanocrystals.

Chapter 2 reports the published results (*Plos One* 2012) for a continuous wavelength STED(CW STED) microscope based on a Ti:Sapphire Oscillator. This work focuses on the CW STED with less complexity in system set-up and biological applications under super-resolution condition. We established a CW STED microscopy based on a Ti:Sapphire Oscillator working in CW mode to achieve ~71nm super-resolution on 20 nm fluorescent nanoparticles. Then three components of cellular skeleton and RNA were imaged in fixed cells with super-resolution. The results presented show that the continuous-wave mode can substantially reduce the systemic complexity and cost. However, the extreme depletion intensity condition to achieve improved resolution remains unsuitable for live cell imaging.

In chapter 3 I presented the preliminary experiments on lower power STED imaging with upconversion nanocrystals. Our initial investigation of highly-doped $NaYF_4$:Yb^{3+}/Tm^{3+} upconversion nanocrystals has been reported on *Nature Nanotechnology* in 2014. We have further explored application of these upconversion nanocrystals in stimulated emission depletion microscopy. Taking advantage of the long lifetime and high brightness of these nanocrystals, we aimed to solve the major challenge of extreme depletion intensity required for conventional STED process. With simulation and controlled measurement on low dopant and high dopant emitter concentration samples, we successfully demonstrated low power stimulated emission depletion of Tm^{3+} highly doped upconversion nanocrystals with an innovative intermediate-state depletion mechanism. Meanwhile we observed absorption and fluorescent signal enhancement on low dopant concentration samples. We achieved sub-40-nm super-resolution imaging results with much lower intensity on 6% Tm^{3+} dopant samples.

Chapter 4 reports the published results (*Nature* 2017) of lower power STED

super-resolution based on the photon avalanche mechanism in $NaYF_4:Yb^{3+}/Tm^{3+}$ upconversion nanocrystals, applying the innovative intermediate-state depletion mechanism. The measurement of depletion efficiency on variable dopant concentrations nanoparticles proved that for highly doped samples, the saturation intensity could be largely reduced; comparing to standard organic dyes, depletion intensity could be reduced by two orders of magnitude for 8% and 4% Tm^{3+}-doped samples. Additionally we were able to image the high dopant concentration nanoparticles to achieve super-resolution as low as 30 nm. We have studied the mechanism for the low intensity depletion on highly doped upconversion nanocrystals and found that the rate of the cross-relaxation inside the upconversion system can be significantly enhanced with high dopant concentration. This leads to photon avalanche in the intermediate states and eventually population inversion. A range of factors which affect the overall excitation-depletion process are reported.

Finally, Chapter 5 summarises the key outcomes of this thesis, and discusses the future prospects for this technology. Also presented are some preliminary data on an investigation of using tunable luminescent lifetime for lifetime coding and decoding. We aim to combine this with STED to further broaden the applications.

References

1 Abbe E. Beiträge zur Theorie des Mikroskops und der mikroskopischen Wahrnehmung. Archiv für mikroskopische Anatomie 1873, 9, 413-418.

2 Smith K, Oatley C. The scanning electron microscope and its fields of application. British Journal of Applied Physics 1955, 6, 391.

3 Williams DB, Carter CB. The transmission electron microscope. (Springer, 1996).

4 Binnig G, Quate CF, Gerber C. Atomic force microscope. Physical review letters 1986, 56, 930.

5 Binnig G, Rohrer H. Scanning tunneling microscopy. IBM Journal of research and development 2000, 44, 279.

6 Ohara PT, Buck RC. Contact guidance in vitro: a light, transmission, and scanning electron microscopic study. Experimental cell research 1979, 121, 235-249.

7 Putnam WP. Non-destructive electron microscopy through interaction-free quantum measurement, Massachusetts Institute of Technology, (2008).

8 Takaku Y, Suzuki H, Ohta I et al. A thin polymer membrane, nano-suit, enhancing survival across the continuum between air and high vacuum. Proceedings of the National Academy of Sciences 2013, 110, 7631-7635.

9 Gwynne P, Page G. Laboratory and technology trends: fluorescence and labeling. Science 2000, 288, 1081-1091.

10 Lichtman JW, Conchello J-A. Fluorescence microscopy. Nature methods 2005, 2, 910-919.

11 Chalfie M, Tu Y, Euskirchen G et al. Green fluorescent protein as a marker for gene expression. Science 1994, 263, 802-805.

12 Lloyd CW. The plant cytoskeleton: the impact of fluorescence microscopy. Annual review of plant physiology 1987, 38, 119-137.

13 Pepperkok R, Ellenberg J. High-throughput fluorescence microscopy for systems biology. Nature Reviews Molecular Cell Biology 2006, 7, 690-696.

14 Palmer RJ, Sternberg C. Modern microscopy in biofilm research: confocal microscopy and other approaches. Current opinion in biotechnology 1999, 10, 263-268.

15 Halbhuber K-J, König K. Modern laser scanning microscopy in biology, biotechnology and medicine. Annals of Anatomy-Anatomischer Anzeiger 2003, 185, 1-20.

16 Minsky M. Memoir on inventing the confocal scanning microscope. Scanning 1988, 10, 128-138.

17 Amos W, White J. How the confocal laser scanning microscope entered biological research. Biology of the Cell 2003, 95, 335-342.

18 Webb RH. Confocal optical microscopy. Reports on Progress in Physics 1996, 59, 427.

19 Wilson T. Confocal microscopy. Academic Press: London, etc 1990, 426, 1-64.

20 Török P, Wilson T. Rigorous theory for axial resolution in confocal microscopes. Optics communications 1997, 137, 127-135.

21 Pawley J, Masters BR. Handbook of biological confocal microscopy. Optical Engineering 1996, 35, 2765-2766.

22 Denk W, Strickler JH, Webb WW. Two-photon laser scanning fluorescence microscopy. Science 1990, 248, 73-76.

23 Göppert‐Mayer M. Über elementarakte mit zwei quantensprüngen. Annalen der Physik 1931, 401, 273-294.

24 Grzybowski A, Pietrzak K. Maria Goeppert-Mayer (1906–1972): Two-photon effect on dermatology. Clinics in dermatology 2013, 31, 221-225.

25 Kaiser W, Garrett C. Two-Photon Excitation in CaF2:Eu2+. Physical review letters 1961, 7, 229.

26 Abella I. Optical double-photon absorption in cesium vapor. Physical Review Letters 1962, 9, 453.

27 So PT, Dong CY, Masters BR et al. Two-photon excitation fluorescence microscopy. Annual review of biomedical engineering 2000, 2, 399-429.

28 Pastirk I, Dela Cruz J, Walowicz K et al. Selective two-photon microscopy with shaped femtosecond pulses. Optics express 2003, 11, 1695-1701.

29 Denk W, Piston DW, Webb WW. in Handbook of biological confocal microscopy (Springer, 1995).

30 Sánchez EJ, Novotny L, Xie XS. Near-field fluorescence microscopy based on two-photon excitation with metal tips. Physical Review Letters 1999, 82, 4014.

31 Bewersdorf J, Schmidt R, Hell S. Comparison of I5M and 4Pi‐microscopy. Journal of microscopy 2006, 222, 105-117.

32 Gustafsson M, Agard D, Sedat J. I5M: 3D widefield light microscopy with better than 100nm axial resolution. Journal of microscopy 1999, 195, 10-16.

33 Hell SW, Lindek S, Cremer C et al. Measurement of the 4pi - confocal point spread function proves 75 nm axial resolution. Applied Physics Letters 1994, 64, 1335-1337.

34 Hell SW, Lindek S, Stelzer EH. Enhancing the axial resolution in far-field light microscopy: two-photon 4Pi confocal fluorescence microscopy. 1994.

35 Truong TV, Supatto W, Koos DS et al. Deep and fast live imaging with two-photon scanned light-sheet microscopy. Nature Methods 2011, 8, 757-760.

36 Keller PJ, Schmidt AD, Santella A et al. Fast, high-contrast imaging of animal development with scanned light sheet-based structured-illumination microscopy. Nature methods 2010, 7, 637-642.

37 Weber M, Huisken J. Light sheet microscopy for real-time developmental biology. Current opinion in genetics & development 2011, 21, 566-572.

38 Keller PJ, Schmidt AD, Wittbrodt J et al. Reconstruction of zebrafish early embryonic development by scanned light sheet microscopy. science 2008, 322, 1065-1069.

39 Fahrbach FO, Gurchenkov V, Alessandri K et al. Light-sheet microscopy in thick media using scanned Bessel beams and two-photon fluorescence excitation. Optics express 2013, 21, 13824-13839.

40 Hell SW. Toward fluorescence nanoscopy. Nature biotechnology 2003, 21, 1347-1355.

41 Hell SW, Wichmann J. Breaking the diffraction resolution limit by stimulated emission: stimulated-emission-depletion fluorescence microscopy. Optics letters 1994, 19, 780-782.

42 Klar TA, Engel E, Hell SW. Breaking Abbe's diffraction resolution limit in fluorescence microscopy with stimulated emission depletion beams of various shapes. Physical Review E 2001, 64, 066613.

43 Huang B, Bates M, Zhuang X. Super resolution fluorescence microscopy. Annual review of biochemistry 2009, 78, 993.

44 Fernández-Suárez M, Ting AY. Fluorescent probes for super-resolution imaging in living cells. Nature Reviews Molecular Cell Biology 2008, 9, 929-943.

45 Gustafsson MG. Surpassing the lateral resolution limit by a factor of two using structured illumination microscopy. Journal of microscopy 2000, 198, 82-87.

46 Gustafsson MG. Nonlinear structured-illumination microscopy: wide-field fluorescence imaging with theoretically unlimited resolution. Proceedings of the National Academy of Sciences of the United States of America 2005, 102, 13081-13086.

47 Willig KI, Rizzoli SO, Westphal V et al. STED microscopy reveals that synaptotagmin remains clustered after synaptic vesicle exocytosis. Nature 2006, 440, 935-939.

48 Rust MJ, Bates M, Zhuang X. Sub-diffraction-limit imaging by stochastic optical reconstruction microscopy (STORM). Nature methods 2006, 3, 793-796.

49 Dyba M, Jakobs S, Hell SW. Immunofluorescence stimulated emission depletion microscopy. Nature biotechnology 2003, 21, 1303-1304.

50 Shao L, Kner P, Rego EH et al. Super-resolution 3D microscopy of live whole cells using structured illumination. Nature methods 2011, 8, 1044-1046.

51 York AG, Parekh SH, Dalle Nogare D et al. Resolution doubling in live, multicellular organisms via multifocal structured illumination microscopy. Nature methods 2012, 9, 749-754.

52 Betzig E, Patterson GH, Sougrat R et al. Imaging intracellular fluorescent proteins at nanometer resolution. Science 2006, 313, 1642-1645.

53 Hess ST, Girirajan TP, Mason MD. Ultra-high resolution imaging by fluorescence photoactivation localization microscopy. Biophysical journal 2006, 91, 4258-4272.

54 Hell SW, Kroug M. Ground-state-depletion fluorscence microscopy: A concept for breaking the diffraction resolution limit. Applied Physics B 1995, 60, 495-497.

55 Hofmann M, Eggeling C, Jakobs S et al. Breaking the diffraction barrier in fluorescence microscopy at low light intensities by using reversibly photoswitchable proteins. Proceedings of the National Academy of Sciences of the United States of America 2005, 102, 17565-17569.

56 Leutenegger M, Eggeling C, Hell SW. Analytical description of STED microscopy performance. Optics express 2010, 18, 26417-26429.

57 Schrader M, Meinecke F, Bahlmann K et al. Monitoring the excited state of a fluorophore in a microscope by stimulated emission. Bioimaging 1995, 3, 147-153.

58 Willig KI, Harke B, Medda R et al. STED microscopy with continuous wave beams. Nature methods 2007, 4, 915-918.

59 Vicidomini G, Moneron G, Han KY et al. Sharper low-power STED nanoscopy by time gating. Nature methods 2011, 8, 571-573.

60 Hell SW. Fluorescence nanoscopy: breaking the diffraction barrier by the RESOLFT concept. Nanobiotechnology 2005, 1, 296-297.

61 Sauer M. Reversible molecular photoswitches: A key technology for nanoscience and fluorescence imaging. Proceedings of the National Academy of Sciences of the United States of America 2005, 102, 9433-9434.

62 Fölling J, Bossi M, Bock H et al. Fluorescence nanoscopy by ground-state depletion and single-molecule return. Nature methods 2008, 5, 943-945.

63 Rittweger E, Wildanger D, Hell S. Far-field fluorescence nanoscopy of diamond color centers by ground state depletion. EPL (Europhysics Letters) 2009, 86, 14001.

64 Deniz E, Tomasulo M, DeFazio RA et al. Fluorescence patterning in films of a photoswitchable BODIPY–spiropyran dyad. Physical Chemistry Chemical Physics 2010, 12, 11630-11634.

65 Heilemann M, Dedecker P, Hofkens J et al. Photoswitches: Key molecules for subdiffraction - resolution fluorescence imaging and molecular quantification. Laser & Photonics Reviews 2009, 3, 180-202.

66 Hell SW, Willig KI, Dyba M et al. Nanoscale resolution with focused light: STED and other RESOLFT microscopy concepts. Handbook of biological confocal microscopy 2006, 571-579.

67 Willig KI, Kellner RR, Medda R et al. Nanoscale resolution in GFP-based microscopy. Nature Methods 2006, 3, 721.

68 Gustafsson MG, Shao L, Carlton PM et al. Three-dimensional resolution doubling in wide-field fluorescence microscopy by structured illumination. Biophysical journal 2008, 94, 4957-4970.

69 Hirvonen LM, Wicker K, Mandula O et al. Structured illumination microscopy of a living cell. European Biophysics Journal 2009, 38, 807-812.

70 Heintzmann R, Jovin TM, Cremer C. Saturated patterned excitation microscopy—a concept for optical resolution improvement. JOSA A 2002, 19, 1599-1609.

71 Gur A, Zalevsky Z, Micó V et al. The limitations of nonlinear fluorescence effect in super resolution saturated structured illumination microscopy system. Journal of fluorescence 2011, 21, 1075-1082.

72 Mortensen KI, Churchman LS, Spudich JA et al. Optimized localization analysis for single-molecule tracking and super-resolution microscopy. nature methods 2010, 7, 377-381.

73 Waterman-Storer CM, Desai A, Bulinski JC et al. Fluorescent speckle microscopy, a method to visualize the dynamics of protein assemblies in living cells. Current biology 1998, 8, 1227-S1221.

74 Thompson RE, Larson DR, Webb WW. Precise nanometer localization analysis for individual fluorescent probes. Biophysical journal 2002, 82, 2775-2783.

75 Subach FV, Patterson GH, Manley S et al. Photoactivatable mCherry for high-resolution two-color fluorescence microscopy. Nature methods 2009, 6, 153-159.

76 Huang B, Wang W, Bates M et al. Three-dimensional super-resolution imaging by stochastic optical reconstruction microscopy. Science 2008, 319, 810-813.

77 Bates M, Huang B, Dempsey GT et al. Multicolor super-resolution imaging with photo-switchable fluorescent probes. Science 2007, 317, 1749-1753.

78 Patterson GH, Lippincott-Schwartz J. A photoactivatable GFP for selective photolabeling of proteins and cells. Science 2002, 297, 1873-1877.

79 Hell SW. Far-field optical nanoscopy. science 2007, 316, 1153-1158.

80 Fölling J, Belov V, Kunetsky R et al. Photochromic rhodamines provide nanoscopy with optical sectioning. Angewandte Chemie International Edition 2007, 46, 6266-6270.

81 Shroff H, Galbraith CG, Galbraith JA et al. Live-cell photoactivated localization microscopy of nanoscale adhesion dynamics. Nature methods 2008, 5, 417-423.

82 Shaevitz JW. Super-resolution for a 3D world. Nature methods 2008, 5, 471-473.

83 Klar TA, Jakobs S, Dyba M et al. Fluorescence microscopy with diffraction resolution barrier broken by stimulated emission. Proceedings of the National Academy of Sciences 2000, 97, 8206-8210.

84 Liu Y, Lu Y, Yang X et al. Amplified stimulated emission in upconversion nanoparticles for super-resolution nanoscopy. Nature 2017, advance online publication.

85 Rittweger E, Han KY, Irvine SE et al. STED microscopy reveals crystal colour centres with nanometric resolution. Nature Photonics 2009, 3, 144-147.

86 Hanne J, Falk HJ, Görlitz F et al. STED nanoscopy with fluorescent quantum dots. Nature communications 2015, 6.

87 Hein B, Willig KI, Hell SW. Stimulated emission depletion (STED) nanoscopy of a fluorescent protein-labeled organelle inside a living cell. Proceedings of the National Academy of Sciences 2008, 105, 14271-14276.

88 Liu Y, Ding Y, Alonas E et al. Achieving λ/10 resolution CW STED nanoscopy with a Ti: sapphire oscillator. PloS one 2012, 7, e40003.

89 Westphal V, Rizzoli SO, Lauterbach MA et al. Video-rate far-field optical nanoscopy dissects synaptic vesicle movement. Science 2008, 320, 246-249.

90 Moneron G, Medda R, Hein B et al. Fast STED microscopy with continuous wave fiber lasers. Optics express 2010, 18, 1302-1309.

91 Irvine SE, Staudt T, Rittweger E et al. Direct light‐driven modulation of luminescence from Mn‐doped ZnSe quantum dots. Angewandte Chemie 2008, 120, 2725-2728.

92 Michalet X, Pinaud F, Bentolila L et al. Quantum dots for live cells, in vivo imaging, and diagnostics. science 2005, 307, 538-544.

93 Alivisatos AP. Semiconductor clusters, nanocrystals, and quantum dots. Science 1996, 271, 933.

94 Zhou B, Shi B, Jin D et al. Controlling upconversion nanocrystals for emerging applications. Nature nanotechnology 2015, 10, 924-936.

95 Heer S, Kömpe K, Güdel HU et al. Highly Efficient Multicolour Upconversion Emission in Transparent Colloids of Lanthanide‐Doped NaYF4 Nanocrystals. Advanced Materials 2004, 16, 2102-2105.

96 Song Z, Anissimov YG, Zhao J et al. Background free imaging of upconversion nanoparticle distribution in human skin. Journal of biomedical optics 2013, 18, 061215-061215.

Chapter 2

This chapter explores the design and evaluation of a synchronisation-free continuous wave stimulated emission depletion (CW-STED) super-resolution nanoscopy system. A Ti:Sapphire oscillator, which is commonly used for multi-photon microscopy, was employed to generate the depletion beam with wavelength tunability in CW mode. This enabled easy optimisation for the depletion wavelength to suit different fluorescent dyes, allowed us to resolve the fine subcellular structures at ~70 nm resolution. This work is reported in the form of a published journal paper.

2.1 Contributions to Paper 1

TABLE 2-1 Author contribution summary for paper 1.

	Y.L.	Y.D.	E.A.	W.Z.	P.J.S.	J.D.	J.A.P.	J.T.	Q.R.	P.X.
Experiment Design	•					•	•		•	•
System Setup	•	•								
Sample Preparation	•		•	•	•			•		
Data Collection	•									
Analysis	•									•
Manuscript and Figures	•				•	•				•

My supervisors and I designed the project. I led the major experimental work, including system design and setup, alignment and evaluation, and data acquisition. My colleagues and I prepared the samples. I also led data analysis and manuscript preparation.

2.2 Paper 1

Liu Y, Ding Y, Alonas E, Zhao W, Santangelo PJ, Jin D, Piper J A, Teng J, Ren Q, Xi P, "Achieving λ/10 Resolution CW STED Nanoscopy with a Ti:Sapphire Oscillator". *PLoS ONE* **7**(6) e40003,doi: 10.1371/ journal. pone. 0040003.

(Article first published online: 27 June 2012)

OPEN ACCESS Freely available online PLoS one

Achieving λ/10 Resolution CW STED Nanoscopy with a Ti:Sapphire Oscillator

Yujia Liu[1,2], Yichen Ding[2], Eric Alonas[3], Wenli Zhao[5], Philip J. Santangelo[3], Dayong Jin[4], James A. Piper[4], Junlin Teng[5], Qiushi Ren[1,2], Peng Xi[2]*

1 School of Biomedical Engineering, Shanghai Jiao Tong University, Shanghai, China, **2** Department of Biomedical Engineering, College of Engineering, Peking University, Beijing, China, **3** Wallace H Coulter Department of Biomedical Engineering, Georgia Institute of Technology and Emory University, Atlanta, Georgia, United States of America, **4** Advanced Cytometry Labs, MQphotonics Research Centre, Macquarie University, Sydney, New South Wales, Australia, **5** College of Life Sciences, Peking University, Beijing, China

Abstract

In this report, a Ti:Sapphire oscillator was utilized to realize synchronization-free stimulated emission depletion (STED) microscopy. With pump power of 4.6 W and sample irradiance of 310 mW, we achieved super-resolution as high as 71 nm. With synchronization-free STED, we imaged 200 nm nanospheres as well as all three cytoskeletal elements (microtubules, intermediate filaments, and actin filaments), clearly demonstrating the resolving power of synchronization-free STED over conventional diffraction limited imaging. It also allowed us to discover that, Dylight 650, exhibits improved performance over ATTO647N, a fluorophore frequently used in STED. Furthermore, we applied synchronization-free STED to image fluorescently-labeled intracellular viral RNA granules, which otherwise cannot be differentiated by confocal microscopy. Thanks to the widely available Ti:Sapphire oscillators in multiphoton imaging system, this work suggests easier access to setup super-resolution microscope via the synchronization-free STED.

Citation: Liu Y, Ding Y, Alonas E, Zhao W, Santangelo PJ, et al. (2012) Achieving λ/10 Resolution CW STED Nanoscopy with a Ti:Sapphire Oscillator. PLoS ONE 7(6): e40003. doi:10.1371/journal.pone.0040003

Editor: Jörg Langowski, German Cancer Research Center, Germany

Received April 30, 2012; **Accepted** May 30, 2012; **Published** June 27, 2012

Funding: This research is supported by the "973" Major State Basic Research Development Program of China (2011CB809101, 2010CB933901, 2011CB707502), the National Natural Science Foundation of China (61178076), PKU-GT/Emory University BME Seed Grant funded by Wallace H. Coulter Foundation, and seed fund support from Olympus Australia. The funders had no role in study design, data collection and analysis, decision to publish, or preparation of the manuscript.

Competing Interests: Part of this research is sponsored by Olympus Australia, however this does not alter the authors' adherence to all the PLoS ONE policies on sharing data and materials.

* E-mail: xipeng@pku.edu.cn

Introduction

Fluorescence microscopy has become an essential tool to study biological molecules, pathways and events in living cells, tissues and animals. Its key advantages over other forms of microscopy arise from the use of specific, minimally invasive molecular staining and compatibility with living cells. Fluorescence microscopes with the most advanced confocal geometries available yield optical resolution approaching the theoretical Abbe diffraction limit of ~ 200 nm, but this is still larger than many subcellular structures, which are too small to be observed in detail. These limitations have driven the development of super-resolution optical imaging methodologies over the past decade, and have significantly impacted many fields of science [1,2,3,4,5].

Bypassing the optical diffraction limit in far-field optical microscopy has been realized by two key pioneering concepts: spatially patterned excitation with emission inhibition, such as Stimulated Emission Depletion (STED) microscopy [6,7,8] and Saturated Structured Illumination Microscopy (SSIM) [9,10]; and high-precision localization of single fluorophores through individual activation, such as STochastic Optical Reconstruction Microscopy (STORM) [11,12] and Photo-Activated Localization Microscopy (PALM) [13]. Stimulated Emission Depletion (STED) was the first and most direct approach to overcoming the diffraction limit for far-field nanoscopy. STED microscopy uses an intense doughnut-shaped beam surrounding the excitation focus to switch the fluorophore(s) in the sample to a "dark" state through stimulated emission. This effectively eliminates the periphery of the Point Spread Function (PSF), resulting in a narrower PSF, or super-resolution.

The depletion efficiency of STED can be optimized with the pulsed excitation and the temporal delayed pulsed STED beam [7]. This requires precise synchronization of two laser pulses and maintenance of the accurate time delay [14,15,16,17,18,19,20]. To meet these requirements, either a laser diode was specially designed with a rather sophisticated optical or electrical delay line [14,15,16,17,18], or a single laser was used to generate both excitation and STED pulses to minimize synchronization steps [19,20]. Continuous Wave (CW) STED, with both excitation and STED beams in CW mode, can be engineered based on spectral discrimination of the spontaneous emission and stimulated emission of the fluorescent molecules, and has been successfully applied to image neurofilaments in neuroblastoma cells [21], syntaxin clusters in the cell membrane [21], the nuclear lamina of mammalian cells [21], and the endoplasmic reticulum of living cells [22]. CW STED is beneficial because it is synchronization-free, and requires no pulse length or timing optimization for the excitation and depletion beams. This characteristic makes it easier to adapt to a conventional confocal fluorescence configurations. Previous reports of CW STED utilized either high pump power laser systems [21], or the combination of multiple

fiber lasers [22]. However, these lasers are not readily available in biomedical instrumentation labs, which might explain their limited use. The only other current option for CW STED are commercial microscopes, but these are prohibitively expensive for most users.

On the other hand, the Ti:Sapphire laser has recently been used as both an excitation and depletion source in a two-photon STED system for super-resolution neuron imaging [23]; as well as for single-laser, single-wavelength STED nanoscopy [24]. The work presented here further expands the application of Ti:Sapphire lasers to STED nanoscopy.

In this paper, we demonstrated a synchronization-free CW STED microscope using a 6 Watt Diode-Pumped Solid State (DPSS) 532 nm laser pumped Ti:Sapphire oscillator tuned to CW mode, which is a source broadly available in many two-photon microscope systems [25,26,27,28,29]. Taking advantage of the wavelength tunability of the Ti:Sapphire laser, the depletion wavelength was optimized for different dyes. Using this system we demonstrated a super-resolution of 71 nm, and resolved the fine structures of actin filaments, intermediate filaments, and microtubules. In situations where optical deconvolution fails to interpret the structure of aggregated nanospheres, CW STED can correctly discern the nanospheres with ~200 nm distance. Interestingly, a pair of parallel actin filaments, 240 nm from each other, was clearly imaged with STED, which could be misinterpreted as with a double-helix structure in confocal microscopy due to the lack of sufficient resolution. Furthermore, we applied the CW STED for the first time to visualize the viral genomic RNA of human respiratory syncytial virus (hRSV) in HEp-2 cells resulting in a high-resolution image clearly showing individual RNA granules. Moreover, we demonstrated the utility of Dylight 650 as a far-red dye suitable for STED microscopy with improved depletion efficiency.

Results

Figure 1 illustrates the schematic setup and preliminary evaluation of the stimulated emission depletion efficiencies on different fluorescent dyes (1d). We employed a vortex 0–2π phase plate to generate the doughnut shaped depletion beam

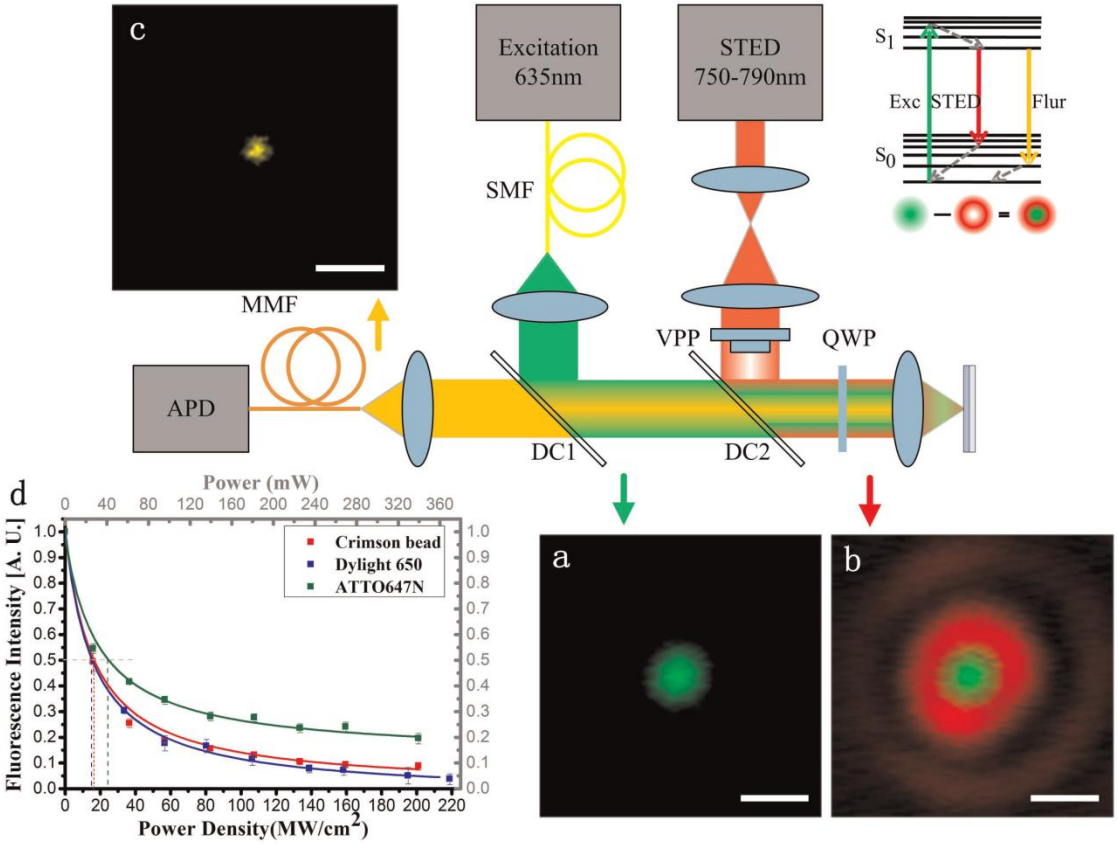

Figure 1. Schematic of the CW STED system for far-field super-resolution optical nanoscopy. The green line represents the excitation 635 nm laser, red line is the CW Ti: Sapphire STED beam, and the yellow line represents the fluorescence signal. SMF: single mode fiber; MMF: multi-mode fiber; DC1 and DC2 are dichotic filters. VPP: vortex 0–2π phase plate; QWP: quarter waveplate. The excitation PSF (a), doughnut depletion PSF overlapped with excitation PSF (b), and STED PSF (c) clearly shows the process of achieving super-resolution. Scale bar: 500 nm. The modulation efficiency versus the depletion intensity was measured with crimson beads, DyLight 650 and ATTO 647N solution (d). The STED wavelengths are 763 nm for crimson beads and ATTO 647N, and 783 nm for DyLight 650.
doi:10.1371/journal.pone.0040003.g001

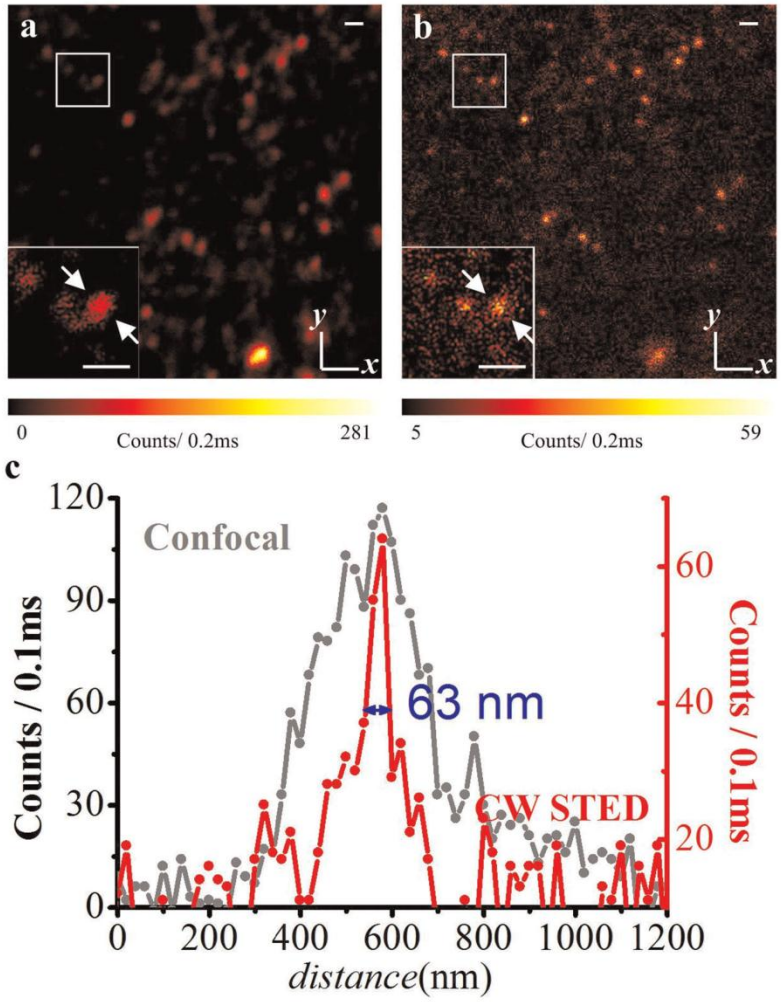

Figure 2. Confocal and corresponding CW-STED images of fluorescent 20-nm-diameter nanospheres. (a) Confocal; (b) CW-STED; (c) The profile along the dashed line in (a) and (b) exhibits a spot size of 63 nm, indicating an effective resolution of ~59 nm after subtraction of the bead size. Scale bar: 500 nm.
doi:10.1371/journal.pone.0040003.g002

for de-exciting the fluorescence by stimulated emission [30]. As the resolution is determined by the depletion efficiency, not the diffraction limit, we first studied the effect of the depletion ratio η_{CW} on the spontaneous fluorescence by overlapping the STED focus (without phase modulation) with the excitation focus [31]. As shown in Figure 1d, the saturation intensity I_s (in which the possibility of spontaneous emission and stimulated emission is equal) is measured to be ~17 MW/cm^2 for crimson beads at 763 nm, ~14.4 MW/cm^2 for DyLight 650 at 783 nm and ~23.8 MW/cm^2 for ATTO 647N at 763 nm (the intensities are measured before the 100x objective). The saturation intensity for ATTO647N is larger than previous literatures [21,24], which may due to residual system optical aberration as well as the measurement condition, to which the extinction ratio of $\xi = I_{\mathrm{mod}}/I_s$ is insensitive. The reciprocal fitting of $\eta_{CW} = (1 + I_{\mathrm{mod}}/I_s)^{-1}$ agrees well with the experimental data. When the STED beam was switched off, the system functioned as a normal confocal system, which was used to obtain data for comparison.

The resolution of the prototype STED system was evaluated by imaging 20 nm crimson nanospheres. As shown Figure 2, at the maximum available STED power of 340 mW, the FWHM spot size was measured as small as 63 nm laterally, indicating an effective resolution of 59 nm after accounting for the size of the nanosphere [21]. With a total 20 nanospheres measured in the focal plane, the average resolution was calculated as 71 nm ±9 nm. This is in good agreement with the theoretical prediction of $d_{STED} = \frac{0.45\lambda}{NA\sqrt{1+\xi}}$. The pixel dwell time is set to 0.2 ms in all the presented images.

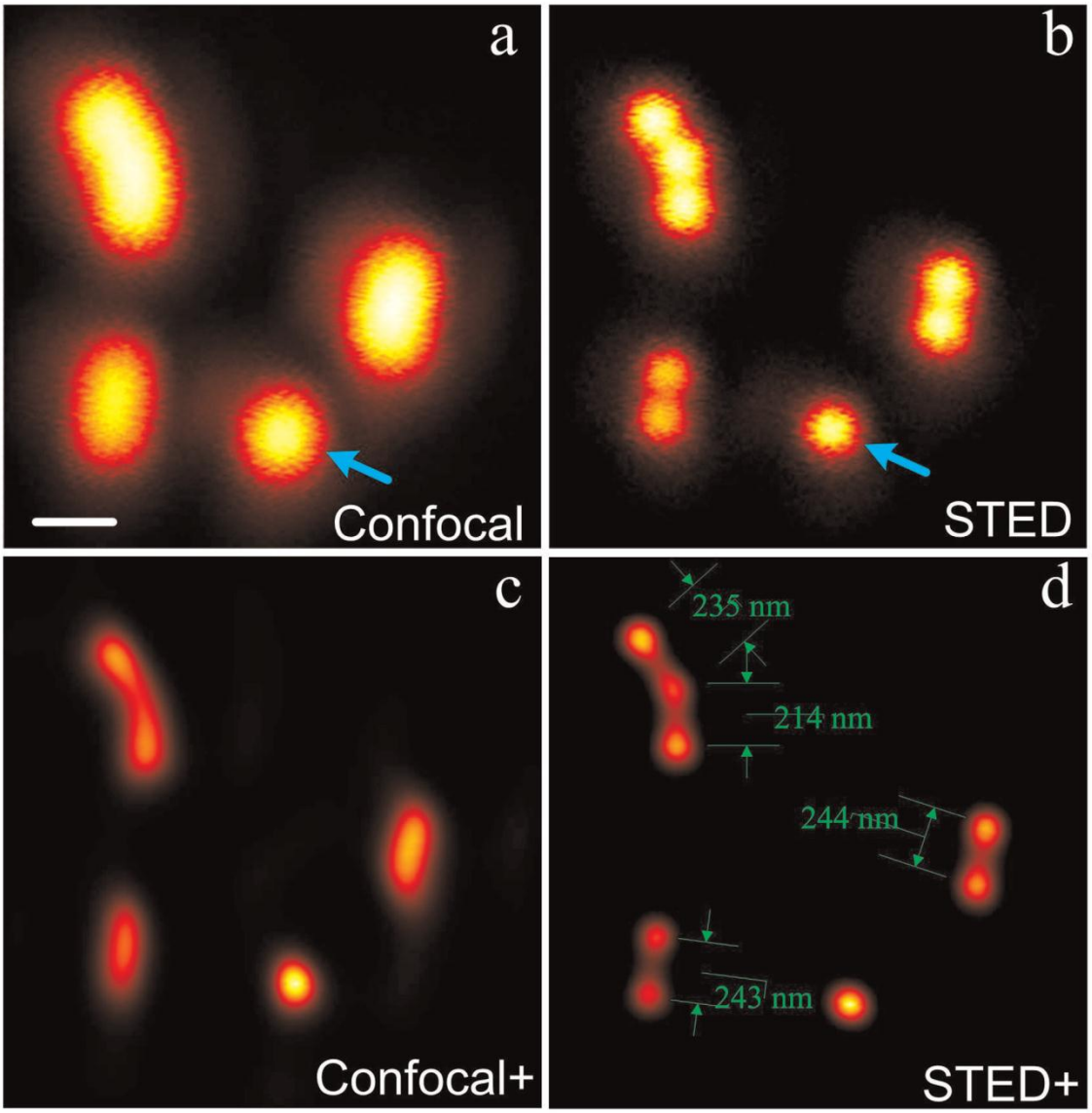

Figure 3. Comparison of diffraction-limited confocal microscopy and STED nanoscopy for fluorescent 200-nm-diameter nanospheres. (a) Confocal and (b) corresponding CW-STED images; (c) and (d) are the deconvolved results of (a) and (b). Scale bar: 500 nm.
doi:10.1371/journal.pone.0040003.g003

Figure 3 shows images of the 200 nm nanospheres on glass. Adjacent nanospheres under the confocal system (a and c) can be clearly discriminated by the super-resolution CW STED system (b and d). Though the Richardson-Lucy (R-L) deconvolution algorithm can improve the resolution of both confocal and STED images (denoted confocal+ in a versus b, and STED+ in c versus d), once the adjacent nanospheres are within the optical diffraction limit, the STED+ (Fig 3d) can discern all the spheres clearly.

To demonstrate the resolving power of the CW STED nanoscope, all three cytoskeleton filaments were imaged: microtubules, intermediate filaments (keratin), and actin filaments. From the microtubule network of Vero cells, we can see that STED nanoscopy provides ~128 nm FWHM with Dylight 650 staining (Figure 4). Because of the size of the microtubules is generally ~25 nm, its junctions are hardly resolved with conventional microscope. However, with the STED, the fine microstructure can be visualized in Figure 4b, which result can be further improved by the R-L deconvolution in Figure 4c. In comparison, Figure 5 showed the images of the intermediate filament network in PtK2 cells, a male rat kangaroo kidney epithelial cell line stained with ATTO647N. The cross-sectional diameter is measured to be

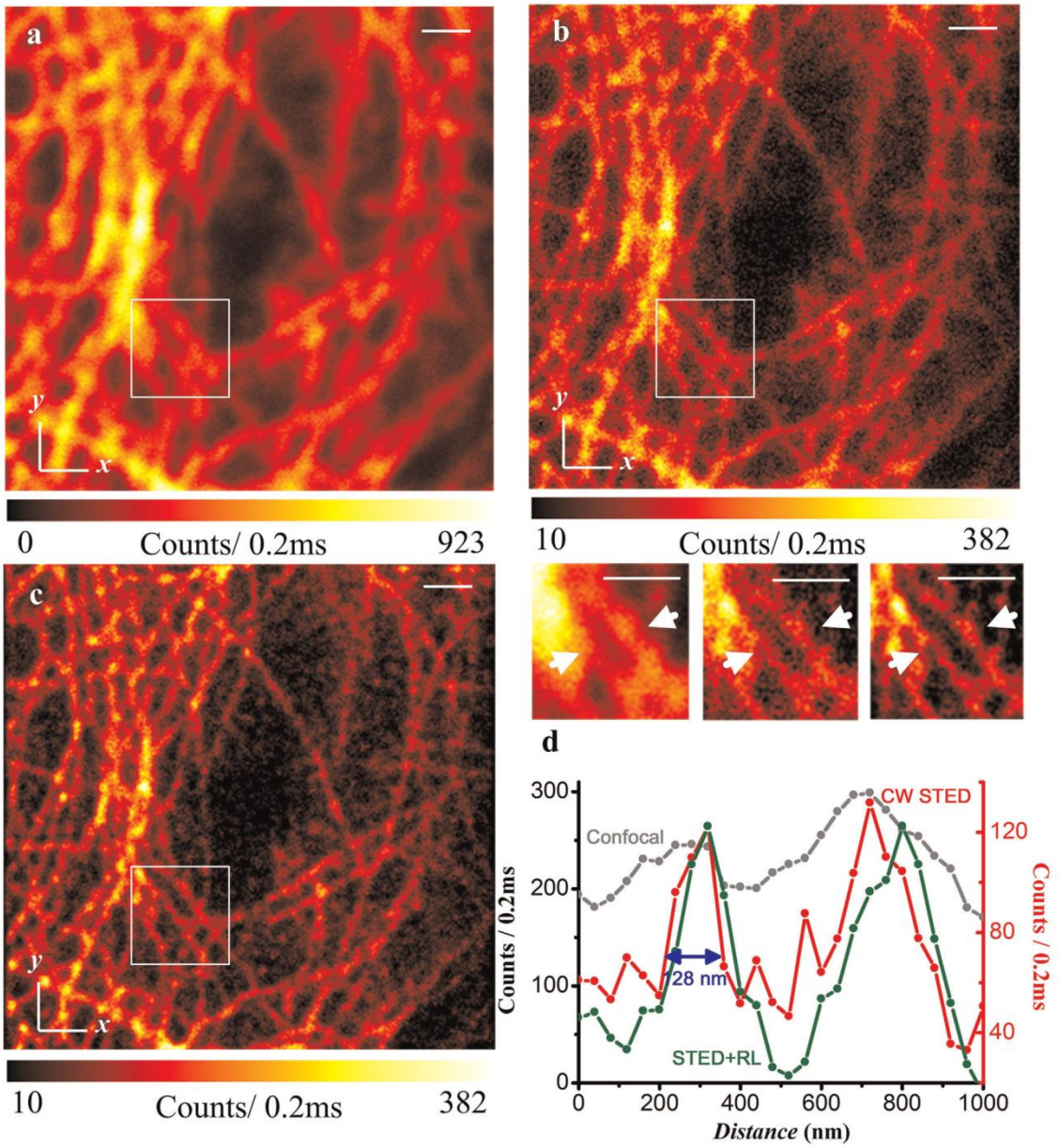

Figure 4. Confocal, corresponding CW-STED, and deconvolved STED images of microtubules in a Vero cell stained with Dylight 650. (a) Confocal; (b) CW-STED; (c) R-L deconvolution of (b). The intensity at the cross-section marked in (a), (b), and (c) inlets are plotted in (d). The wavelength and power density for the STED beam is 783 nm and ~200 MW/cm^2. Scale bar: 1 μm.
doi:10.1371/journal.pone.0040003.g004

168 nm on STED. The typical diameter of intermediate filament is ~10 nm.

Furthermore, as reported by Oliva et al., insufficient resolution may lead to aliasing of image [32]. In our actin filament imaging of HeLa cell (Figure 6), we observed what appeared to be a single twisted actin filament from the confocal microscopy; this artifact was due to resolution larger than the size (~8 nm) of filamentous actin and the lateral separation (~240 nm) between filaments. However, with the aid of CW STED, we can clearly visualize the parallel structure of the actin filaments (Figure 6e).

RNA plays a critical role in mediating and regulating gene expression. Understanding RNA localization and dynamics will not only aid in our understanding of native cellular gene expression, but will also provide information on the life cycle of

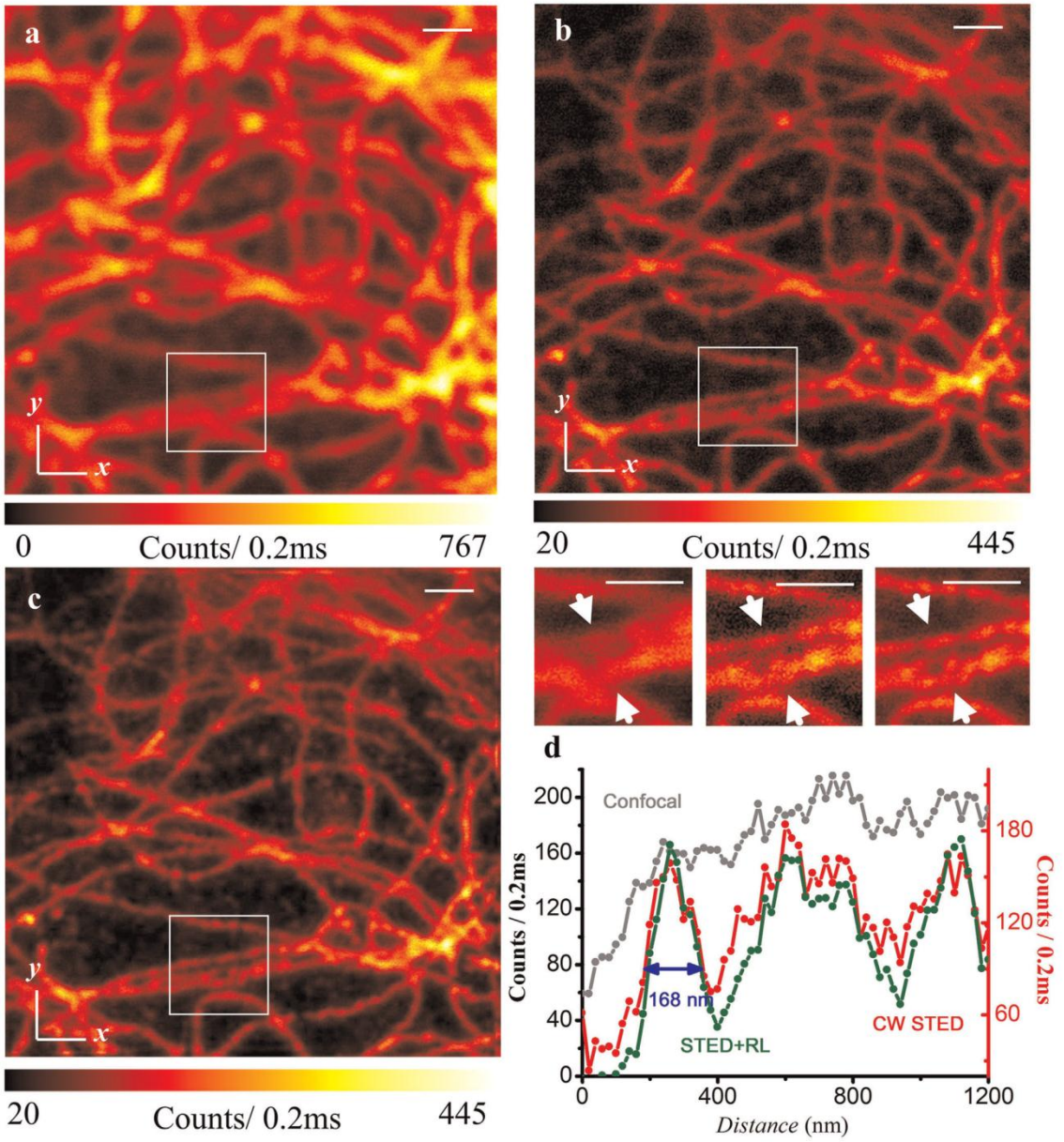

Figure 5. Confocal, corresponding CW-STED, and deconvolved STED images of keratin intermediate filaments in a PtK2 cell stained with ATTO 647N. (a) Confocal; (b) CW-STED; (c) R-L deconvolution of (b). The intensity at the cross-section marked in (a), (b), and (c) boxed regions are plotted in (d). The wavelength and power density for STED beam is 763 nm and ~200 MW/cm^2. Scale bar: 1 μm.
doi:10.1371/journal.pone.0040003.g005

RNA viruses. Given that the size of most RNA molecules is often smaller than the diffraction limit, examining RNA localization is a model problem for the application of CW STED [33]. By utilizing exogenous multiply-labeled fluorescent probes described by Santangelo et al. [34], the genomic RNA of the human respiratory syncytial virus (hRSV strain A2) during cellular infection was specifically labeled with DyLight 650-conjugated probes and imaged via CW STED. As shown in Figure 7, a resolution of 82 nm on STED was achieved comparing to 290 nm on confocal. The contrast in performance is clearly obvious in Figure 7d and e where there is a higher concentration of RNA molecules.

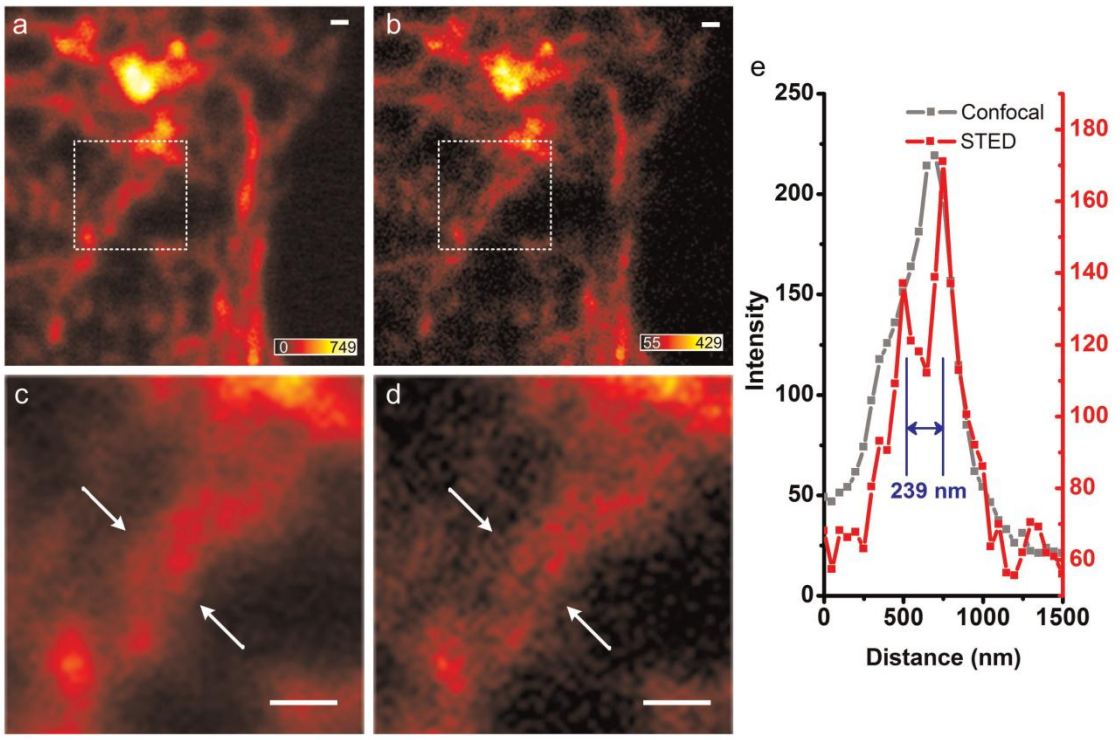

Figure 6. Confocal and corresponding CW-STED images of actin filaments in a HeLa cell. (a) Confocal; (b) CW-STED. The boxed regions in (a) and (b) are magnified in (c) and (d), respectively. The intensities at the cross-section marked in (c) and (d) are plotted in (e). The wavelength and power density for the STED beam is 763 nm and ~127 MW/cm^2. Scale bar: 500 nm.
doi:10.1371/journal.pone.0040003.g006

Discussion

STED nanoscopy has been intensively investigated over the last decade, showing great promise for imaging cellular structures. It utilizes a donut depletion beam to de-excite fluorphoes at the edges of the excitation focus, thus breaking the diffraction limit. It can operate in either pulsed mode or CW mode.The pulsed mode can easily meet the depletion intensity requirements due to the high peak pulsed power, but the precise synchronization between the pulsed excitation laser and pulsed STED laser is both crucial and difficult to achieve and maintain. The successful demonstrations of synchronization-free CW STED, however, employed high power laser or a combination of multiple lasers [21,22], which are not commonplace, thus limiting STED deployment. We report here a CW STED system with a Ti:Sapphire laser tuned to CW mode, and we achieved a super-resolution of 71 nm laterally, which is only one-tenth the emission wavelength. With super-resolution, the imaging of 200 nm nanospheres demonstrated that beads with distances beyond conventional resolution can be clearly discerned.

Two factors determine the resolution of CW STED nanoscopy: the saturation intensity of the fluorescence dye, and the depletion power applied. Here, for the first time, we have used Dylight 650 for STED nanoscopy and found that its saturation intensity is much lower than that of ATTO 647N, a commonly used STED fluorophore. This might lead to the exploration of other dyes that are more suitable for STED nanoscopy. The depletion power applied relates to two disadvantages associated with CW STED: (1) photobleaching is more pronounced due to constant excitation of the fluorophore and (2) photo-thermal damage to the specimen is possible due to the greater excitation energy applied over time. Therefore, the application of an anti-fade reagent, as well as mounting medium containing an oxygen scavenger, can improve the performance of CW STED imaging. Recent publications have reported that with the addition of Mowiol [21,35], an oxygen scavenger system [35,36], and reducing and oxidizing system [35,37], the photostability of dye molecules can change dramatically. Therefore, it will be important in future studies to further characterize and optimize sample preparation protocols for each dye used in super-resolution nanoscopy..

Here, we have applied CW STED nanoscopy to all three cytoskeleton filaments (microtubule, intermediate filaments, actin filaments), whose sizes are smaller than the resolution of a diffraction-limit microscope, to demonstrate the performance of our STED system, and succeeded in discriminating parallel actin filaments, which appeared as a single structure by confocal imaging. We further demonstrated, for the first time, that STED nanoscopy can discern the Dylight 650-MTRIP-labeled viral RNAs in HEp-2 cells, with a resolution of 82 nm. The imaging capability of CW STED demonstrated in this report should help researchers interested in setting up their own STED systems with access to Ti:Sapphire oscillators, and to further apply STED nanoscopy to a broader, more diverse set of biological problems.

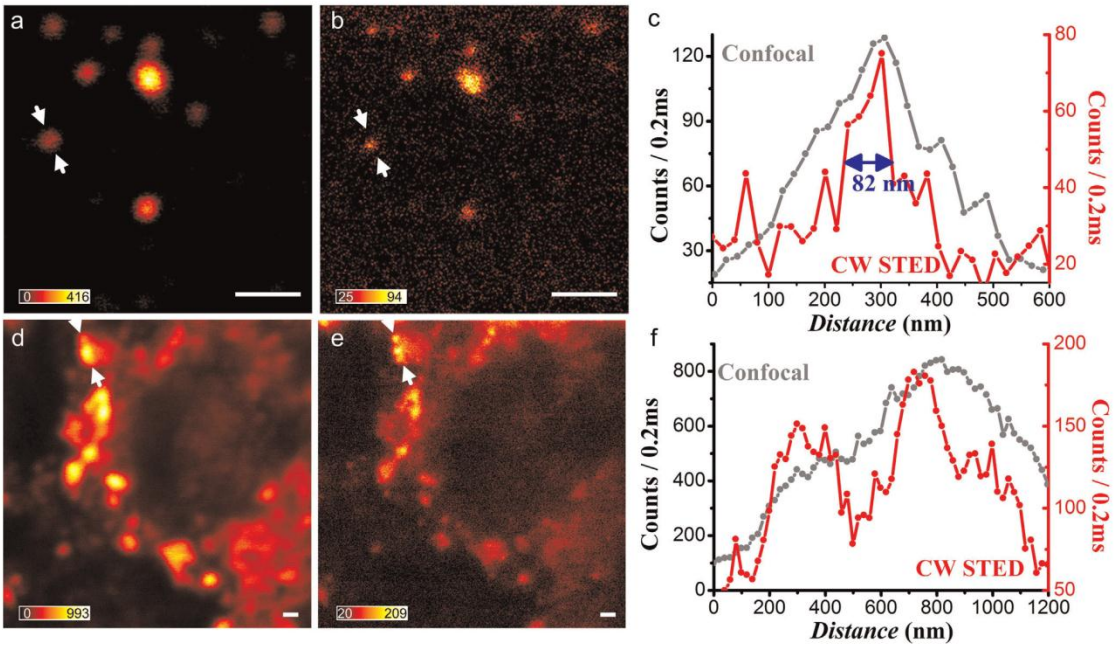

Figure 7. Confocal and corresponding CW-STED images of hRSV genomic RNA granules in a HEp2 cell. Confocal (a) and corresponding CW-STED (b) results of isolated individual RNA, as well as RNA granules images by confocal (c) and CW-STED (d) are shown. The intensity at the cross-section marked in (d) and (e) are plotted in (c, f). The wavelength and power intensity for STED beam is 783 nm and ~162 MW/cm^2. Scale bar: 1 μm.
doi:10.1371/journal.pone.0040003.g007

Materials and Methods

STED Instrumentation

The STED system was built based on a home-made confocal imaging system with 635 nm excitation. A Ti:Sapphire laser (Griffin-F, KMLabs, USA) pumped by a 6-Watt DPSS 532 nm laser (Finesse-6W, Laser Quantum, UK) was employed as the CW STED source. The output from the laser source is ~800 mW. To generate the doughnut PSF for effective depletion, a vortex 0–2π phase plate (VPP-A, RPC Photonics) was used. We focused the beams into samples using an oil-immersion objective of NA = 1.4 (100x, PlanAPO, Zeiss). To obtain a 2-D image, a piezo scanning stage (Nanomax, Thorlabs) was employed to move the specimen. A photo-counting avalanche photodiode (SPCM-AQRH-13-FC, Perkin Elmer) was used to collect the fluorescence signal. The scanning and data collection were performed with a DAQ board (USB-6259, National Instruments), and image collection was accomplished with Imspector (Max-Plank Innovation).

Cells and Viruses

Vero cells (ATCC CCL-81) were maintained in High Glucose DMEM (Lonza) with 10% FBS (Hyclone), 100 U ml-1 penicillin, and 100 μg ml^{-1} streptomycin (Invitrogen). hRSV strain A2 (ATCC VR-1544) was propagated in HEp-2 cells (ATCC CCL-23) at a titer of 1×10^6 pfu/mL. Cells were plated the day before infection at 25% confluency. Cells were infected by removing the media, washing with PBS (without Ca^{2+} and Mg^{2+}), adding virus at a multiplicity of infection (MOI) of 1, and incubating the cells for 1 h at 37°C. After adsorption, fresh medium was added to the inoculum.

Microtubule Immunofluorescence

Vero's were plated the day before fixation at 25% confluency and were fixed with 100% methanol for 10 min at −20°C and additionally permeabilized with 100% acetone for 2 min at −20°C. Nonspecific antibody binding was blocked with 5% bovine serum albumin (EMD) in PBS for 30 min at 37°C. Veros were then incubated with a primary antibody against alpha tubulin (rabbit polyclonal IgG, Abcam ab18251) for 30 min at 37°C, washed twice in PBS, and incubated with a secondary antibody (goat anti-rabbit DyLight 650 IgG, Pierce) for 30 min at 37°C, washed twice in PBS, and mounted in a mixture of Mowiol 4–88 (Sigma) and DABCO (VWR) [38].

Keratin Immunofluoresnce

The PtK2 cells (a gift of Dr. K. Willig) were fixed with ice-cold methanol and blocked with BSA in PBS. The intermediate filaments were stained using indirect immunofluorescence. The primary antibody was a mouse anti-Keratin IgG (Dianova, DLN-09032), and the secondary antibody was a sheep anti-mouse IgG conjugated with ATTO 647N.

Actin Staining

HeLa cells were maintained in DMEM (Gibco) with 10% FBS (Hyclone). Cells were fixed with 100% methanol for 10 min at −20°C, washed twice in PBS. Cells were then incubated with Atto 647N-Phalloidin (ATTO-TEC) for 1h at room temperature, washed five times in PBS, and mounted in mixture of Mowiol 4–88 (Sigma) and DABCO (VWR).

hRSV Probe Delivery

To effectively image the genomic RNA of hRSV in HEp-2 cells, MTRIP probes labeled with DyLight 650 were made in a manner similar to [34]. Briefly, 2′-O-methyl RNA/DNA chimeric oligonucleotides, complimentary to the intergenic sites of the hRSV genomic RNA, with a 5′ biotin modification and 5 primary amine-C_6 deoxy-thymines within the sequence, were labeled with DyLight 650 NHS Ester (Pierce), and filtered using a Zeba spin column (Pierce) to remove free dye. The labeled oligonucleotides were assembled into MTRIP probes and delivered into live cells using streptolysin O (SLO) at 48 h post infection, where they hybridized to multiple sites of the genomic RNA. Pores formed by SLO were closed via recovery in complete growth media for 30 minutes. This was followed by fixation in paraformaldehyde. Cells were mounted in a medium containing 80% glycerol, glucose, glucose oxidase, catalase, and β-mercaptoethanol [35].

Acknowledgments

The authors would like to acknowledge Dr. Katrin Willig, Dr. Benjamine Harke and Dr. Haisen Ta for technical instructions and providing the gold nanoparticle and intermediate filament samples; and Dr. Andreas Schönle for helping with Imspector. PX thank Prof. Stefan W. Hell for mentoring and training on STED nanoscopy instrumentation.

Author Contributions

Conceived and designed the experiments: PX QR DJ JAP. Performed the experiments: YL YD EA WZ. Analyzed the data: YL PX. Contributed reagents/materials/analysis tools: EA PJS WZ JT. Wrote the paper: YL PJS DJ PX.

References

1. Westphal V, Rizzoli SO, Lauterbach MA, Kamin D, Jahn R, et al. (2008) Video-rate far-field optical nanoscopy dissects synaptic vesicle movement. Science 320: 246 249.
2. Willig KI, Rizzoli SO, Westphal V, Jahn R, Hell SW (2006) STED microscopy reveals that synaptotagmin remains clustered after synaptic vesicle exocytosis. Nature 440: 935 939.
3. Hofmann M, Eggeling C, Jakobs S, Hell SW (2005) Breaking the diffraction barrier in fluorescence microscopy at low light intensities by using reversibly photoswitchable proteins. P Natl Acad Sci U S A 102: 17565 17569.
4. Hirvonen LM, Smith TA (2011) Imaging on the Nanoscale: Super-Resolution Fluorescence Microscopy. Aust J Chem 64: 41 45.
5. Cao Y, Gan Z, Jia B, Evans RA, Gu M (2011) High-photosensitive resin for super-resolution direct-laser-writing based on photoinhibited polymerization. Opt Express 19: 19486 19494.
6. Hell SW (2010) Far-field optical nanoscopy. In: Gräslund A, Rigler R, J W, editors. Single Molecule Spectroscopy in Chemistry, Physics and Biology: Springer. 365 398.
7. Hell SW, Wichmann J (1994) Breaking the diffraction resolution limit by stimulated emission: stimulated-emission-depletion fluorescence microscopy. Opt Lett 19: 780 782.
8. Williamson DJ, Owen DM, Rossy J, Magenau A, Wehrmann M, et al. (2011) Pre-existing clusters of the adaptor Lat do not participate in early T cell signaling events. Nat Immunol 12: 655 662.
9. Hanssen E, Carlton P, Deed S, Klonis N, Sedat J, et al. (2010) Whole cell imaging reveals novel modular features of the exomembrane system of the malaria parasite, Plasmodium falciparum. Int J Parasitol 40: 123 134.
10. Riglar DT, Richard D, Wilson DW, Boyle MJ, Dekiwadia C, et al. (2011) Super-resolution dissection of coordinated events during malaria parasite invasion of the human erythrocyte. Cell Host Microbe 9: 9 20.
11. Rust MJ, Bates M, Zhuang X (2006) Sub-diffraction-limit imaging by stochastic optical reconstruction microscopy (STORM). Nat Methods 3: 793 796.
12. Huang B, Wang W, Bates M, Zhuang X (2008) Three-dimensional super-resolution imaging by stochastic optical reconstruction microscopy. Science 319: 810.
13. Shroff H, Galbraith CG, Galbraith JA, Betzig E (2008) Live-cell photoactivated localization microscopy of nanoscale adhesion dynamics. Nat Methods 5: 417 423.
14. Westphal V, Blanca C, Dyba M, Kastrup L, Hell S (2003) Laser-diode-stimulated emission depletion microscopy. Appl Phys Lett 82: 3125.
15. Rankin BR, Hell SW (2009) STED microscopy with a MHz pulsed stimulated-Raman-scattering source. Opt Express 17: 15679 15684.
16. Bückers J, Wildanger D, Vicidomini G, Kastrup L, Hell SW (2011) Simultaneous multi-lifetime multi-color STED imaging for colocalization analyses. Opt Express 19: 3130 3143.
17. Moneron G, Hell SW (2009) Two-photon excitation STED microscopy. Opt Express 17: 14567 14573.
18. Schrof S, Staudt T, Rittweger E, Wittenmayer N, Dresbach T, et al. (2011) STED nanoscopy with mass-produced laser diodes. Opt Express 19: 8066 8072.
19. Wildanger D, Rittweger E, Kastrup L, Hell SW (2008) STED microscopy with a supercontinuum laser source. Opt Express 16: 9614 9621.
20. Scheul T, D'Amico C, Wang I, Vial JC (2011) Two-photon excitation and stimulated emission depletion by a single wavelength. Opt Express 19: 18036 18048.
21. Willig KI, Harke B, Medda R, Hell SW (2007) STED microscopy with continuous wave beams. Nat Methods 4: 915 918.
22. Moneron G, Medda R, Hein B, Giske A, Westphal V, et al. (2010) Fast STED microscopy with continuous wave fiber lasers. Opt Express 18: 1302 1309.
23. Ding JB, Takasaki KT, Sabatini BL (2009) Supraresolution imaging in brain slices using stimulated-emission depletion two-photon laser scanning microscopy. Neuron 63: 429 437.
24. Bianchini P, Harke B, Galiani S, Vicidomini G, Diaspro A (2012) Single-wavelength two-photon excitation-stimulated emission depletion (SW2PE-STED) superresolution imaging. P Natl Acad U S A 109: 6390 6393.
25. So PTC, Dong CY, Masters BR, Berland KM (2000) Two-photon excitation fluorescence microscopy. Annu RevBiomed Eng 2: 399 429.
26. Diaspro A, Chirico G, Collini M (2005) Two-photon fluorescence excitation and related techniques in biological microscopy. Q Rev Biophys 38: 97 166.
27. Xi P, Andegeko Y, Weisel LR, Lozovoy VV, Dantus M (2008) Greater signal, increased depth, and less photobleaching in two-photon microscopy with 10 fs pulses. Opt Commun 281: 1841 1849.
28. Xi P, Andegeko Y, Pestov D, Lovozoy VV, Dantus M (2009) Two-photon imaging using adaptive phase compensated ultrashort laser pulses. J Biomed Opt 14: 014002.
29. Wang W, Liu Y, Xi P, Ren Q (2010) Origin and effect of high-order dispersion in ultrashort pulse multiphoton microscopy in the 10 fs regime. Appl Opt 49: 6703 6709.
30. Keller J, Sch nle A, Hell SW (2007) Efficient fluorescence inhibition patterns for RESOLFT microscopy. Opt Express 15: 3361C3371.
31. Harke B, Keller J, Ullal CK, Westphal V, Schönle A, et al. (2008) Resolution scaling in STED microscopy. Opt Express 16: 4154 4162.
32. Oliva A, Schyns PG (1997) Coarse blobs or fine edges? Evidence that information diagnosticity changes the perception of complex visual stimuli. Cognitive Psychol 34: 72 107.
33. Hyeon C, Dima RI, Thirumalai D (2006) Size, shape, and flexibility of RNA structures. J Chem Phys 125: 194905.
34. Santangelo PJ, Lifland AW, Curt P, Sasaki Y, Bassell GJ, et al. (2009) Single molecule sensitive probes for imaging RNA in live cells. Nat Methods 6: 347 349.
35. Kasper R, Harke B, Forthmann C, Tinnefeld P, Hell SW, et al. (2010) Single-Molecule STED Microscopy with Photostable Organic Fluorophores. Small 6: 1379 1384.
36. Huang B, Jones SA, Brandenburg B, Zhuang X (2008) Whole-cell 3D STORM reveals interactions between cellular structures with nanometer-scale resolution. Nat Methods 5: 1047 1052.
37. Vogelsang J, Kasper R, Steinhauer C, Person B, Heilemann M, et al. (2008) A reducing and oxidizing system minimizes photobleaching and blinking of fluorescent dyes. Angew Chem Int Edit 47: 5465 5469.
38. Wurm CA, Neumann D, Schmidt R, Egner A, Jakobs S (2010) Sample preparation for STED microscopy. In: Papkovsky DB, editor. Live Cell Imaging, Methods in Molecular Biology. Totowa, NJ: Humana Press. 185 199.

2.3 Remarks

The implementation of a Ti:Sapphire oscillator proposed in this chapter opens a new way to realise synchronisation-free CW-STED nanoscopy optimised for different fluorescent dyes at reduced instrumentation complexity and cost. Nevertheless, although ~70 nm resolution was demonstrated using fluorescent nanospheres, we applied over 800 mW output of the 760 nm laser, which is equivalent to over $3.4x10^8$ W/cm^2 depletion intensity at the focus point. Furthermore, at the same intensity level, the resolution decreases to ~100 nm for biological samples due to scattering of the complicated structures and potential mismatch of reflective index. During the experiments, we found that the high depletion intensity can easily destroy fine sub-cellular structures even for fixed cells, rendering live cell imaging practically impossible. This key challenge will be addressed in the next chapters.

Chapter 3

This chapter evaluates the preliminary idea of applying lanthanide-based upconversion nanocrystals in STED microscopy. As concluded from Chapter 2, traditional STED super-resolution imaging requires extreme depletion intensity in order to optically switch (off) conventional fluorescent probes. Theoretically, the depletion power requirement can be reduced by using probes with longer decay lifetime. Therefore, upconversion nanocrystals that emit luminescence with microsecond-to-millisecond lifetime may have the potential to overcome the power barrier. In this chapter, we first introduce the fundamentals and recent progress on upconversion nanocrystals, including a published work of which I was co-author, and then assess the potential application of these nanocrystals for STED operation.

3.1 Upconversion Nanocrystals with Increased Doping

In order to harness the photonic properties of upconversion nanocrystals for potential STED super-resolution imaging, I participated in a project to study upconversion nanocrystals with increased doping concentration at the early stage of my PhD. This provided me an excellent opportunity to learn the fundamental physics of photon upconversion and the systematic approaches to nanoparticle characterisation. We found that highly doped upconversion nanocrystals behave differently compared to conventional upconversion nanocrystals with low doping concentration, which is the key clue for my later projects. This work is reported in the form of a published paper in *Nature Nanotechnology*.

3.1.1 Contributions to Paper 2

TABLE 3-1 Author contributions.

	J.Z.	D.J.	E.P.S.	Y.Lu	Y.Liu	A.V.Z.	Z.L.	J.M.D.	P.X.	J.A.P.	E.M.G.	T.M.M.
Project Design		●										●
Materials	●					●						
System Setup	●	●	●	●								●
Data Collection	●	●	●		●		●					
Analysis	●	●	●		●	●	●	●	●	●	●	●
Manuscript & Figures	●	●	●	●	●			●		●	●	●
Modelling	●										●	
Supplementary Information	●	●				●	●				●	

This project was mainly conducted by my senior peer Jiangbo Zhao under the supervision of Dayong Jin and Tanya Monro. My contribution to this project is centred on the demonstration of security inks using upconversion nanocrystals. In detail, I managed to inject upconversion nanocrystals into the commercial ink cartridges to mix thoroughly with the pigment, and design the security patterns to precisely print them on paper. I laminated the paper samples and mounted them on glass slides, and performed image scanning using the orthogonal scanning automated microscope (OSAM) developed in our group. I analysed the results and prepared the figure illustration.

3.1.2 Paper 2

Zhao J, Jin D, Schartner E P, Lu Y, **Liu Y**, Zvyagin A V, Zhang L, Dawes J M, Xi P, Piper J A, Goldys E G, Monro T M, "Single-nanocrystal sensitivity achieved by enhanced upconversion luminescence". ***Nature Nanotechnology***, 2013, **8**, 794-796.

(First published online: 01 Sep 2013)

nature nanotechnology

LETTERS

PUBLISHED ONLINE: 1 SEPTEMBER 2013 | DOI: 10.1038/NNANO.2013.171

Single-nanocrystal sensitivity achieved by enhanced upconversion luminescence

Jiangbo Zhao[1], Dayong Jin[1]*, Erik P. Schartner[2], Yiqing Lu[1], Yujia Liu[1,3], Andrei V. Zvyagin[1], Lixin Zhang[1], Judith M. Dawes[1], Peng Xi[3,4], James A. Piper[1], Ewa M. Goldys[1] and Tanya M. Monro[2]

Upconversion nanocrystals convert infrared radiation to visible luminescence, and are promising for applications in biodetection[1-3], bioimaging[4-7], solar cells[8-10] and three-dimensional display technologies[8,9,11]. Although the design of suitable nanocrystals has improved the performance of upconversion nanocrystals[10,12-14], their emission brightness is limited by the low doping concentration of activator ions needed to avoid the luminescence quenching that occurs at high concentrations[15,16]. Here, we demonstrate that high excitation irradiance can alleviate concentration quenching in upconversion luminescence when combined with higher activator concentration, which can be increased from 0.5 mol% to 8 mol% Tm^{3+} in $NaYF_4$. This leads to significantly enhanced luminescence signals, by up to a factor of 70. By using such bright nanocrystals, we demonstrate remote tracking of a single nanocrystal with a microstructured optical-fibre dip sensor. This represents a sensitivity improvement of three orders of magnitude over benchmark nanocrystals such as quantum dots[17].

Lanthanide-doped upconversion nanocrystals[8,9] are typically doped with ytterbium (Yb^{3+}) sensitizer ions, which absorb infrared radiation and non-radiatively transfer their excitation to activator ions such as erbium (Er^{3+}), thulium (Tm^{3+}) or holmium (Ho^{3+}). Although recent advances in synthesis have led to accurate control of upconversion nanocrystal morphology, crystal phase and emission colours[7,11,15,16,18–21], it has been difficult to achieve strong upconversion luminescence. Attempts to overcome this problem include coating nanocrystals with an inert/active shell to minimize surface quenching[12,14,22,23], or using noble metal nanostructures to enhance the energy transfer rate by surface plasmons[24,25]. However, these approaches do not address the intrinsic limitation of concentration quenching[15,16,18], where brightness decreases with increasing dopant density beyond the optimal concentration threshold. The optimal Tm^{3+} concentration in $NaYF_4$ host lattices is low, in the range of ~0.2–0.5 mol% at excitation irradiance below 100 W cm^{-2} (with ~20–40 mol% Yb^{3+})[16,26–29]. Such nanocrystals have small numbers of activators and therefore produce weak upconversion emission.

Here we present evidence that upconversion luminescence can be significantly enhanced by using much higher activator concentrations under relatively high-irradiance excitation. We have found that this previously unexplored regime achieves a new balance between the sensitizers, activators and excitation irradiance, and can overcome the widely reported concentration quenching in upconversion[15,16,18,26–29]. As a result, it has been possible to realize high bright upconversion luminescence in 8 mol% Tm^{3+}-doped $NaYF_4$ nanocrystals co-doped with 20 mol% Yb^{3+}. Their high brightness originates from a combination of high excitation intensity, increased activator concentration, and accelerated sensitizer–activator energy transfer rate arising from the decreased average minimum distance between adjacent Ln^{3+} ions. This significantly enhanced upconversion has enabled the remote detection of a single nanocrystal using a fibre dip sensor.

Hexagonal-phase $NaYF_4$ nanocrystals were synthesized with Tm^{3+} concentrations in the range ~0.2–8 mol% co-doped with 20 mol% Yb^{3+} (Supplementary Section S1 and Fig. S1). A single-mode continuous-wave 980 nm diode laser beam launched into a suspended-core microstructured optical fibre (Fig. 1) produced excitation irradiance values of up to 2.5×10^6 W cm^{-2}. The uniform ~40 nm nanocrystals dispersed in cyclohexane (39 pM) were drawn into the holes in the fibre for upconversion luminescence measurements (Supplementary Section S2). This brings the nanocrystals into the vicinity of sufficiently high intensity guided light, and also provides a platform suitable for efficiently collecting their emission. At 2.5×10^6 W cm^{-2} irradiance, we observed that the 8 mol% Tm^{3+} nanocrystals generate a previously unreported bright upconversion emission that is much stronger than in 0.5 mol% Tm^{3+} nanocrystals (the 802 nm emission is increased by a factor of 70, Fig. 1c). In contrast, at a low excitation of 10 W cm^{-2}, our results (Supplementary Fig. S2) show that the upconversion intensity as a function of Tm^{3+} concentration first increases and then decreases above 0.5 mol% Tm^{3+}, consistent with previous reports[16,26–29]. This observation indicates that efficient upconversion emission can be realized at a high activator doping, but only when sufficient irradiance is provided (~1×10^6 W cm^{-2}, achieved in laser scanning microscopy). Sufficient excitation irradiance can unlock otherwise dark activators, thereby enhancing the upconversion brightness (Supplementary Fig S3). This effect is independent of nanocrystal size (from tens to several hundreds of nanometres), surface conditions and synthesis conditions (Supplementary Sections S3, S4, Figs S3–S7).

To understand the relationship between the upconversion signal, activator concentration and excitation irradiance, we collected a matrix of power-dependent (1.6×10^4 W cm^{-2} to 2.5×10^6 W cm^{-2}) luminescence spectra for same sized ~40 nm upconversion nanocrystals at varying Tm^{3+} concentrations. The spectra, which are similar to those in Fig. 2b were decomposed into individual Gaussian peaks (Fig. 2c). These were divided into three groups according to the initial Tm^{3+} levels: the $^3H_4$ group, comprising a single peak at 802 nm, the $^1G_4$ group, with 650 nm and 480 nm peaks, and the $^1D_2$ group, with peaks at 455 nm, 514 nm, 744 nm and 782 nm (see Fig. 2a for a simplified diagram of transitions in the Yb^{3+}–Tm^{3+} system). The integrated intensity ratios of the $^1D_2$

[1]Advanced Cytometry Laboratories, MQ Photonics Research Centre and MQ BioFocus Research Centre, Macquarie University, Sydney, New South Wales 2109, Australia, [2]Institute of Photonics and Advanced Sensing and School of Chemistry and Physics, University of Adelaide, Adelaide, South Australia 5005, Australia, [3]School of Biomedical Engineering, Shanghai Jiao Tong University, Shanghai, China, [4]Department of Biomedical Engineering, College of Engineering, Peking University, Beijing 100871, China. *e-mail: dayong.jin@mq.edu.au

LETTERS NATURE NANOTECHNOLOGY DOI: 10.1038/NNANO.2013.171

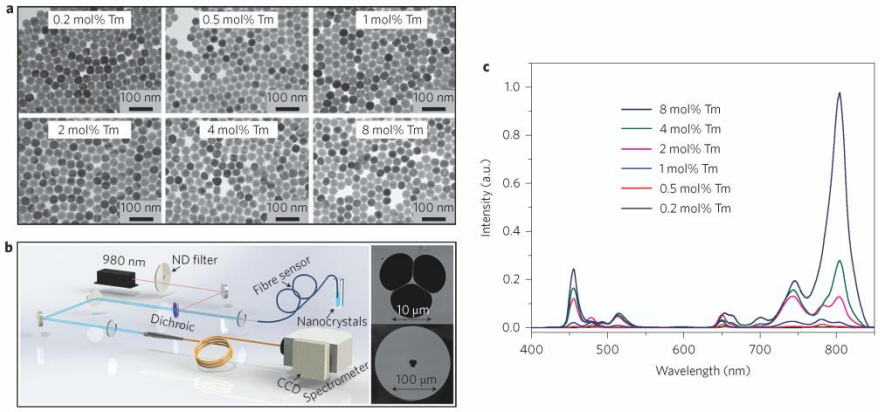

Figure 1 | Highly Tm^{3+}-doped $NaYF_4$ nanocrystals exhibit enhanced upconversion in a suspended-core fibre. a, Transmission electron microscopy images of monodispersed $NaYF_4$:Yb/Tm nanocrystals at different doping levels. All nanoparticles have a similar average size with a narrow size distribution. **b**, Schematic of the experimental configuration for capturing upconversion luminescence of $NaYF_4$:Yb/Tm nanocrystals using a suspended-core microstructured optical-fibre dip sensor. The continuous-wave 980-nm diode laser is targeted at the suspended core. Light propagates along the length of the fibre and interacts with the upconversion nanocrystals located within the surrounding holes. The excited upconversion luminescence is coupled into the fibre core and the backward-propagating light is captured by a spectrometer. Inset: scanning electron microscope images showing a cross-section of the F2 suspended-core microstructured optical fibre at different magnifications. The fibre outer diameter is 160 μm with a 17 μm hole and 1.43 μm core. **c**, Upconversion spectra of a series of $NaYF_4$:Yb/Tm nanocrystals with varied Tm^{3+} concentrations under an excitation irradiance of 2.5×10^6 W cm^{-2}, showing a steady increase in upconversion luminescence with increasing Tm^{3+} content from 0.2 mol% to 8 mol%.

to $^3H_4$ and $^1G_4$ to $^3H_4$ groups (Fig. 2d) show a decreasing contribution of emissions from the $^1G_4$ and $^1D_2$ groups with increasing Tm^{3+} content compared to $^3H_4$ emission. This suggests that the respective population ratios of $^1D_2$ and $^1G_4$ levels to $^3H_4$ decrease in these conditions, to a point where the 8 mol% Tm^{3+} nanocrystals mainly produce the $^3H_4$ (802 nm) emission within our excitation range. We also note that the emission ratios of $^1G_4$:$^3H_4$ and $^1D_2$:$^3H_4$ increase with excitation irradiance in all samples. This suggests that, with increasing excitation irradiance, the population of $^1D_2$ and $^1G_4$ levels increases faster than the population of $^3H_4$. These trends also suggest that a low activator concentration causes an energy transfer bottleneck: at increasing excitation powers the $^3H_4$ level eventually reaches its full capacity to release the 802 nm emission energy (Fig. 2e), and, in order to release any additional energy transferred from Yb^{3+}, the higher energy level emissions in Tm^{3+} ($^1G_4$ and $^1D_2$) become progressively activated. At higher Tm^{3+} concentrations the decay rate of the $^3H_4$ population increases, and this shifts the bottleneck to proportionately higher excitation energies.

Moreover, we have confirmed that the absolute conversion efficiency strongly increases with increasing irradiance, which is attributed to increased excited-state populations of sensitizer and activator ions. The absolute conversion efficiency is defined as the ratio of the emitted to absorbed power (Supplementary Section S5 and Fig. S8)[14]. The absolute conversion efficiency in the low concentration (0.5 mol%) sample reaches a plateau at 3×10^2 W cm^{-2}, whereas in the high concentration (4 mol%) sample it continues to increase within this range. We also measured the power-dependent relative upconversion efficiency for the different nanocrystal samples (Fig. 3a). Increasing the excitation irradiance from 1.6×10^4 W cm^{-2} to 2.5×10^6 W cm^{-2} enhances the overall upconversion luminescence intensity by factors of 5.6, 71 and 1,105 for 0.5 mol%, 4 mol% and 8 mol% Tm^{3+}, respectively. Additionally, this figure indicates that the partitioning of excitation energy flux between the 'effective' 980 nm quanta actually producing upconversion and those 980 nm quanta that are lost on other processes (such as various non-radiative recombination and unobserved emissions) changes dramatically with excitation irradiance and concentration of Tm^{3+} ions. Importantly, at high excitation and high Tm^{3+} doping level, the fraction of excitation energy producing upconversion emission is increased. This shows that upconversion is more efficient at high excitation and for high Tm^{3+} doping. The effect is observed to be especially strong for the 8 mol% Tm^{3+} samples, as is evident from the extremely steep slope above 2×10^6 W cm^{-2} excitation irradiance. Figure 3b shows the same integrated upconversion intensity per Tm^{3+} ion for different Tm^{3+} doping levels. Although the observation of significant enhancement in upconversion intensity from 0.2 mol% to 1 mol% may be due to the fact that upconversion from five photon excitations, previously reported in 0.2 mol% Tm^{3+} (refs 30–32), was not collected in this work, the increase from 1 mol% to 2 mol% clearly shows that the energy transfer efficiency from Yb^{3+} sensitizers to Tm^{3+} activators has been significantly enhanced. This work has therefore shown that the decreased excited sensitizer-to-excited activator distance has indeed increased the energy transfer efficiency, which makes a significant contribution to enhancing the overall conversion efficiency.

To verify that increasing the excitation irradiance enhances the upconversion luminescence and changes the optimal activator/sensitizer concentration ratio, we formulated the rate equations in a generalized upconverting Yb^{3+}–Ln^{3+} system (Supplementary Section S6 and Fig. S9a). In our model the lanthanide ion (activator) is represented by three states—Ln_0, Ln_1 and Ln_2—with equal energy spacing $E_2-E_1 = E_1-E_0$, and the upconversion emission takes place from the excited Ln_2 state to the ground Ln_0 state. The lanthanide ions are excited by energy transfer from the excited states of Yb^{3+} (Yb_1) populated by transitions from the ground-state Yb_0, which have the same energy spacing of E_1-E_0. Using our rate equations,

NATURE NANOTECHNOLOGY DOI: 10.1038/NNANO.2013.171 LETTERS

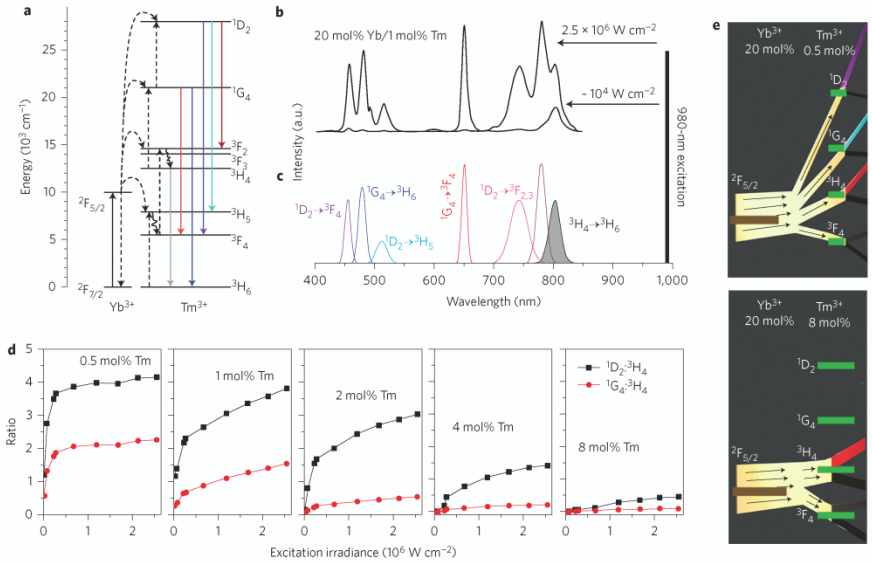

Figure 2 | Analysis of power-dependent multiphoton upconversion. **a**, Simplified energy-level scheme of $NaYF_4$:Yb/Tm nanocrystals indicating major upconversion processes. Dashed lines indicate non-radiative energy transfer, and curved arrows indicate multiphonon relaxation. **b**, Typical evolution of spectra for 1 mol% Tm^{3+} as a function of excitation, showing substantial growth of emissions from the $^1G_4$ and $^1D_2$ levels with increasing excitation from 1×10^4 W cm^{-2} to 2.5×10^6 W cm^{-2}. **c**, Decomposition of the spectra into individual Gaussian peaks. Integrated intensities are given by I_λ where λ is the peak wavelength. Different transitions are indicated by the colours shown in the energy-level scheme in **a**. For example, the shaded area represents the $^3H_4 \rightarrow {}^3H_6$ transitions. **d**, Intensity ratios of the $^1D_2$ to $^3H_4$ classes $(I_{455} + I_{514} + I_{744} + I_{782})/I_{802}$ and $^1G_4$ to $^3H_4$ classes $(I_{480} + I_{660})/I_{802}$ as a function of excitation irradiance. **e**, Diagram illustrating energy transfer between the ensemble of Yb^{3+} and Tm^{3+} ions and subsequent radiative and non-radiative pathways. Top (bottom) panels: low (high) Tm^{3+}/Yb^{3+} ratio. In the case of a low Tm^{3+}/Yb^{3+} ratio, the limited number of Tm^{3+} ions creates an energy transfer bottleneck, due to the limited capacity of Tm^{3+} to release energy from the $^3F_4$ and $^3H_4$ states. Thus, at increasing excitation, alternative energy loss channels (radiative and non-radiative) involving higher states $^1G_4$ and $^1D_2$ progressively switch on. Brown, excitation light; green, simplified energy levels; red, blue and purple, radiative energy flux; grey, radiative flux not observed in this work; black, non-radiative energy loss.

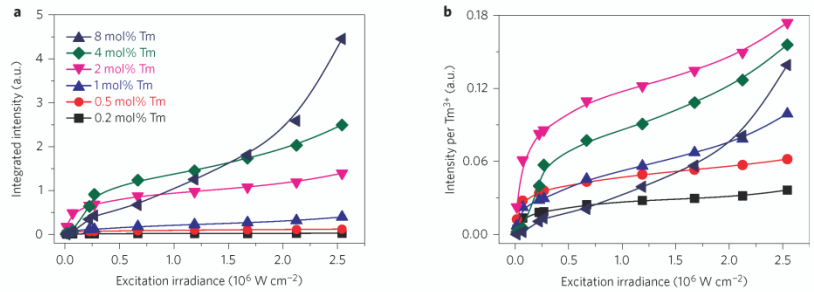

Figure 3 | Analysis of power-dependent upconversion efficiency. **a**, Integrated upconversion luminescence intensity (~400–850 nm) as a function of excitation irradiance for a series of Tm^{3+}-doped nanocrystals. All samples have the same volume and number of nanocrystals. **b**, As in **a**, but divided by the concentration of Tm^{3+} ions. Under an excitation irradiance of 2.5×10^6 W cm^{-2}, 2 mol% Tm^{3+} has the highest relative upconversion efficiency, whereas the strongest upconversion signal is observed in 8 mol% Tm^{3+} due to the larger number of activators available with sufficient excitation.

the population in the Ln_2 state is expressed in terms of the density of lanthanide ions in the ground state, the excited Yb^{3+} population, excitation irradiance and various intrinsic macroscopic rate constants, such as the energy transfer and upconversion rates. The experimental and simulated upconversion luminescence intensities show concentration quenching at low irradiance, but increase at

LETTERS NATURE NANOTECHNOLOGY DOI: 10.1038/NNANO.2013.171

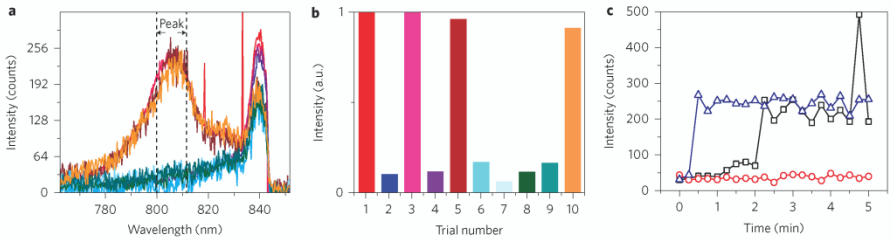

Figure 4 | Detecting a single nanocrystal in a suspended-core microstructured fibre dip sensor. a, Results of 10 trials of loading 3.9 fM nanocrystal solution into the fibre dip sensor. Four positive trials, shown in red, magenta, dark red and orange, show comparable ~800–810 nm emission peaks, and six trials result in consistent background noise baselines (presented in the remaining colours). The baseline level is due to scattering of 980-nm excitation. **b**, Normalized nanocrystal emission integrated from ~800 to 810 nm. The four positive trials shown in red, magenta, dark red and orange produce intensities of ~250 with a low coefficient of variation (CV) of 4.7%, and high signal-to-noise ratio of >8. **c**, Time-dependent dynamics of three independent trials. Red: trial with no nanocrystals observed (only background is observed). Blue: one nanocrystal appears shortly after the start of the trial. Black: single nanocrystal appears in the fibre after 2 min, followed by a second at ~5 min; one of the nanocrystals then exits the observation volume.

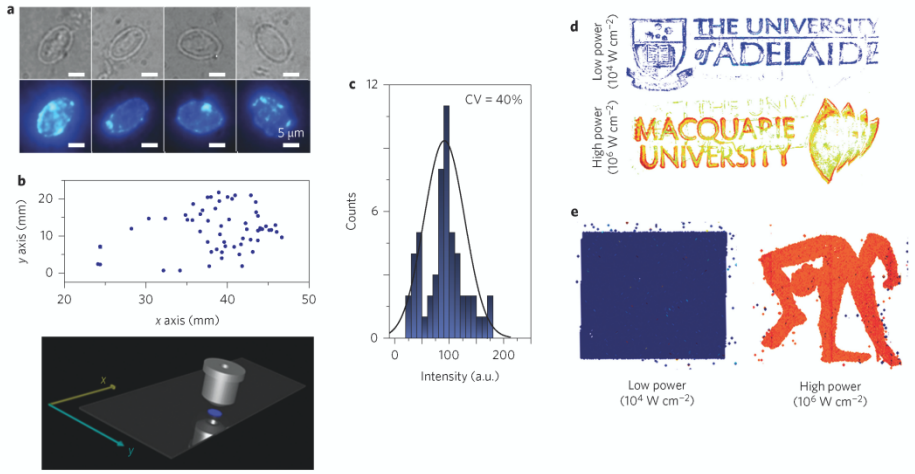

Figure 5 | Proof-of-principle experiments demonstrating a broad spectrum of applications. a, Images of *Giardia lamblia* cells labelled with antibody-conjugated 4 mol% Tm^{3+} upconversion nanocrystals under transmission (top) and luminescence (bottom) modes. The 980-nm wide-field excitation and upconversion detection yield negligible autofluorescence background, so absolute signal intensities of each single microorganism (see histogram in **c**) provide quantification of the level of surface antigens. **b**, Individual cells localized on a glass slide by a scanning cytometry system (top), and its schematic (bottom). Targeted cells are symbolized by blue dots. **c**, Histogram showing the quantification results of the population of nanocrystal-labelled *Giarida lamblia* (CV, coefficient of variation). **d**, Demonstrations of security inks using the power-dependent optimal Tm^{3+} concentration. Low-concentration (0.2 mol% Tm^{3+}) nanocrystals were used to stain the masking pattern (University of Adelaide logo), which is visible under both low-power illumination (top) and high-power illumination (bottom). High-concentration (4 mol% Tm^{3+}) nanocrystals were used to stain the hidden pattern (Macquarie University logo), which is over 10 times brighter than the masking pattern. At this dynamic range the masking pattern is almost unnoticeable. **e**, Nanocrystal solution 'security inks' were used in an inkjet printer with 0.5 mol% Tm^{3+} nanocrystals as a rectangular mask to confound the signal image from 8 mol% Tm^{3+} nanocrystals. At laser scanning confocal setting (>1 × 10^6 W cm^{-2}), the hidden trademark image of the 8 mol% Tm^{3+} nanocrystals becomes visible and dominant.

high irradiance, in agreement with our observations (Supplementary Fig. S9b–f). Moreover, the simulations show increasing relative upconversion efficiency with increasing excitation irradiance (Supplementary Fig. S9g), which is in agreement with Fig. 3a. To the best of our knowledge, this is the first analytical approach to describe the upconversion quenching process at increasing activator concentrations and excitation powers.

We have demonstrated that these bright nanocrystals can significantly extend the detection limit in a fibre-based dip sensor, a novel nanoscale sensing platform for clinical point-of-care, chemical and

NATURE NANOTECHNOLOGY DOI: 10.1038/NNANO.2013.171 LETTERS

biological applications[17]. The detection limit for fluorescent quantum dots in such sensors was earlier reported to be ~10 pM due to competing autofluorescence background from the fibre itself. In this work the fibre autofluorescence problem is avoided by using 980 nm excitation and 802 nm emission of Tm^{3+}, wavelengths that are well separated from the glass background fluorescence (Supplementary Fig. S11). To investigate the achievable detection limit, we measured our brightest 8 mol% Tm^{3+} nanocrystals at 3.9 fM dilution in ten identical fibre dip sensors (Supplementary Section S8). The respective 802 nm peaks (Fig. 4a) show a consistent intensity of 250 ± 30 counts in four experiments, whereas six other experiments show a consistent background level of ~30 counts (Fig. 4b). We attribute these strongly quantized values of the peak intensity (~220 net counts) to the observation of single nanocrystals in these four trials. To confirm this hypothesis we calculated the average number of particles expected to be located within the detection volume in a microstructured fibre, and found this to be 0.55, consistent with our observations of a single nanocrystal in 40% of trials. The Poissonian probability of observing two or more nanocrystals in a single trial for our average of 0.55 particles is 11%. To validate our assignment further, we set up an experiment to continuously monitor the 802 nm upconversion intensity during sample intake as the holes of the fibre fill with the nanocrystal suspension by capillary action (Fig. 4c). One of these trials (red) showed the background signal only, indicating that in this trial no nanocrystals entered the detection volume. The second (blue) showed a single nanocrystal appearing in the detection volume halfway through the experiment. The third (black) showed one nanocrystal entering the detection region, followed by a second one after 6 min; one nanocrystal is then observed to exit while the other continues to be observed. The signal of both combined nanocrystals is 470 ± 30 (440 net counts), twice the single nanocrystal net count of 220. These experiments show that high brightness of upconversion emission achieved at sufficient irradiance excitation enables, for the first time, the detection of a single high Tm^{3+}-doped nanocrystal within the fibre platform. Furthermore, these single nanocrystals are bright enough to be visible to the naked eye and could be recorded by a low-cost digital camera in a wide-field microscopy system (Fig. S10 in Supplementary Section S7).

This exceptional nanocrystal brightness provides compelling advantages to a wide range of fields including immunofluorescence imaging (Fig. 5a), rare event cell detection and quantification (Fig. 5b,c), document security (Fig. 5d) and security printing (Fig. 5e). We demonstrated that the new ultrabright upconversion nanocrystals provide high-contrast biolabels. To this end, *Giardia lamblia* cells were labelled by nanocrystals conjugated to suitable monoclonal antibodies (G203). Figure 5a shows the labelled Giardia cells imaged by a scanning system at only 0.1 s exposure time by a standard charge-coupled device (CCD) camera. The absence of autofluorescence background at 980 nm excitation enabled the quantification of the absolute signal intensities of each single microorganism, as well as quantification of the level of surface antigens (Fig. 5c)[33]. Single labelled cells on a glass slide have been detected within 3 min without background interference (Fig. 5b). This shows that these bioprobes are capable of rare event detection. Moreover, excitation-dependent upconversion has also enabled a new approach to 'security inks' (Fig. 5d,e), because the highly doped (>4 mol%) Tm^{3+} nanocrystals remain dark unless high infrared excitation irradiance is used, in contrast to low doped nanocrystals (Fig. 5d). Additionally, the nanocrystal suspensions can be dispersed in traditional inkjet printer inks to print highly secure trademarks/images on papers/plastics (Fig. 5e).

In conclusion, we have demonstrated a novel approach to significantly enhance the upconversion luminescence of nanocrystals, by increasing the activator concentration in combination with elevated irradiance excitation ($\sim 1 \times 10^6$ W cm^{-2}). The microstructured fibre dip sensor used here easily achieves such excitation intensities, making it possible to detect single nanocrystals while probing subcellular fluid volumes. These results show that the nanocrystals can be detected at one end of the fibre as they enter the fibre from the other end, enabling measurements to be made from a significant distance, and leading the way to *in vivo* measurements. Highly Ln^{3+}-doped nanocrystals at sufficient irradiance excitation have strong potential for use as photostable, background-free and extremely bright labelling probes for bioimaging. Furthermore, this work presents a new approach for understanding and predicting the behaviour of lanthanide-based upconversion systems, and provides new directions both for nanoscale sensing and the materials science of Ln^{3+}-doped nanomaterials.

Received 13 May 2013; accepted 26 July 2013;
published online 1 September 2013

References

1. Zhang, C., Yuan, Y., Zhang, S., Wang, Y. & Liu, Z. Biosensing platform based on fluorescence resonance energy transfer from upconverting nanocrystals to graphene oxide. *Angew. Chem. Int. Ed.* **50,** 6851–6854 (2011).
2. Wu, S. W. *et al.* Non-blinking and photostable upconverted luminescence from single lanthanide-doped nanocrystals. *Proc. Natl Acad. Sci. USA* **106,** 10917–10921 (2009).
3. Stepuk, A. *et al.* Use of NIR light and upconversion phosphors in light-curable polymers. *Dental Mater.* **28,** 304–311 (2012).
4. Nyk, M., Kumar, R., Ohulchanskyy, T. Y., Bergey, E. J. & Prasad, P. N. High contrast *in vitro* and *in vivo* photoluminescence bioimaging using near infrared to near infrared up-conversion in Tm^{3+} and Yb^{3+} doped fluoride nanophosphors. *Nano Lett.* **8,** 3834–3838 (2008).
5. Wang, M. *et al.* Immunolabeling and NIR-excited fluorescent imaging of HeLa cells by using $NaYF_4$:Yb,Er upconversion nanoparticles. *ACS Nano* **3,** 1580–1586 (2009).
6. Yang, Y. M. *et al. In vitro* and *in vivo* uncaging and bioluminescence imaging by using photocaged upconversion nanoparticles. *Angew. Chem. Int. Ed.* **51,** 3125–3129 (2012).
7. Tian, G. *et al.* Mn^{2+} dopant-controlled synthesis of $NaYF_4$:Yb/Er upconversion nanoparticles for *in vivo* imaging and drug delivery. *Adv. Mater.* **24,** 1226–1231 (2012).
8. Haase, M. & Schäfer, H. Upconverting nanoparticles. *Angew. Chem. Int. Ed.* **50,** 5808–5829 (2011).
9. Auzel, F. Upconversion and anti-Stokes processes with *f* and *d* ions in solids. *Chem. Rev.* **104,** 139–173 (2004).
10. Zou, W. Q., Visser, C., Maduro, J. A., Pshenichnikov, M. S. & Hummelen, J. C. Broadband dye-sensitized upconversion of near-infrared light. *Nature Photon.* **6,** 560–564 (2012).
11. Wang, F. *et al.* Simultaneous phase and size control of upconversion nanocrystals through lanthanide doping. *Nature* **463,** 1061–1065 (2010).
12. Vetrone, F., Naccache, R., Mahalingam, V., Morgan, C. G. & Capobianco, J. A. The active-core/active-shell approach: a strategy to enhance the upconversion luminescence in lanthanide-doped nanoparticles. *Adv. Funct. Mater.* **19,** 2924–2929 (2009).
13. Liu, X. *et al.* Breakthrough in concentration quenching threshold of upconversion luminescence via spatial separation of the emitter doping area for bio-applications. *Chem. Commun.* **47,** 11957–11959 (2011).
14. Boyer, J. C. & van Veggel, F. C. Absolute quantum yield measurements of colloidal $NaYF_4$: Er^{3+}, Yb^{3+} upconverting nanoparticles. *Nanoscale* **2,** 1417–1419 (2010).
15. Wang, F. & Liu, X. Upconversion multicolor fine-tuning: visible to near-infrared emission from lanthanide-doped $NaYF_4$ nanoparticles. *J. Am. Chem. Soc.* **130,** 5642–5643 (2008).
16. Zhang, H., Li, Y., Lin, Y., Huang, Y. & Duan, X. Composition tuning the upconversion emission in $NaYF_4$:Yb/Tm hexaplate nanocrystals. *Nanoscale* **3,** 963–966 (2011).
17. Schartner, E. P., Ebendorff-Heidepriem, H., Warren-Smith, S. C., White, R. T. & Monro, T. M. Driving down the detection limit in microstructured fiber-based chemical dip sensors. *Sensors* **11,** 2961–2971 (2011).
18. Wang, F. *et al.* Tuning upconversion through energy migration in core–shell nanoparticles. *Nature Mater.* **10,** 968–973 (2011).
19. Ye, X. C. *et al.* Morphologically controlled synthesis of colloidal upconversion nanophosphors and their shape-directed self-assembly. *Proc. Natl Acad. Sci. USA* **107,** 22430–22435 (2010).
20. Yan, C., Dadvand, A., Rosei, F. & Perepichka, D. F. Near-IR photoresponse in new up-converting CdSe/$NaYF_4$:Yb,Er nanoheterostructures. *J. Am. Chem. Soc.* **132,** 8868–8869 (2010).

21. Gorris, H. H., Ali, R., Saleh, S. M. & Wolfbeis, O. S. Tuning the dual emission of photon-upconverting nanoparticles for ratiometric multiplexed encoding. *Adv. Mater.* **23,** 1652–1655 (2011).
22. Wang, F., Wang, J. A. & Liu, X. G. Direct evidence of a surface quenching effect on size-dependent luminescence of upconversion nanoparticles. *Angew. Chem. Int. Ed.* **49,** 7456–7460 (2010).
23. Mai, H. X., Zhang, Y. W., Sun, L. D. & Yan, C. H. Highly efficient multicolor up-conversion emissions and their mechanisms of monodisperse $NaYF_4$:Yb,Er core and core/shell-structured nanocrystals. *J. Phys. Chem. C* **111,** 13721–13729 (2007).
24. Priyam, A., Idris, N. M. & Zhang, Y. Gold nanoshell coated $NaYF_4$ nanoparticles for simultaneously enhanced upconversion fluorescence and darkfield imaging. *J. Mater. Chem.* **22,** 960–965 (2012).
25. Zhang, F. *et al.* Fabrication of $Ag@SiO_2@Y_2O_3$:Er nanostructures for bioimaging: tuning of the upconversion fluorescence with silver nanoparticles. *J. Am. Chem. Soc.* **132,** 2850–2851 (2010).
26. Yin, A., Zhang, Y., Sun, L. & Yan, C. Colloidal synthesis and blue based multicolor upconversion emissions of size and composition controlled monodisperse hexagonal $NaYF_4$:Yb,Tm nanocrystals. *Nanoscale* **2,** 953–959 (2010).
27. Mahalingam, V., Vetrone, F., Naccache, R., Speghini, A. & Capobianco, J. A. Colloidal Tm^{3+}/Yb^{3+}-doped $LiYF_4$ nanocrystals: multiple luminescence spanning the UV to NIR regions via low-energy excitation. *Adv. Mater.* **21,** 4025–4028 (2009).
28. Kramer, K. W. *et al.* Hexagonal sodium yttrium fluoride based green and blue emitting upconversion phosphors. *Chem. Mater.* **16,** 1244–1251 (2004).
29. Liang, L. F., Wu, H., Hu, H. L., Wu, M. M. & Su, Q. Enhanced blue and green upconversion in hydrothermally synthesized hexagonal $NaY_{1-x}Yb_xF_4:Ln^{3+}$. *J. Alloys Comp.* **368,** 94–100 (2004).
30. Chen, X. & Song, Z. Study on six-photon and five-photon ultraviolet upconversion luminescence. *J. Opt. Soc. Am. B* **24,** 965–971 (2007).
31. Chen, G. Y., Somesfalean, G., Zhang, Z. G., Sun, Q. & Wang, F. P. Ultraviolet upconversion fluorescence in rare-earth-ion-doped Y_2O_3 induced by infrared diode laser excitation. *Opt. Lett.* **32,** 87–89 (2007).
32. Qin, G. S. *et al.* Intense ultraviolet upconversion luminescence from Yb^{3+} and Tm^{3+} codoped amorphous fluoride particles synthesized by pulsed laser ablation. *Opt. Commun.* **242,** 215–219 (2004).
33. Lu, Y., Xi, P., Piper, J. A., Huo, Y. & Jin, D. Time-gated orthogonal scanning automated microscopy (OSAM) for high-speed cell detection and analysis. *Sci. Rep.* **2,** 837 (2012).

Acknowledgements

The authors thank D. Birch, D. Inglis, N. Vella, A. Nadort, R. Field, M. Nguyen, D. Liu, C. Yan and J. Shen (Olympus Australia) for sample characterization, H. Ebendorff-Heidepriem for providing the suspended-core fibres, which were fabricated at the OptoFab node of the Australian National Fabrication Facility (ANFF), and A. Nechaev (Lomonosov Moscow State University of Fine Chemical Technologies, Russia) for bulk crystal preparation. J.Z. acknowledges a Macquarie University Research Excellence Scholarship, and D.J. and J.P. acknowledge support from the Australian Research Council (DP1095465, LP130100517). P.X. acknowledges support from the '973 program' of China (2011CB707502, 2011CB809101) and T.M. acknowledges the support of an ARC Federation Fellowship.

Author contributions

D.J. and T.M. conceived the project, designed the experiments and supervised the research. J.Z., E.S., Y.Lu and D.J. were primarily responsible for data collection and analysis. D.J., E.G., J.Z. and T.M. prepared figures and wrote the main manuscript text. J.Z., E.G., A.Z. and D.J. were primarily responsible for supporting information and numerical simulations. All authors contributed to data analysis, discussions and manuscript preparation.

Additional information

Supplementary information is available in the online version of the paper. Reprints and permissions information is available online at www.nature.com/reprints. Correspondence and requests for materials should be addressed to D.J.

Competing financial interests

The authors declare no competing financial interests.

3.2 Stimulated emission depletion using upconversion nanocrystals

My involvement in Paper 2 as well as the $NaYF_4$:Yb^{3+}/Tm^{3+} upconversion nanocrystal samples used there offered me a good foundation to investigate their potential for stimulated emission depletion. I then designed and conducted some preliminary experiments to validate this idea.

3.2.1 Design of upconversion STED

As shown in Fig 3-1, when the $NaYF_4$:Yb^{3+}/Tm^{3+} nanocrystals are excited at 980 nm, the Yb^{3+} sensitiser ions absorb the excitation photons, and then transmit the energy to Tm^{3+} emitter ions. As a result of the ladder-like energy levels, the Tm^{3+} are capable of being pumped onto multiple intermediate excited states, which then emit upconversion luminescence at multiple wavelengths through spontaneous emission. These include 2.0 um IR emission from the $^3F_4$ level to the ground level; 793 nm NIR emission from the $^3H_4$ level to the ground level; 475 nm and 660 nm visible emission from the $^1G_4$ level to the $^3H_6$ level and the $^3F_4$ level, respectively; 360 nm, 455nm and 743 nm from the $^1D_2$ level to the ground level, the $^3F_4$ level and the $^3H_4$ level, respectively. Photon upconversion progress to higher excited levels is also possible, but their emission are mainly in UV range, which are less attractive in the majority of biological studies.

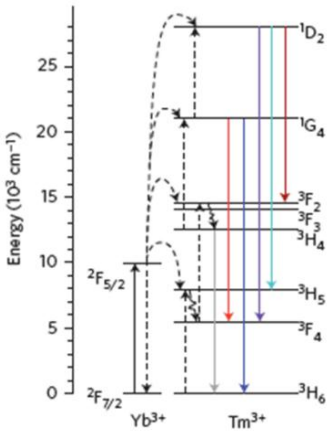

FIGURE 3-1 Jablonski diagram of Tm^{3+}-doped rare-earth upconversion material $NaYF_4$:Yb^{3+}/Tm^{3+}

Since the emitters are pumped onto lower excited levels first before being pumped further onto the higher excited levels, if the accumulation of emitters on any intermediate level is inhibited, the upconversion luminescence resulting from higher levels will be hindered. Therefore, a new STED scheme can be designed for upconversion nanocrystals, which depletes one of the intermediate energy level via stimulated emission to switch off the luminescence signal. For the Yb^{3+}/Tm^{3+} co-doped system here, for example, an 808 nm depletion beam can be added to deplete the $^3H_4$ level down to the ground level, so that the upconversion process to $^1G_4$ and $^1D_2$ will be interrupted, as shown in Fig 3-2. This is different from traditional STED, where depletion and emission are essentially from the same excited energy level.

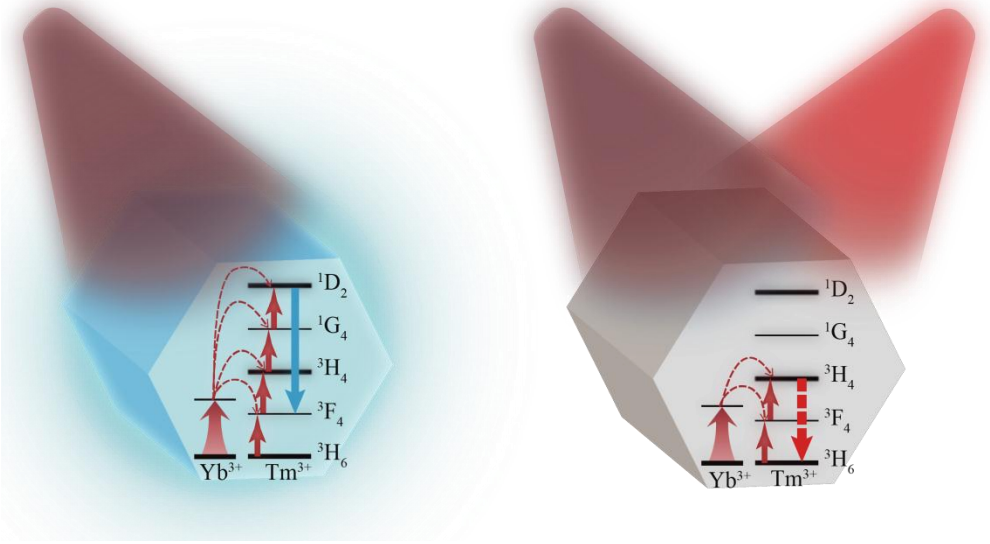

FIGURE 3-2 Mechanism of intermediate-state ladder depletion in $NaYF_4:Yb^{3+}/Tm^{3+}$ upconversion nanomaterial

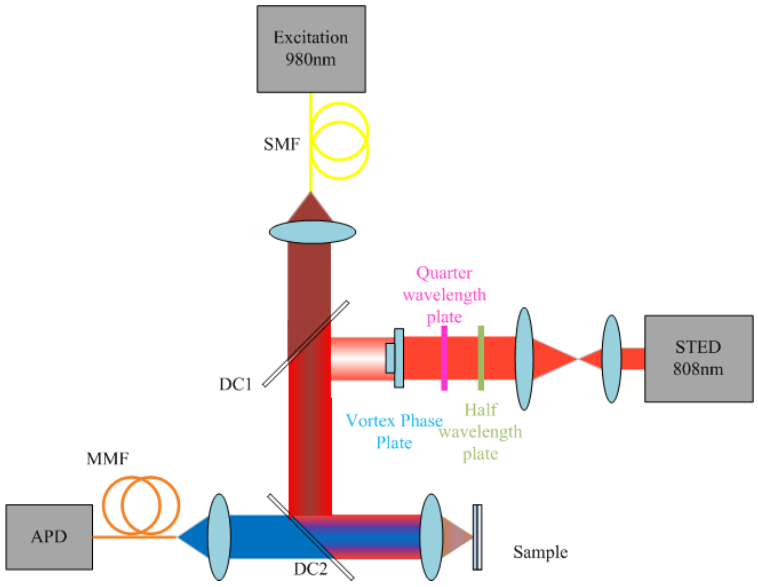

FIGURE 3-3 The optical layout of the dual-laser confocal microscope for probing upconversion nanocrystals. To further realize optical super-resolution, a half-wave plate, a quarter-wave plate and a vortex phase plate are inserted in the 808 nm beam path. MMF: single-mode fibre; MMF: multi-mode fibre; DC1 and DC2: dichotic filters

Based on the new depletion scheme, I built the upconversion STED super-resolution microscopy system for Tm^{3+} doped nanocrystals. As shown in Fig 3-3, sample scanning configuration was employed using a 3-axis closed-loop piezo stage (stage body MAX311D/M, piezo controller BPC303; Thorlabs). A single-mode fibre-coupled 980 nm diode laser (LE-LS-980-300-FCS, LEO Photonics; maximum output power 300 mW) was used as the excitation source. After collimation, the excitation beam transmitted through a long-pass dichroic mirror (ZT860lpxr, Chroma; cutting edge at 860 nm), then was reflected by a second short-pass dichroic mirror (T750spxrxt, Chroma), and focused through an oil-immersion objective (UPlanAPO, Olympus; 100X, NA = 1.4) onto the sample slide. The first dichroic mirror also allowed the 808 nm probing beam from a polarization-maintaining fibre-coupled diode laser (LU0808M250-1C16F30A, Lumics; single mode, linear polarisation, maximum output power 250 mW) to merge with the 980 nm beam. Diligent alignment was performed to ensure the two laser beams precisely overlap on the focal plane of the objective. The lateral FWHM of PSF (Point of Spread Function) was measured to be ~420 nm.

The luminescence signal from the sample was collected by the same objective, split from the excitation and probing beams by the second dichroic mirror, before coupled into a

multi-mode fibre (M24L01, Thorlabs). The other end of the fibre was connected to a single-photon avalanche diode (SPAD; SPCM-AQRH-13-FC, PerkinElmer). To select the emission bands, different band-pass filters (FF01-448/20-25 and FF01-660/13-25, Semrock) were inserted in the detection path for both transient response measurement and confocal imaging.

For measuring the 800 nm transient response under 980 excitation only, the distal end of the multi-mode fibre connected to the SPAD can be substituted for the distal end of the polarisation-maintaining fibre of the 808 nm laser, with a band-pass filter (FB800-10, Thorlabs) also inserted in the beam path.

3.2.2 Sample preparation

The $NaYF_4$:Yb^{3+}/Tm^{3+} nanocrystals, which were the same as used in paper 2, were synthesized using the co-deposition method. Briefly, 5 mL of methanol solution of $LnCl_3$ (1.0 mmol, Ln = Y, Yb, Tm/Er) was magnetically mixed with 6 mL OA and 15 mL ODE in a three-neck round-bottom flask. The resulting mixture was heated at 150 ℃ under argon flow for 30 min to form a clear light yellow solution. After cooling down to 50 ℃, 10 mL of methanol solution containing 0.16 g NH_4F and 0.10 g NaOH was added with vigorous stirring for 30 min. Then, the slurry was slowly heated and kept at 110 ℃ for 30 min to remove methanol and residual water. Next, the reaction mixture was protected with an argon atmosphere, quickly heated to 305 ℃ and maintained for 1.5 h. The products were isolated by adding ethanol, and centrifuged without size-selective fractionation. The final $NaYF_4$:Yb/Tm nanocrystals were redispersed in cyclohexane with 5 mg/mL concentration after washing with cyclohexane/ethanol several times.

The sensitizer Yb^{3+} concentration is fixed at 20% for all samples, and the emitter Tm^{3+} concentrations are 0.5%, 2%, 2.5%, 3%, 3.5%, 4%, 6% and 8% respectively. The transmission electron microscopy (TEM) images of the samples are shown in Fig 3-4.

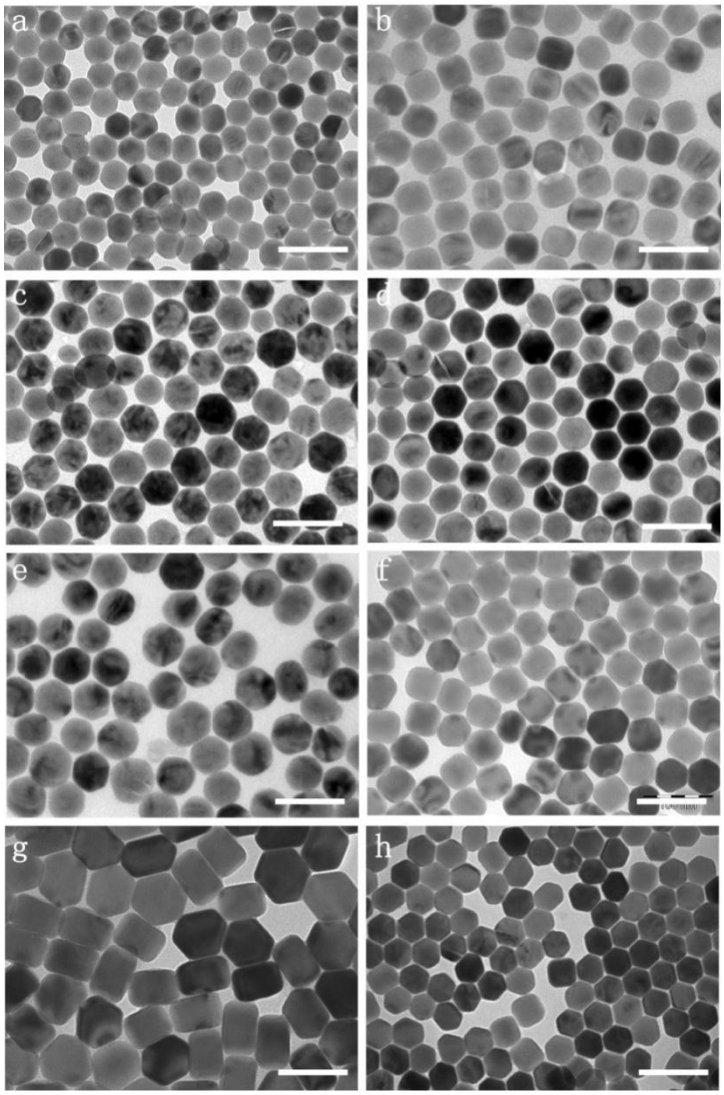

FIGURE 3-4 TEM results of eight β-phase $NaYF_4$:Yb^{3+}/Tm^{3+} upconversion nanocrystals used in this chapter. The Yb^{3+} dopant concentration is fixed to 20% and the Tm^{3+} dopant concentration from (a) to (i) is 0.5%, 2%, 2.5%, 3%, 3.5%, 4%, 6% and 8%, respectively. Scale bar: 100 nm

For super-resolution imaging, the use of immersion lenses with high numerical apertures is compromised by spherical aberrations induced by the refractive index mismatch between the immersion and the embedding medium. A solution to this problem is to adapt the index of the embedding medium to that of the immersion medium. This is crucial for high-resolution imaging. For the lanthanide-doped upconversion nanocrystals, the embedding medium Mowiol used in Chapter 2 is also suitable due to its none interactive characteristics. The preparation protocol for Mowiol mixture is as follows:

1. Mix 6 g glycerol with 2.4 g Mowiol 4-88 in a 50 ml centrifuge tube and stir 1 h on magnetic stirrer.

2. Add 6 ml water and stir for further 2 h.

3. Add 12 ml Tris–HCl buffer (0.2 M, pH 8.4) and heat up the solution to 50 ℃ (in a water-bath) for more than 2 h under constant agitation. Extend this step, until the Mowiol 4-88 is completely dissolved.

4. Centrifuge at 7500g for 30 min to remove any undissolved solids.

5. Aliquot in eppendorf tubes and store at –20 ℃. Each aliquot can be used for several weeks if stored at 4 ℃.

Notably, the standard protocol of embedding normal organic samples in Mowiol for STED imaging does not work well with upconversion nanocrystals, as they tend to aggregate substantially in the final sample slide, even with properly diluted concentration. Further dilution will largely reduce the number of nanocrystals in field of view, which will adversely affect the measurement. This is a new challenge not reported in literature, as previous works on upconversion nanocrystals are mainly based on dense samples for measurement; whereas here samples with individually distributed nanocrystals are essential for quality evaluation of super-resolution imaging.

To prevent upconversion nanocrystals from aggregation, we developed a new protocol for preparing the sample slides, which presents the highest success rate for achieving individually distributed upconversion nanocrystals. The new protocol is as follows:

1. Dilute the concentration of the upconversion nanocrystals solution to 0.08 mg/ml.

2. Wash the cover slips with pure ethanol then H_2O under ultrasonication, then treat with 50 ul Poly-L-lysine solution (0.1% w/v in H_2O) on the front surface of the cleaned cover-glass

3. After 30 mins wash off the Poly-L-Lysine with H_2O, then dry the surface of the cover slips (heat or air dry)

4. Drop 20ul upconversion nanocrystals solution on the treated surface, wait for 2 seconds then wash the solution off with 100 ul cyclohexane twice.

5. After air-dried, the cover slip was put over a clean slide containing 20 μl as-prepared embedding medium, with any air bubbles squeezed out by gentle force. The sample was kept at room temperature for another 24 h to ensure complete drying before being tested.

Fig. 3-5 presents the confocal imaging results of sample slides prepared using the standard protocol (Fig. 3-5a) and the new protocol (Fig. 3-5b), respectively, which clearly shows superior performance of the latter.

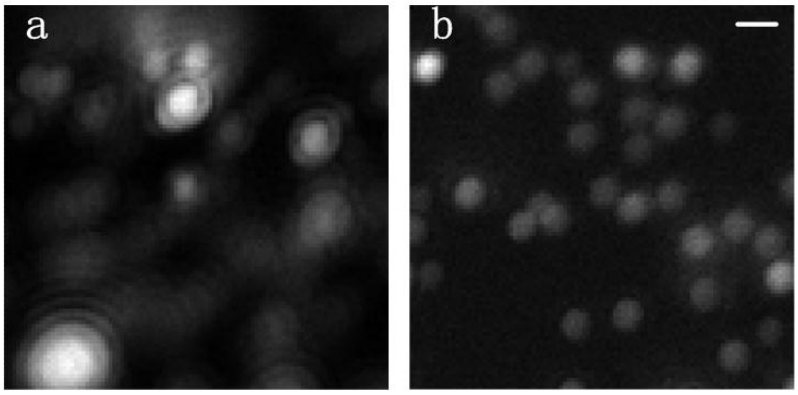

FIGURE 3-5 Comparison of confocal fluorescent results on single nanoparticles samples prepared by different protocols. (a)Separation results only by dilution; (b)The sample prepared with the protocol presented in this section. Yb^{3+} dopant concentration is 20%, and Tm^{3+} is 4%. Fluorescent wavelength: 455 nm, scale bar: 1 μm

We also developed a robust protocol to prepare dense but single-layer upconversion nanocrystals on glass slides, to avoid potential inaccuracy in the luminescence signal as the excitation intensity changes along the axial axis, for measurements that do not need to be performed on single particles. The protocol is as follows:

1. Dilute the concentration of the upconversion nanocrystals solution to 8 mg/ml.

2. Wash the cover slips with pure ethanol then H_2O under ultrasonication, then treat with 50 ul Poly-L-lysine solution (0.1% w/v in H_2O) on the front surface of the cleaned cover-glass

3. After 30 mins wash off the Poly-L-Lysine with H_2O, then dry the surface of the cover slips (heat or air dry)

4. Drop 20 ul upconversion nanocrystals solution on the treated surface. After air-dried, the cover slip was put over a clean slide containing 20 μl as-prepared embedding medium,

with any air bubbles squeezed out by gentle force. The sample was kept at room temperature for another 24 h to ensure complete drying before being tested.

3.2.3 Initial Depletion Test on $NaYF_4:Yb^{3+}/Tm^{3+}$ nanocrystals

The samples prepared above were measured by the dual-laser confocal setup to test the depletion efficiency of Tm^{3+}-doped upconversion nanocrystals. The preliminary results were highly encouraging. While the upconversion nanocrystal with conventional doping concentration of 0.5% was difficult to switch off (they are less efficient than the best-performing dye, Dylight 650, depleted at 783 nm in our previous CW STED system), the nanocrystals with high doping concentrations, e.g. those with 6% Tm^{3+}, are surprisingly efficient to deplete, as shown in Fig 3-6. In fact, they were almost completely depleted at low depletion power on the sub-milliwatt level.

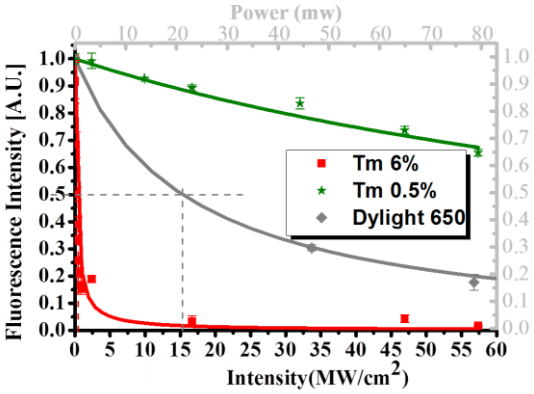

FIGURE 3-6 The modulation efficiency versus the depletion intensity. measured with $NaYF_4:Yb^{3+}/Tm^{3+}$ nanocrystals. The red spots indicate the depletion data on high dopant nanocrystals of 6% Tm^{3+}. The red curve is the fitting curve. The green spots indicate the depletion data on low dopant nanocrystals of 0.5% Tm^{3+}. The green curve is the fitting curve. Excitation wavelength is 980 nm and depletion wavelength is 808 nm. Fluorescent central wavelength is 455 nm. Grey spot and dash curve indicates the depletion data and fitting curve of Dylight 650 which shows the lowest I_s in chapter 2, respectively.

3.2.4 Influence of temporal configuration

To study the affection of temporal factors in two wavelength modulation on Tm^{3+} dopant upconversion nanocrystals, we monitored the time dependant fluorescent emission

with 980 nm laser and 808 nm laser both in pulse mode. The lasers were set to be the same in pulse duration time while different pulse delay interval.

The controlled measurement was carried on high dopant $NaYF_4:Yb^{3+}/Tm^{3+}$ upconversion nanocrystals with 8% Tm^{3+} and 20% Yb^{3+} dopant concentration. In some other projects, we have measured the dopant dependant fluorescent lifetime on $NaYF_4:Yb^{3+}/Tm^{3+}$ upconversion nanocrystals. And for the 8% dopant concentration sample, the lifetime is on 10^1-10^2 micro-second level. To ensure the sufficient population reversion, we applied 1 milli-second pulse duration condition in our measurement. And the temporal interval between 808 nm and 980 nm pulses started at 808 nm pulses coming 1 ms ahead of 980 nm with step of 0.5 ms, until 808 nm pulses were completely after 980 nm pulses. The measurement cycle was set to be 10 ms. The intensity of 980 nm and 808 nm was 0.6 MW/cm^2 and 0.76 MW/cm^2, respectively.

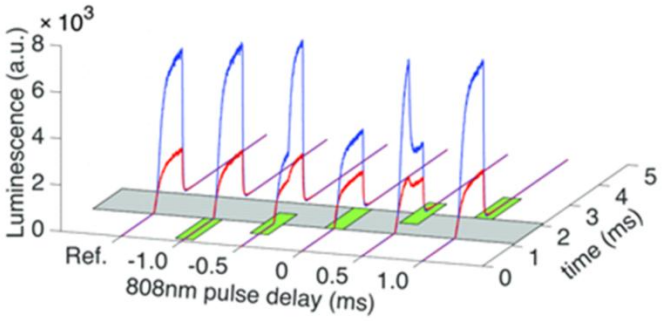

FIGURE 3-7 Transient responses of upconversion emission at 455 nm (blue curves) and 660 nm(red curves) from 8% Tm^{3+}-doped nanocrystals under pulsed 980 nm (grey shadows) and 808 nm (green shadows) illumination (Ref. curve is measured without 808 nm illumination). The 980 nm excitation intensity is 0.6 MW/cm^2 and the 808 nm probing intensity is 0.76 MW/cm^2. Pulse duration time is 1 ms and measurement period is 10 ms

As shown in Fig 3-7, from the response emission curve of 455 nm(blue) and 660 nm(red), it is clear that without any overlapping in temporal domain, there would be no depletion on upconversion fluorescent emission. While with half or complete overlapping on temporal domain, the fluorescent emission could be depleted well in the overlapped time frame. And with totally overlapping, the 808 nm showed the highest depletion efficiency.

Interestingly, when 808 nm pulses lead 1 ms ahead of 980 nm pulses, the peak of time dependent fluorescent emission was slightly higher than the original strength. This was due

to the long lifetime characteristic of the Tm^{3+} intermediate state. The earlier arrived 808 nm photons were absorbed by the electron on ground state $^3H_6$, which were excited to $^3H_4$ and stayed due to the micro-second level lifetime. When the 980 nm photons joined, the electrons could be excited directly from $^3H_4$ to higher intermediate states. This could actually change the ratio of upconversion absorption process.

Meanwhile, if given shortened excitation pulse duration time and corresponding short depletion pulses, the depletion would happen with relatively low efficiency. This was because without enough excitation duration, the upconversion nanocrystal could not reach efficient population reversion, as shown in the Appendix.

We also measured the affection of temporal factor on depletion efficiency. We applied ms 980 nm excitation pulses while shortened 808 nm pulses with no longer than 100 us duration, as shown in Fig 3-8. Without enough depletion time, the upconversion process could not be restrained efficiently.

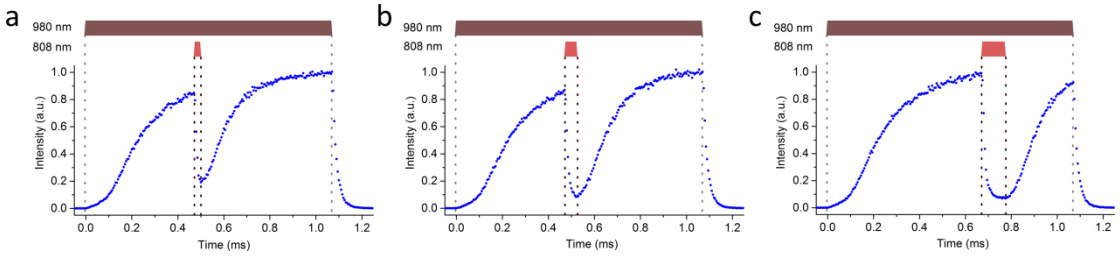

FIGURE 3-8 The temporal conditions for stimulated emission in highly-doped upconversion nanocrystals. (a-c)Transient responses of the 455 nm emission with fixed 980 nm pulse duration but different 808 nm pulse duration of 20, 50 and 100 μs, relatively. The 980 nm intensity is 0.6 MW/cm^2 and the 808 nm intensity is 7.57 MW/cm^2

3.2.5 Influence of power factor

In this section, we studied the influence of intensity factor on two wavelength modulation on Tm^{3+} dopant upconversion nanocrystals.

The controlled measurement was carried on high dopant $NaYF_4$:Yb^{3+}/Tm^{3+} upconversion nanocrystals with 8% Tm^{3+} and 20% Yb^{3+} dopant concentration. We also applied 1 milli-second pulse duration condition in our measurement. And the temporal

interval between 808 nm and 980 nm pulses started at 808 nm pulses coming 1 ms ahead of 980 nm with step of 0.5 ms, until 808 nm pulses were completely after 980 nm pulses.

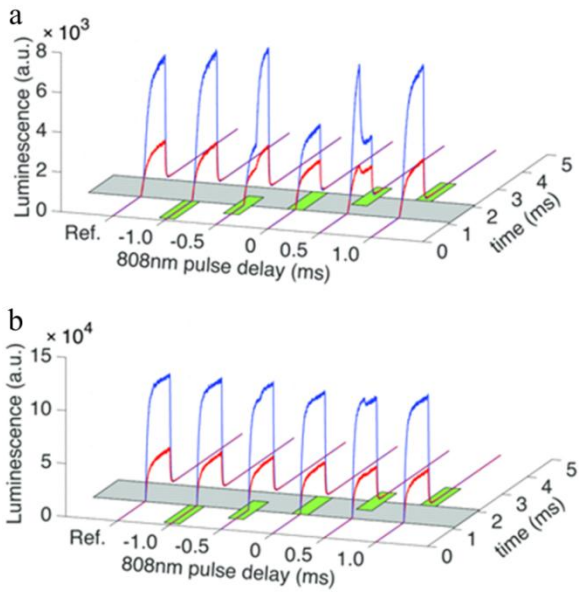

FIGURE 3-9 Transient responses of upconversion emission at 455 nm (blue curves) and 660 nm (red curves) from 8% Tm^{3+}-doped nanocrystals under pulsed 980 nm (grey shadows) and 808 nm (green shadows) illumination (Ref. curve is measured without 808 nm illumination). (a) 980 nm excitation intensity is 0.6 MW/cm^2 and (b) 980 nm excitation intensity is 6.0 MW/cm^2. The 808 nm probing intensity is fixed at 0.76 MW/cm^2. Pulse duration time is 1 ms and measurement period is 10 ms

As shown in Fig 3-9, the intensity of 808 nm was fixed at 0.76 MW/cm^2 while 980 nm intensity was raised up from 0.6 MW/cm^2(Fig 3-9a) to 6.0 MW/cm^2(Fig 3-9b). From the results, we could find that with higher excitation intensity, the depletion efficiency went much lower. More data could be find in Appendix. This was due to the competition of mutually independence of upconversion emission and stimulated emission process in upconversion nanocrystals. The excitation energy was absorbed by sensitizer originally meanwhile the depletion occurred on emitters directly and final emission results was dominated by the winner. When the 980 nm photons were absorbed by Yb^{3+}, the energy was then transmitted to Tm^{3+}, and given more energy, total transmitted energy rose up and it became harder to deplete the excited electrons. So the depletion efficiency was lowered down.

We then fixed the 980 nm excitation intensity to 0.6 MW/cm^2, and raised the 808 nm depletion intensity from 0.76 to 7.56 MW/cm^2. As shown in Fig 3-10, the more 808 nm

intensity, the higher depletion efficiency. This was in accordance to the result in the main figures.

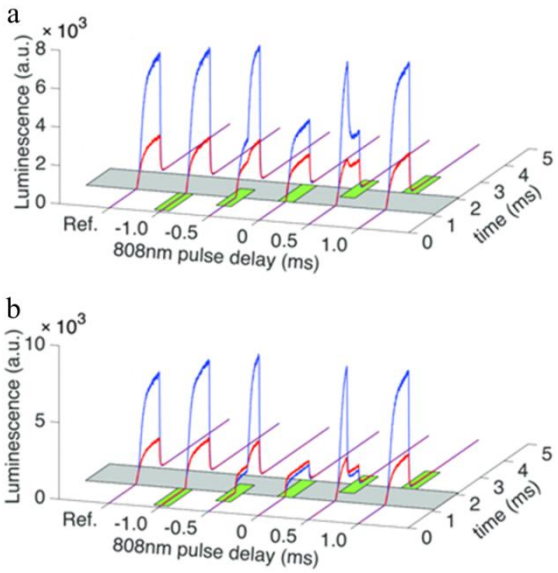

FIGURE 3-10 Transient responses of upconversion emission at 455 nm (blue curves) and 660 nm (red curves) from 8% Tm^{3+}-doped nanocrystals under pulsed 980 nm (grey shadows) and 808 nm (green shadows) illumination (Ref. curve is measured without 808 nm illumination). The 908 nm excitation intensity is fixed at 0.6 MW/cm^2. (a) 808 nm depletion intensity is 0.76 MW/cm^2 and (b) 808 nm depletion intensity is 7.57 MW/cm^2. Pulse duration time is 1 ms and measurement period is 10 ms

3.2.6 Influence of doping concentration

In the last section, we studied the influence of material factors on two wavelength modulation on Tm^{3+} dopant upconversion nanocrystals. We focused on the dopant concentration factor and intermediate state factor.

We combined the conditions tested in section 3.2.4 and 3.2.5, and carried on the controlled measurement on high dopant and low dopant emitter concentration while monitoring the temporal dependent fluorescent emission on $^1G_4$ and $^1D_2$ state. We used the 8% Tm^{3+} and 20% Yb^{3+} nanocrystals as high dopant sample and 1% Tm^{3+} and 20% Yb^{3+} as low dopant sample. The 660 nm emission from $^1G_4$ and 455 nm emission from $^1D_2$ was collected.

We applied 1 milli-second pulse duration condition in our measurement. And the temporal interval between 808 nm and 980 nm pulses started at 808 nm pulses coming 1

ms ahead of 980 nm with step of 0.5 ms, until 808 nm pulses were completely after 980 nm pulses.

Under different excitation and depletion intensity combinations, the high dopant concentration sample presented higher depletion efficiency on $^1D_2$ state than $^1G_4$ state, as shown in Fig 3-11. This was because the upconversion progress would become more challenging for higher intermediate state. The upconversion to higher intermediate state was easier affected by the ladder depletion mechanism.

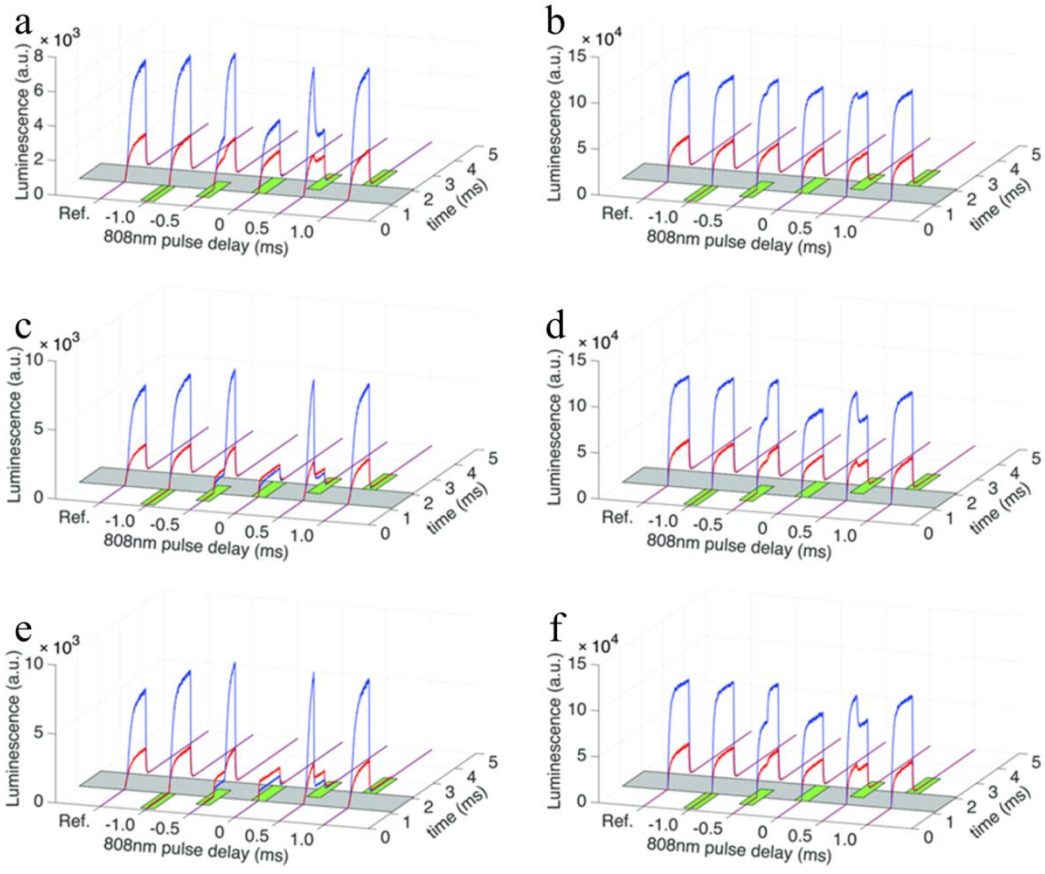

FIGURE 3-11 Transient responses of upconversion emission at 455 nm (blue curves) and 660 nm (red curves) from 8% Tm^{3+}-doped nanocrystals under pulsed 980 nm (grey shadows) and 808 nm (green shadows) illumination of varied temporal arrangements (Ref. curves are measured without 808 nm illumination). The 980 nm excitation intensity is 0.6 MW/cm^2 for (a)(c)(e) and 6.0 MW/cm^2 for (b)(d)(f), and the 808 nm probing intensity is 0.76 MW/cm^2 for (a)(b), 7.57 MW/cm^2 for (c)(d) and 30.3 MW/cm^2 for (e)(f)

For low dopant concentration condition, comparing with high dopant sample, low dopant sample presented more absorption and fluorescent signal enhancement rather than

depletion, as shown in Fig 3-12. This directly proved that with larger distance between emitters, the rate of cross-relaxation would largely reduce thus the population reversion became extremely challenging to occur. On the other hand, due to the low dopant concentration, one emitter shared more nearby sensitizers and could be transmitted with more energy from nearby sensitizers, which would make depletion more difficult to happen. Similarly, if given higher sensitizer dopant concentration, the depletion efficiency would also be largely reduced due to the same reason of higher sensitizer to emitter ratio. More measurement data under other conditions could be find in Appendix.

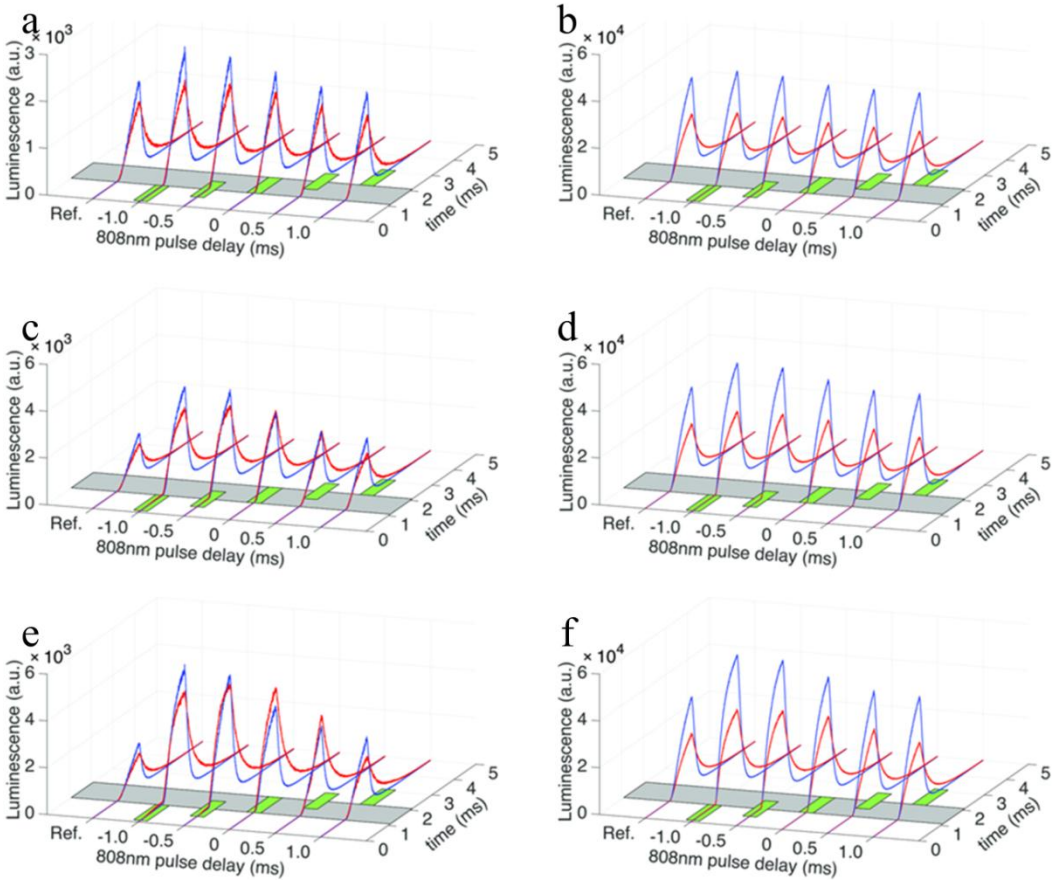

FIGURE 3-12 Transient responses of upconversion emission at 455 nm (blue curves) and 660 nm (red curves) from 1% Tm3+-doped nanocrystals under pulsed 980 nm (grey shadows) and 808 nm (green shadows) illumination of varied temporal arrangements (Ref. curves are measured without 808 nm illumination). The 980 nm excitation intensity is 0.6 MW/cm^2 for (a)(c)(e) and 6.0 MW/cm^2 for (b)(d)(f), and the 808 nm probing intensity is 0.76 MW/cm^2 for (a)(b), 7.57 MW/cm^2 for (c)(d), and 30.3 MW/cm^2 for (e)(f).

3.2.7 Upconversion-STED super-resolution imaging

We further demonstrated the upconversion-STED super-resolution imaging using highly doped Tm nanocrystals. To modify the dual-laser confocal system into STED, a quarter-wave plate (WPQ10M-808, Thorlabs) was used to transform the 808 nm beam from linear polarisation to circular polarisation. In practice a half-wave plate (WPH10M-808, Thorlabs) was used together to facilitate the adjustment towards quality circular polarisation. A vortex phase plate (VPP-1a, RPC Photonics) was also inserted in the 808 nm beam path, so that a doughnut-shaped PSF was generated at the focal plane. The two beams of 980 nm and 808 nm were carefully aligned to ensure precise overlapping of their PSFs in xy plane and z direction, as shown in Fig 3-13. The FWHM of PSF for the fluorescent imaging part is 420 nm, which is the system resolution when the depletion beam is off.

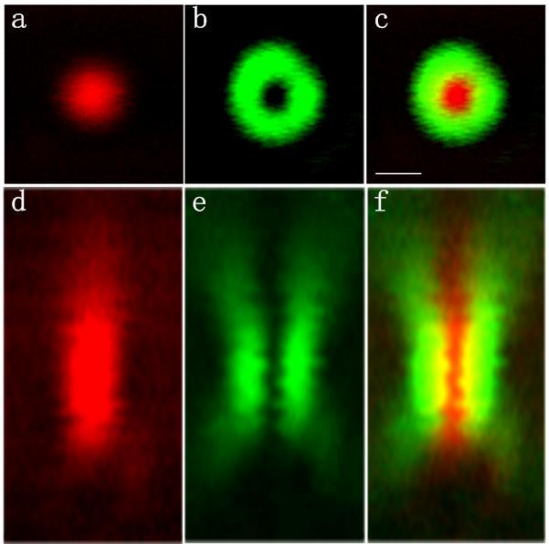

FIGURE 3-13 PSFs overlapping of excitation and doughnut STED beam. (a)PSF of 980 nm excitation on xy plane; (b)PSF of Doughnut 808 nm STED beam after modulation with vortex phase plate on xy plane; (c)Overlapping of two PSFs with high precision. (d)(e)(f) are corresponding psf to (a)(b)(c) in xz plane. Pixel dwell time: 0.2 ms. Scale bar: 1 μm

The nanocrystals imaged were about 80 nm in size and had 20% Yb^{3+} and 6% Tm^{3+} (Fig. 3-4g). The depletion power measured at the back aperture of the objective was around 79 mW, which equals to 56 MM/cm^2 at the focal plane. The theoretical resolution is improved by 13-fold compared to the confocal result, with ultimate resolution of 30 nm achieved. From the imaging result, as shown in Fig 3-14, the arrow line indicates a FWHM

of 98 nm on one single nanocrystal. Subtracting the nanocrystal size, we achieved the resolution of ~35 nm which is approximately 1/28 of the excitation wavelength.

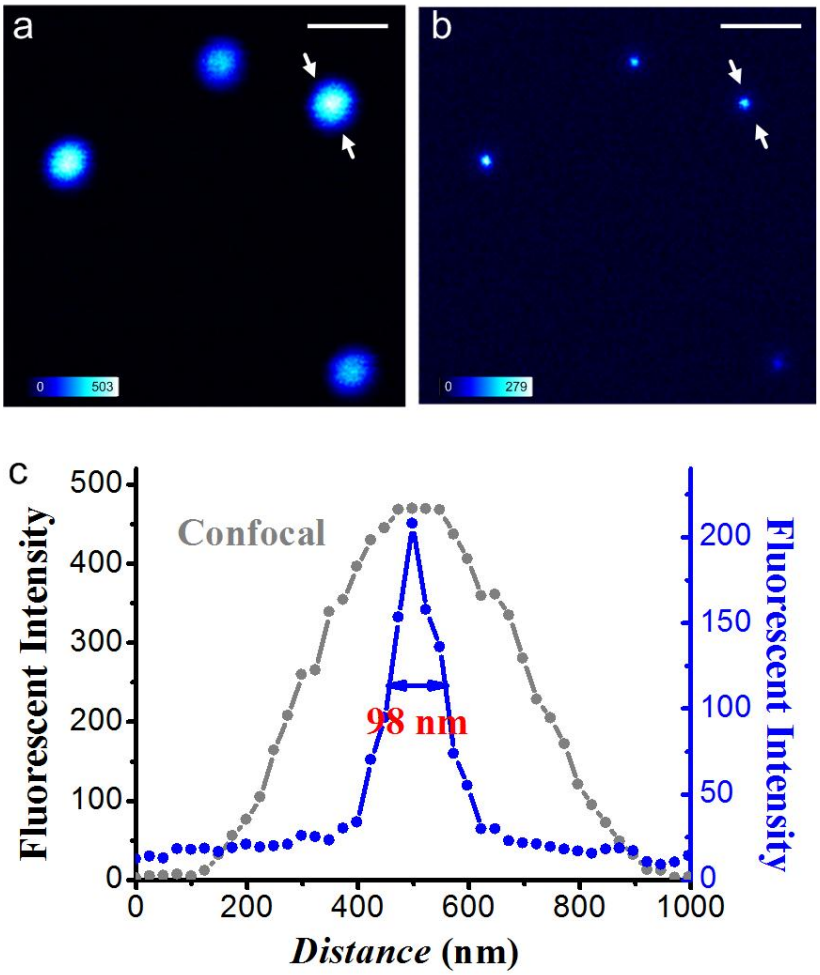

FIGURE 3-14 The CW STED super-resolution result on 6% dopant concentration Tm^{3+} $NaYF_4$:Yb^{3+}/Tm^{3+} nanocrystals. Confocal (a) and corresponding CW STED super-resolution result (b) images of upconversion nanocrystals; (c)The profile along the dashed line in a and b exhibits a spot size of 98 nm, indicating an effective resolution of ~35 nm after subtraction of the nanocrystal size. Pixel dwell time: 5 ms. The scale bar is 1 μm

3.3 Remarks

In this chapter we explored stimulated emission depletion for the $NaYF_4:Yb^{3+}/Tm^{3+}$ upconversion nanocrystals and applied them in upconversion-STED nanoscopy. With controlled measurements in doping concentration, power factor and temporal configuration, we successfully demonstrated low power intermediate-level STED-like operation on highly doped Tm^{3+} upconversion nanocrystals. This is promising to overcome the major challenge of extreme intensity requirement in traditional STED techniques. Interestingly, we observed luminescence enhancement on upconversion nanocrystals with low doping concentration. The detailed physical process is investigated in the next chapter.

Chapter 4

This chapter further studies the fundamental details and practical performance using upconversion nanocrystals for stimulated emission depletion nanoscopy. We reveal a key photon-avalanche-like process only found in highly doped upconversion nanocrystals, which forms a positive feedback process, leading to effective population inversion for amplified stimulated emission. This enables luminescence depletion at low intensity levels towards biological-friendly super-resolution imaging using the new upconversion-STED technique. This work is reported in the form of a journal paper published in *Nature*.

4.1 Contributions to Paper 3

TABLE 4-1 Author contribution summary for paper 3.

	Y.Liu	Y.Lu	X.Y.	X.Z.	S.W.	F.W.	X.V.	J.Zhao	D.L	Z.Z	C.M.	J.Zhou	J.A.P.	P.X.	D.J.
Experiment Design	•	•											•	•	•
System Setup	•		•	•		•									
Sample Preparation	•			•	•			•	•		•	•			
Data Collection	•	•	•	•						•					
Analysis	•	•	•				•							•	•
Manuscript and Figures	•	•	•				•							•	•

The basic idea was conceived by Jin and Piper in Macquarie University and Xi in Peking University as a collaboration to combine upconversion nanocrystals with STED super-resolution imaging, and was detailed during the period when Lu and I significantly involved in the project since 2012. I did major contributions to this work, including building the dual-laser confocal/STED system, coordinating sample preparation, conducting major optical experiments, and participating in data analysis, preparation of the manuscript and figures.

4.2 Paper 3

Liu Y, Lu Y, Yang X, Zheng X, Wen S, Wang F,Vidal X, Zhao J, Liu D, Zhou Z, Ma C, Zhou J, Piper J A, Xi P, Jin D, "Amplified stimulated emission in upconversion nanoparticles for super-resolution nanoscopy", accepted by *Nature* on 9th Jan 2017, DOI: 10.1038/nature21366.

LETTER

doi:10.1038/nature21366

Amplified stimulated emission in upconversion nanoparticles for super-resolution nanoscopy

Yujia Liu[1,2,3,4*], Yiqing Lu[1,2*], Xusan Yang[3*], Xianlin Zheng[1,2], Shihui Wen[1,5], Fan Wang[1,2,5], Xavier Vidal[1,2], Jiangbo Zhao[1,2], Deming Liu[1,2], Zhiguang Zhou[1,5], Chenshuo Ma[1], Jiajia Zhou[5], James A. Piper[1,2], Peng Xi[1,3] & Dayong Jin[1,2,5]

Lanthanide-doped glasses and crystals are attractive for laser applications because the metastable energy levels of the trivalent lanthanide ions facilitate the establishment of population inversion and amplified stimulated emission at relatively low pump power[1–3]. At the nanometre scale, lanthanide-doped upconversion nanoparticles (UCNPs) can now be made with precisely controlled phase, dimension and doping level[4,5]. When excited in the near-infrared, these UCNPs emit stable, bright visible luminescence at a variety of selectable wavelengths[6–9], with single-nanoparticle sensitivity[10–13], which makes them suitable for advanced luminescence microscopy applications. Here we show that UCNPs doped with high concentrations of thulium ions (Tm^{3+}), excited at a wavelength of 980 nanometres, can readily establish a population inversion on their intermediate metastable $^3H_4$ level: the reduced inter-emitter distance at high Tm^{3+} doping concentration leads to intense cross-relaxation, inducing a photon-avalanche-like effect that rapidly populates the metastable $^3H_4$ level, resulting in population inversion relative to the $^3H_6$ ground level within a single nanoparticle. As a result, illumination by a laser at 808 nanometres, matching the upconversion band of the $^3H_4 \rightarrow {}^3H_6$ transition, can trigger amplified stimulated emission to discharge the $^3H_4$ intermediate level, so that the upconversion pathway to generate blue luminescence can be optically inhibited. We harness these properties to realize low-power super-resolution stimulated emission depletion (STED) microscopy and achieve nanometre-scale optical resolution (nanoscopy), imaging single UCNPs; the resolution is 28 nanometres, that is, 1/36th of the wavelength. These engineered nanocrystals offer saturation intensity two orders of magnitude lower than those of fluorescent probes currently employed in stimulated emission depletion microscopy, suggesting a new way of alleviating the square-root law that typically limits the resolution that can be practically achieved by such techniques.

To investigate conditions for amplified stimulated emission from single Yb/Tm co-doped $NaYF_4$ UCNPs, we built a dual-laser confocal microscope (Extended Data Fig. 1). As illustrated in Fig. 1a, the photon upconversion process comprises absorption of 980 nm excitation by the Yb^{3+} sensitizers, stepwise transfer of that energy onto the scaffold energy levels of the Tm^{3+} emitters, and eventually upconverted emission from the two-photon $^3H_4$, three-photon $^1G_4$ or four-photon $^1D_2$ levels of Tm^{3+}. In the presence of population inversion between the $^3H_4$ intermediate level and the $^3H_6$ ground level, a probe laser beam with wavelength corresponding to the energy gap (that is, 808 nm for $^3H_4 \rightarrow {}^3H_6$) will trigger stimulated emission to discharge the $^3H_4$ level, consequently inhibiting upconverted emission from higher excited levels (for example, $^1G_4$ and $^1D_2$).

Figure 1b shows confocal images of single UCNPs highly doped with 8% Tm^{3+} ions (and 20% Yb^{3+}). The upconversion emission under

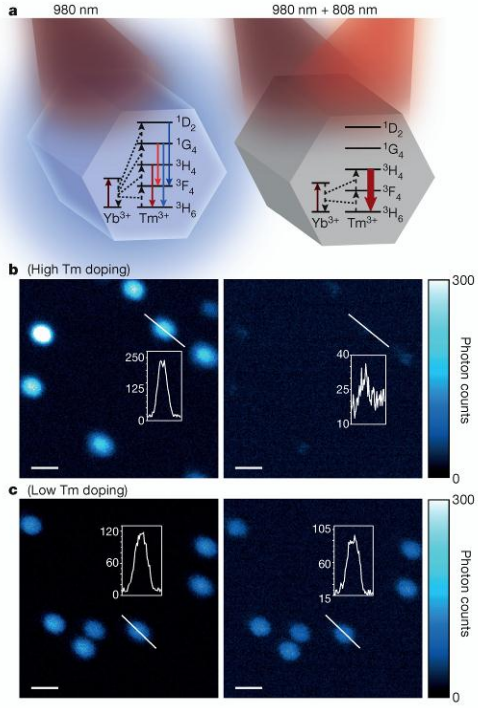

Figure 1 | Probing upconversion luminescence using dual-laser illumination. a, Energy level diagrams of Yb/Tm co-doped UCNPs under 980 nm illumination (left), and under both 980 nm and 808 nm illumination (right). See text for details. **b**, Confocal images in 455 nm upconversion emission of the 8% Tm-doped UCNPs under continuous-wave 980 nm laser (left) and under both 980 nm and 808 nm dual laser (right) illumination. **c**, As **b** but for 1% Tm-doped UCNPs. For **b** and **c**, the 980 nm and 808 nm laser powers measured at the objective back aperture were 1 mW and 5 mW, respectively. Each inset shows the luminescence signal profile along the diagonal white line in that panel across a typical nanocrystal. Pixel dwell time, 4 ms; scale bar, 500 nm.

[1]Advanced Cytometry Laboratories, ARC Centre of Excellence for Nanoscale BioPhotonics (CNBP), Macquarie University, Sydney, New South Wales 2109, Australia. [2]Department of Physics and Astronomy, Macquarie University, Sydney, New South Wales 2109, Australia. [3]Department of Biomedical Engineering, College of Engineering, Peking University, Beijing 100871, China. [4]School of Life Sciences and Biotechnology, Shanghai Jiao Tong University, Shanghai 200241, China. [5]Institute for Biomedical Materials and Devices (IBMD), Faculty of Science, University of Technology Sydney, Sydney, New South Wales 2007, Australia.
*These authors contributed equally to this work.

RESEARCH LETTER

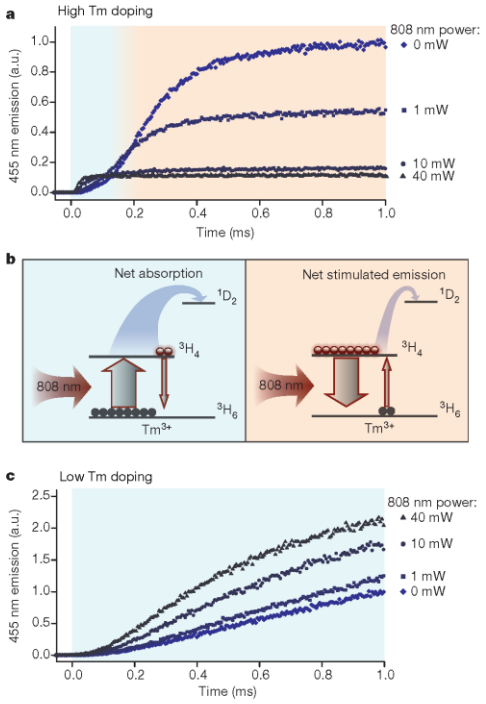

Figure 2 | Competition between absorption and stimulated emission. **a**, Transient response of the 455 nm emission from 8% Tm-doped UCNPs under synchronous 980 nm and 808 nm pulses (1 ms duration). The 980 nm laser power was fixed at 1 mW, while the 808 nm laser power was varied from 0 to 40 mW (both at the objective back aperture). **b**, Diagrams illustrating net absorption (left) and net stimulated emission (right) between $^3H_4$ and $^3H_6$ levels when the UCNPs under 980 nm excitation were probed with the 808 nm laser, which then led to either inhibition or enhancement of the further upconverted emission. See text for details. **c**, As **a** but for 1% Tm-doped UCNPs.

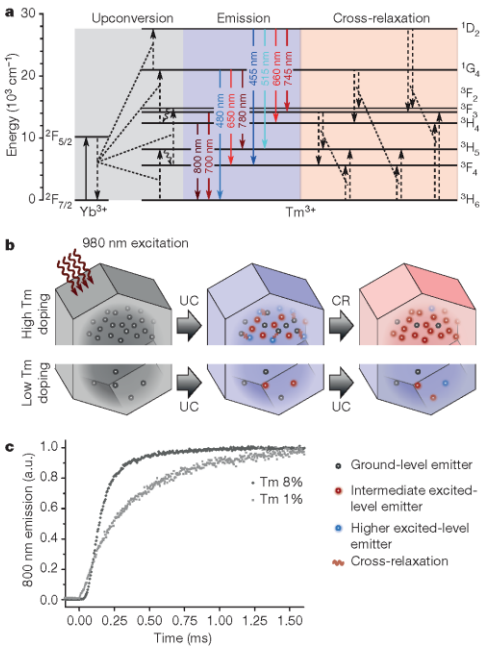

Figure 3 | The photon-avalanche-like process underlying enhanced population inversion. **a**, Energy level diagram of Yb/Tm co-doped UCNPs including typical cross-relaxation pathways among Tm^{3+} emitters. Solid arrows, excitation and emission; curved arrows, non-radiative relaxation; dashed arrows connected by dotted lines, energy transfer processes. **b**, Diagrams of the photon-avalanche-like process, which stems from the intense cross-relaxation among emitters in a highly doped nanocrystal only (sensitizers are not shown). UC, upconversion; CR, cross-relaxation. **c**, Transient response of the upconverted emission measured at 800 nm from 8% and 1% Tm-doped UCNPs after the 980 nm excitation was switched on at time = 0 ms (in the absence of the 808 nm probing beam). The 980 nm laser power was 1 mW at the objective back aperture.

continuous-wave (CW) 980 nm excitation was clearly inhibited once a CW 808 nm probe beam was applied. By contrast, under the same experiment conditions, the UCNPs with low doping concentration (conventionally 1% Tm^{3+} and 20% Yb^{3+}) showed negligible optical switching effects (Fig. 1c).

Since the 808 nm probe matches only the $^3H_4 \rightarrow {}^3H_6$ transition (no upconversion emission is observed under 808 nm excitation alone, Extended Data Fig. 2), inhibition of visible upconversion emission by the 808 nm probe is concrete evidence for population inversion and net stimulated emission on $^3H_4 \rightarrow {}^3H_6$; if this were not so, visible upconversion emission would be enhanced because of the increased optical pumping to $^3H_4$. To confirm this, we measured the transient response of the upconversion emission at 455 nm (Fig. 2) and at 650 nm (Extended Data Fig. 3) using synchronized 980 nm and 808 nm pulses. Initially, the emission from 8% Tm-doped UCNPs is indeed enhanced (Fig. 2a), indicating that the absorption of 808 nm dominates (cartoon shown in Fig. 2b left). The more intense the 808 nm beam, the more obvious the initial enhancement. However increase of the upconversion emission is rapidly truncated once sufficient 980 nm energy is transferred to Tm^{3+} ($^3H_4$) acceptors to establish a population inversion, whereupon stimulated emission on $^3H_4 \rightarrow {}^3H_6$ dominates and upconversion emissions from the three- and four-photon levels of $^1G_4$ and $^1D_2$ are short-circuited (cartoon shown in Fig. 2b right). By contrast, for 1% Tm-doped nanocrystals, the build-up of upconversion emission is accelerated by the probe 808 nm beam (that is, enhancement; corresponding to Fig. 2b left), showing no sign of population inversion over the same period of time (Fig. 2c).

The differences shown above between the two UCNPs of different Tm^{3+} concentrations indicate that the critical population inversion is driven by a key mechanism related to the doping concentration, which we ascribe to a photon-avalanche-like process. This refers to the intense cross-relaxation between emitters such that those in a higher excited energy level have high probability for transfer of energy to a nearby emitter in the ground or lower energy level instead of undergoing other relaxation pathways, forming a positive feedback process accelerating the accumulation of emitters in intermediate excited energy levels. Unlike ordinary photon avalanche, however, the condition of non-resonant ground-level absorption is not met with co-doped UCNPs containing sensitizers and emitters, so that the threshold behaviour of photon avalanche is absent[14–17] (see Methods and Extended Data Fig. 4 for discussion). For the Tm-doped UCNPs, the similarly spaced energy levels of Tm^{3+} provide abundant cross-relaxation pathways (Fig. 3a). The cross-relaxation coefficients are

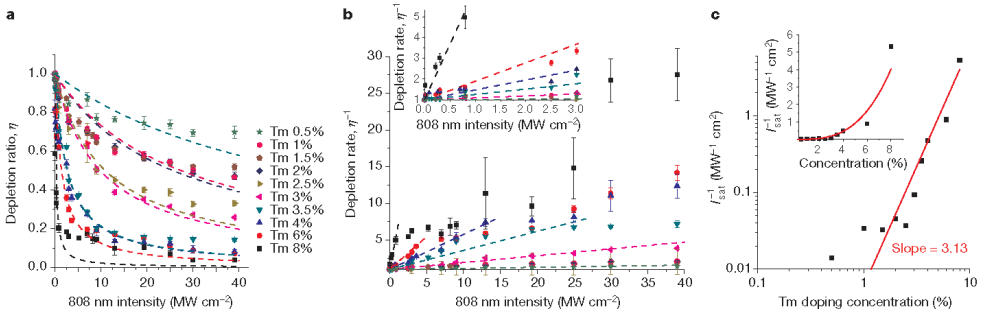

Figure 4 | Optical switching efficiency with respect to Tm doping concentration. a, Depletion ratio of the upconversion emission at 455 nm, as a result of intermediate-level stimulated emission, under continuous-wave 980 nm excitation at a fixed intensity of 0.66 MW cm^{-2} and 808 nm intensities up to 39 MW cm^{-2}, measured for a series of UCNPs with incremental Tm doping concentrations from 0.5 to 8 mol%. Dashed lines are fitted curves using the form $\eta = (1 + I_{808}/I_{sat})^{-1}$, where I_{sat} denotes the saturation intensity. **b**, The depletion ratio data in **a** are inverted to illustrate the linear relation $\eta^{-1} = 1 + I_{808}/I_{sat}$. In the inset, the dashed lines are fitted using all data points; in the main panel, linear curve fitting for Tm concentrations ≥3.5% uses only data points at low 808 nm intensity. At high 808 nm intensity, the reciprocals of depletion ratio start to deviate from linearity towards plateaus. Error bars in **a** and **b**, ±1 s.d. with $n = 5$ each. **c**, Inverse of the saturation intensity values obtained by linear curve fitting in **b** in relation to the Tm doping concentration, plotted on a log–log scale in the main panel and on a linear scale in the inset.

enhanced quadratically as the doping concentration increases (assuming that energy transfer between two ions is inversely proportional to the sixth power of their separation[18,19], and that the average separation distance is the cube root of the reciprocal of the doping concentration), so that cross-relaxation dominates when the emitters are close enough to each other (Fig. 3b).

The presence or absence of the photon-avalanche-like process was experimentally verified by measuring the transient response of the upconversion emission from the $^3H_4$ level under excitation by a single wavelength of 980 nm. The 800 nm upconversion emission of the 8% Tm-doped nanocrystals exhibited an 'S' shape over the build-up period (Fig. 3c), which is a signature of photon avalanche[14,15,17,20]. In contrast, for the 1% Tm-doped nanocrystals, the increase of 800 nm emission took place immediately upon 980 nm excitation. Theoretically, the precondition for photon avalanche is when the cross-relaxation coefficient surpasses the intrinsic decay rate from the higher excited level to the ground level, thereby producing positive feedback[14,16]. By fitting the transient responses of the 8% Tm-doped nanocrystals to rate equations, we show that the rate parameters obtained satisfy this requirement (Extended Data Fig. 5); in contrast, for 1% Tm-doped UCNPs where the cross-relaxation coefficients are reduced quadratically with the doping concentration (that is, dividing the coefficients by 64), the photon avalanche condition is not satisfied.

To determine the critical Tm^{3+} doping concentration for enhanced population inversion, a series of ten batches of 40-nm UCNPs were synthesized with incremental Tm concentrations from 0.5 mol% to 8 mol% (Extended Data Fig. 6). Under dual-laser CW illumination, the optical depletion ratio (that is, the ratio of the emission strength in the presence of the 808 nm depletion probe to that in the absence of that probe) of the 455 nm emission was measured as a function of the 808 nm intensity. As shown in Fig. 4a, within the available power range of the 808 nm laser, only UCNPs with Tm doping concentration >2% can have more than 50% of their emission switched off. For Tm doping concentrations above 4%, optimum depletion ratios above 90% can be achieved.

The saturation intensities, denoting the particular values of the probe intensity that halve the upconverted emission, were calculated from a plot of the inverse of the depletion ratio against the 808 nm intensity via linear curve fitting (Fig. 4b)[21,22]. The linearity found for UCNPs with Tm doping ≥3.5% holds only at low 808 nm intensity; at greater intensities, the fit becomes dual- or multi-segment, which suggests that the depletion efficiency for the highly-doped UCNPs is power dependent, and can be substantially amplified by the photon-avalanche-like effect. Those data points appearing with a linear fit in the low 808 nm intensity range show reduction of saturation intensities by more than two orders of magnitude (from 71.4 MW cm^{-2} to 0.19 MW cm^{-2}) as the Tm doping increases from 0.5% to 8%. Once the stimulated emission depletion at low intensity levels of the 808 nm illumination consumes the established population inversion, a balance is re-established between absorption and stimulated emission, and further inhibition of upconversion emission is diminished at higher 808 nm intensities (Extended Data Fig. 7).

The small saturation intensity of highly doped UCNPs suggests that the photon-avalanche-like effect in single UCNPs alleviates the square root law that all current super-resolution nanoscopy methods obey. Plotting the inverse of saturation intensity against the Tm doping concentration on a log–log scale shows a slope of 3.13 (Fig. 4c), suggesting that the saturation intensity is proportional to the average Tm–Tm distance to the ninth power. Both Fig. 4c and b confirm that the saturation intensities in upconversion materials are highly dependent on the doping concentration of emission centres, showing that the photon-avalanche-like effect plays the key role in bringing down the intensity requirement for stimulated emission depletion.

We further explored the use of highly doped UCNPs for optical super-resolution imaging; the 808 nm beam was spatially modulated to produce a doughnut-shaped point spread function (PSF) that overlapped with the Gaussian PSF of the 980 nm excitation beam at the focal plane (illustrated in Fig. 5a). The nanocrystals on the periphery of the 980 nm PSF would therefore be expected to be optically switched off by the 808 nm beam, leading to an effective excitation spot smaller than the optical diffraction limit, similar to the situation in STED microscopy[21]. To prove the concept, two samples of monodispersed UCNPs, both doped with 8% Tm and 20% Yb, were carefully characterized by transmission electron microscopy (TEM), showing average sizes of 39.8 and 12.9 nm, respectively (Fig. 5b and c). A region with a size comparable to the optical diffraction limit but containing three 40-nm UCNPs was selected, and a sequence of far-field optical super-resolution images that clearly resolve the adjacent UCNPs were recorded (Fig. 5d). Spot sizes of 48.3 nm were obtained by our upconversion-STED microscopy at an 808 nm intensity of 9.75 MW cm^{-2} (Fig. 5e and f). As the measured full-width at half-maximum (FWHM) is a convolution between the theoretical resolution and the physical size of the nanoparticle, this only gives the upper bound of the actual PSF size. Deconvolution based on the simple Pythagorean equation[23] shows this result corresponds

RESEARCH LETTER

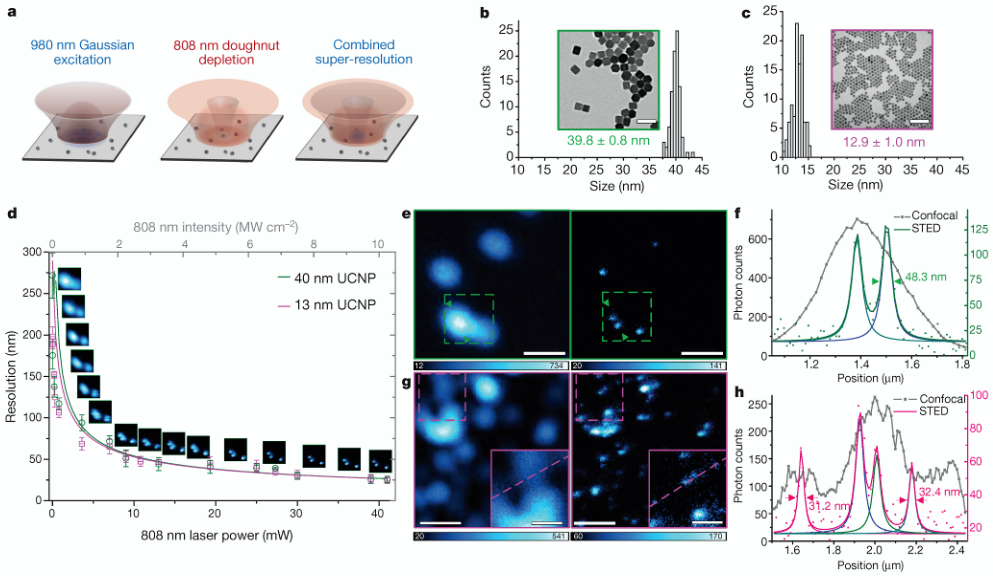

Figure 5 | Super-resolution imaging of the highly-doped UCNPs. **a**, Diagrams of the upconversion-STED super-resolution imaging, in which a Gaussian excitation profile (980 nm) and a Gauss–Laguerre mode 'doughnut' depletion profile (808 nm) at far field are employed. **b**, **c**, Inset, TEM images of two samples of 8% Tm-doped UCNPs revealing an average size of 39.8 and 12.9 nm; main panel, size dispersion. Scale bar, 100 nm. **d**, The resolution enhancement obtained with an increase of depletion intensity. The lines are fitted to $d_{STED} = d_C/(1 + aI_{STED})^{1/2}$, in which d_C is the FWHM of the confocal spot ($I_{STED} = 0$), and a is a constant proportional to I_{sat}. The CW 980 nm excitation was kept at 0.66 MW cm^{-2}. Pixel dwell time, 4 ms; error bars, ±1 s.d. with $n = 5$ each. Insets, upconversion-STED images of 40-nm UCNPs producing the data shown. **e**, Confocal (left) and super-resolution (right) images of the 40-nm 8% Tm-doped UCNPs. The 980 nm and 808 nm intensities were 0.66 and 9.75 MW cm^{-2}, respectively. Pixel dwell time, 4 ms; scale bars, 500 nm. Dashed boxes mark an area containing closely spaced 13-nm UCNPs that can be resolved in upconversion-STED but not in confocal imaging. **f**, Intensity profiles between the arrows across two UCNPs in **e**, showing an FWHM of 48.3 nm after Gaussian fitting. **g**, As **e** but for the 13-nm 8% Tm-doped UCNPs. The 980 nm and 808 nm intensities were 0.66 and 7.5 MW cm^{-2}, respectively. Pixel dwell time, 6 ms; scale bars, 500 nm for the main images and 200 nm for the insets. Dashed boxes mark an area containing closely spaced 13-nm UCNPs that can be resolved in upconversion-STED but not in confocal imaging, and are shown enlarged in the insets marked by solid boxes. **h**, Intensity profiles along the dashed lines across four UCNPs in **g**, showing an FWHM around 32 nm after Gaussian fitting.

to a markedly improved resolution of 27.4 nm, representing a 13-fold improvement over the optical diffraction limit, or 1/36 of the excitation wavelength. We subsequently examined 12.9-nm UCNPs and observed spot FWHM of 31.2 nm (Fig. 5g and h), corresponding to a resolution of 28.4 nm, which confirms the resolution for the present upconversion-STED system of ~28 nm.

Compared with earlier use of UCNPs in super-resolution microscopy[24], the upconversion-STED we report here is superior in two respects—it has a simple set-up involving two near-infrared diode lasers, and it uses $NaYF_4$, which is the most efficient crystal host found so far for bright and tunable upconversion emissions, offering multiple colours and luminescence lifetimes to realize multiplexing. In addition to excellent photostability (Extended Data Fig. 8), sensitivity and versatility, highly doped UCNPs now offer efficient optical switching with saturation intensity as low as 0.19 MW cm^{-2}. This provides a large contrast to conventional fluorescent probes (for example, Alexa Fluor and ATTO dyes) and luminescent nanoparticles (for example, semiconductor quantum dots and nanodiamonds with defect emission centres) previously used for STED microscopy with saturation intensities of 1–240 MW cm^{-2} (refs 21, 25, 26). Owing to the square root relation between resolution and laser power[22,27], extremely high depletion intensities (typically 260–800 mW at the objective back aperture) in the CW-STED mode are required to achieve resolution at the 30 nm level, intensities which not only exacerbate photobleaching of the probes, but also cause thermal damage to biological samples.

The luminescence lifetimes of UCNPs are typically from tens of microseconds to milliseconds, which stems from the forbidden nature of the 4*f*–4*f* transitions of trivalent lanthanide ions. In principle, longer lifetimes should lower the intensity requirement of the depletion beam in normal STED microscopy, but this is not obvious with low-doped UCNPs[28], possibly as a result of the correspondingly reduced cross-section for absorption/stimulated emission. The efficient optical switching (depletion) found only for highly doped UCNPs indicates that the photo-avalanche-like effect plays the key role in establishing population inversion to overcome the reduced cross-section, allowing a depletion beam at low intensity levels to be used in our upconversion-STED system. The low saturation intensity achieved by enhanced population inversion also suggests new approaches to identifying more suitable luminescent probes for STED. On the other hand, in our system, a pixel dwell time at least one order of magnitude higher than that used in conventional STED microscopy is necessary to compensate for the low emission rates associated with the long luminescence lifetimes. New crystal design and synthesis that will allow UCNPs with Tm doping concentration beyond 8% need to be explored, which will both enhance the brightness[12,13] and shorten the lifetime[9] of the upconversion luminescence, thereby shortening pixel dwell time as well as

further reducing saturation intensity. The longer imaging acquisition times for STED based on UCNPs might also be circumvented by employing parallelized scanning with beam arrays in the future[29].

In conclusion, we note that a variety of bioconjugation methods have been developed that make $NaYF_4$ nanocrystals usable as molecular probes for bioimaging[30], and with improved protocols to avoid non-specific binding and aggregation, we believe that highly doped UCNPs together with the upconversion-STED technique reported here will be important in nanoscale biology investigations. The present results also suggest new approaches to developing nanoscale lasers[31] and other nanophotonics applications demanding amplification by simulated emission at the nanoscale[32,33].

Online Content Methods, along with any additional Extended Data display items and Source Data, are available in the online version of the paper; references unique to these sections appear only in the online paper.

Received 23 August 2016; accepted 4 January 2017.
Published online 22 February 2017.

1. Urquhart, P. Review of rare-earth doped fiber lasers and amplifiers. *IEE Proc. J. Optoelectron.* **135,** 385–402 (1988).
2. Stoneman, R. C. & Esterowitz, L. Efficient, broadly tunable, laser-pumped Tm-YAG and Tm-YSGG CW lasers. *Opt. Lett.* **15,** 486–488 (1990).
3. Jackson, S. D. Towards high-power mid-infrared emission from a fibre laser. *Nat. Photon.* **6,** 423–431 (2012).
4. Wang, F. *et al.* Simultaneous phase and size control of upconversion nanocrystals through lanthanide doping. *Nature* **463,** 1061–1065 (2010).
5. Liu, D. *et al.* Three-dimensional controlled growth of monodisperse sub-50 nm heterogeneous nanocrystals. *Nat. Commun.* **7,** 10254 (2016).
6. Mai, H.-X., Zhang, Y.-W., Sun, L.-D. & Yan, C.-H. Highly efficient multicolor up-conversion emissions and their mechanisms of monodisperse $NaYF_4$:Yb,Er core and core/shell-structured nanocrystals. *J. Phys. Chem. C* **111,** 13721–13729 (2007).
7. Chen, G., Ohulchanskyy, T. Y., Kumar, R., Agren, H. & Prasad, P. N. Ultrasmall monodisperse $NaYF_4$:Yb^{3+}/Tm^{3+} nanocrystals with enhanced near-infrared to near-infrared upconversion photoluminescence. *ACS Nano* **4,** 3163–3168 (2010).
8. Wang, F. *et al.* Tuning upconversion through energy migration in core-shell nanoparticles. *Nat. Mater.* **10,** 968–973 (2011).
9. Lu, Y. *et al.* Tunable lifetime multiplexing using luminescent nanocrystals. *Nat. Photon.* **8,** 33–37 (2014).
10. Wu, S. *et al.* Non-blinking and photostable upconverted luminescence from single lanthanide-doped nanocrystals. *Proc. Natl Acad. Sci. USA* **106,** 10917–10921 (2009).
11. Park, Y. I. *et al.* Nonblinking and nonbleaching upconverting nanoparticles as an optical imaging nanoprobe and T1 magnetic resonance imaging contrast agent. *Adv. Mater.* **21,** 4467–4471 (2009).
12. Zhao, J. *et al.* Single-nanocrystal sensitivity achieved by enhanced upconversion luminescence. *Nat. Nanotechnol.* **8,** 729–734 (2013).
13. Gargas, D. J. *et al.* Engineering bright sub-10-nm upconverting nanocrystals for single-molecule imaging. *Nat. Nanotechnol.* **9,** 300–305 (2014).
14. Joubert, M. F., Guy, S. & Jacquier, B. Model of the photon-avalanche effect. *Phys. Rev. B* **48,** 10031–10037 (1993).
15. Collings, B. C. & Silversmith, A. J. Avalanche up-conversion in LaF_3Tm^{3+}. *J. Lumin.* **62,** 271–279 (1994).
16. Auzel, F. & Chen, Y. Photon avalanche luminescence of Er^{3+} ions in $LiYF_4$ crystal. *J. Lumin.* **65,** 45–56 (1995).
17. Scheps, R. Upconversion laser processes. *Prog. Quantum Electron.* **20,** 271–358 (1996).
18. Selvin, P. R. The renaissance of fluorescence resonance energy transfer. *Nat. Struct. Biol.* **7,** 730–734 (2000).
19. Rabouw, F. T., den Hartog, S. A., Senden, T. & Meijerink, A. Photonic effects on the Forster resonance energy transfer efficiency. *Nat. Commun.* **5,** 3610 (2014).
20. Auzel, F. Upconversion and anti-Stokes processes with f and d ions in solids. *Chem. Rev.* **104,** 139–174 (2004).
21. Willig, K. I., Harke, B., Medda, R. & Hell, S. W. STED microscopy with continuous wave beams. *Nat. Methods* **4,** 915–918 (2007).
22. Leutenegger, M., Eggeling, C. & Hell, S. W. Analytical description of STED microscopy performance. *Opt. Express* **18,** 26417–26429 (2010).
23. Donnert, G. *et al.* Macromolecular-scale resolution in biological fluorescence microscopy. *Proc. Natl Acad. Sci. USA* **103,** 11440–11445 (2006).
24. Kolesov, R. *et al.* Super-resolution upconversion microscopy of praseodymium-doped yttrium aluminum garnet nanoparticles. *Phys. Rev. B* **84,** 153413 (2011).
25. Han, K. Y. *et al.* Three-dimensional stimulated emission depletion microscopy of nitrogen-vacancy centers in diamond using continuous-wave light. *Nano Lett.* **9,** 3323–3329 (2009).
26. Hanne, J. *et al.* STED nanoscopy with fluorescent quantum dots. *Nat. Commun.* **6,** 7127 (2015).
27. Harke, B. *et al.* Resolution scaling in STED microscopy. *Opt. Express* **16,** 4154–4162 (2008).
28. Wu, R. *et al.* Optical depletion mechanism of upconverting luminescence and its potential for multi-photon STED-like microscopy. *Opt. Express* **23,** 32401–32412 (2015).
29. Chmyrov, A. *et al.* Nanoscopy with more than 100,000 'doughnuts'. *Nat. Methods* **10,** 737–740 (2013).
30. Sedlmeier, A. & Gorris, H. H. Surface modification and characterization of photon-upconverting nanoparticles for bioanalytical applications. *Chem. Soc. Rev.* **44,** 1526–1560 (2015).
31. He, L., Ozdemir, S. K., Zhu, J., Kim, W. & Yang, L. Detecting single viruses and nanoparticles using whispering gallery microlasers. *Nat. Nanotechnol.* **6,** 428–432 (2011).
32. Koenderink, A. F., Alù, A. & Polman, A. Nanophotonics: shrinking light-based technology. *Science* **348,** 516–521 (2015).
33. Buchegger, B. *et al.* Stimulated emission depletion lithography with mercapto-functional polymers. *ACS Nano* **10,** 1954–1959 (2016).

Acknowledgements This project was primarily supported by the Australian Research Council (ARC) Future Fellowship Scheme (D.J., FT 130100517), the ARC Centre of Excellence for Nanoscale BioPhotonics (CE140100003), the Natural Science Foundation of China (61428501, 31327901, 61475010), and the National Instrumentation Project of China (2013YQ03065102). Y. Lu acknowledges support from a Macquarie University Research Fellowship.

Author Contributions D.J. and P.X. conceived the project. D.J., P.X. and J.A.P. supervised the research. Y. Liu, X.Y., F.W., X.Z. and Z.Z. conducted the optical experiments. S.W., J. Zhao, D.L., J. Zhou, and C.M. synthesized the upconversion nanoparticles. Y. Lu carried out the modelling. Y. Lu, Y. Liu, X.Y., X.Z., X.V., P.X. and D.J. analysed the results, prepared the figures and wrote the manuscript. All authors participated in discussion and editing of the manuscript.

Author Information Reprints and permissions information is available at www.nature.com/reprints. The authors declare no competing financial interests. Readers are welcome to comment on the online version of the paper. Correspondence and requests for materials should be addressed to P.X. (xlpeng@pku.edu.cn), Y. Lu (yiqing.lu@mq.edu.au) or D.J. (dayong.jin@uts.edu.au).

Reviewer Information *Nature* thanks Y. D. Suh and the other anonymous reviewer(s) for their contribution to the peer review of this work.

RESEARCH LETTER

METHODS

Dual-laser confocal/super-resolution microscope. The optical system was built on a sample scanning configuration employing a 3-axis closed-loop piezo stage (stage body MAX311D/M, piezo controller BPC303; Thorlabs). Illustrated in Extended Data Fig. 1, a single-mode fibre-coupled 980 nm diode laser (LE-LS-980-300-FCS, LEO Photonics; maximum output power 300 mW) was used as the excitation source. After collimation, the excitation beam was transmitted through a long-pass dichroic mirror (ZT860lpxr, Chroma), then reflected by a second short-pass dichroic mirror (T750spxrxt, Chroma), and focused through an oil-immersion objective (UPlanAPO, Olympus; 100×, NA = 1.4) onto the sample slide. The first dichroic mirror also allowed the 808 nm probing beam from a polarization-maintaining fibre-coupled diode laser (LU0808M250-1C16F30A, Lumics; single mode, linear polarization, maximum output power 250 mW) to merge with the 980 nm beam. The luminescence signal from the sample was collected by the same objective, split from the excitation and probing beams by the second dichroic mirror, before being coupled into a multi-mode fibre (M24L01, Thorlabs). The other end of the fibre was connected to a single-photon avalanche diode (SPAD; SPCM-AQRH-13-FC, PerkinElmer) capable of being time-gated electronically. To select upconversion emission bands, different band-pass filters (FF01-448/20-25 and FF01-660/13-25, Semrock) were inserted in the detection path for both transient response measurement and confocal imaging. The distal end of the multi-mode fibre could also be switched to a miniature monochromator (MicroHR Auto, Horiba) equipped with a second SPAD for measuring upconversion emission spectra (Extended Data Fig. 2).

For measuring the 800 nm transient response under 980 nm excitation only (Fig. 3c), the distal end of the multi-mode fibre connected to the SPAD was substituted for the distal end of the polarization-maintaining fibre of the 808 nm laser, with a band-pass filter (FB800-10, Thorlabs) also inserted in the beam path.

For acquiring optical super-resolution images, a quarter-wave plate (WPQ10M-808, Thorlabs) was used to first transform the 808 nm beam from linear polarization to circular polarization. In practice a half-wave plate (WPH10M-808, Thorlabs) was also used to facilitate the adjustment towards quality circular polarization. Then, a vortex phase plate (VPP-1a, RPC Photonics) was inserted in the 808 nm beam path, so that a doughnut-shaped PSF was generated at the focal plane. In both cases of dual-laser confocal and super-resolution imaging, the two beams of 980 and 808 nm were carefully aligned to ensure precise overlapping of their PSFs in both X–Y and Z directions.

Synthesis of UCNPs. To produce 40-nm $NaYF_4$:Yb,Tm UCNPs with precisely controlled size, we first synthesized core nanocrystals using the organometallic method, followed by epitaxial growth via a hot-injection protocol. To obtain the core nanocrystals, 5 ml of a methanol solution of $LnCl_3$ (Ln = Y/Yb/Tm, 1.0 mmol in total) together with 6 ml oleic acid (OA) and 15 ml 1-octadecene (ODE) were added to a 50 ml three-neck round-bottom flask. The resulting mixture was heated at 170 °C under argon flow for 30 min to form a transparent solution of light yellow colour. The solution was cooled down to 50 °C, and 5 ml of methanol solution containing 4.0 mmol NH_4F and 2.5 mmol NaOH was added with vigorous stirring for 30 min. Then, the mixture was slowly heated to 150 °C and kept for 20 min under argon flow to remove methanol and residual water. Next, the solution was quickly heated to 300 °C, and maintained at that temperature for 1.5 h. The slurry was then cooled down and the products were isolated by addition of ethanol and centrifugation. After washing with cyclohexane/ethanol several times, the core nanocrystals were re-dispersed in cyclohexane at a concentration of 20 mg ml^{-1}.

The same procedures were repeated one more time, until the step where the reaction solution was slowly heated to 150 °C and kept for 20 min. Instead of further heating to 300 °C to trigger nanocrystal growth, the solution was cooled down to room temperature to yield the shell precursors.

For epitaxial growth, 1.5 ml as-prepared core nanocrystals were added to a 50 ml flask containing 6 ml OA and 6 ml ODE. The mixture was heated to 170 °C under argon for 30 min, and then further heated to 300 °C. Next, 0.25 ml as-prepared shell precursors were injected into the reaction mixture and ripened at 300 °C for 4 min, followed by the same injection and ripening cycles for approximately 16 times. Finally, the slurry was cooled down to room temperature and the formed nanocrystals were purified according to the same procedure used for the core nanocrystals.

The protocol for synthesizing 13-nm $NaYF_4$ nanocrystals co-doped with 20% Yb and 8% Tm is similar to the one above for producing the core nanocrystals, except for the temperature control profile. 5 ml of methanol solution containing 0.72 mmol YCl_3, 0.2 mmol $YbCl_3$ and 0.08 mmol $TmCl_3$ were mixed with 6 ml OA and 15 ml ODE in a 50 ml flask. The mixture was slowly heated up to 150 °C under argon flow, and kept isothermally for 30 min to form a clear solution. The solution was cooled down to room temperature, and 5 ml of methanol solution containing 4.0 mmol NH_4F and 2.5 mmol NaOH was added with vigorous stirring for 30 min. Remaining in the argon atmosphere, the mixture was slowly heated up to 110 °C to evaporate methanol and then to 150 °C to evaporate residual water. After that, the solution was heated up to 300 °C in 23 min, and kept at that temperature for another 1.5 h. The reaction was then stopped, and the slurry was cooled down to room temperature. The nanocrystals were washed with cyclohexane/ethanol for four times, and finally re-dispersed in cyclohexane.

Preparation of sample slides. Sample slides carrying individual-distributed UCNPs were carefully prepared. To achieve the best imaging quality, an embedding medium with refractive index matching that of the immersion oil was made first. 2.4 g Mowiol 4-88 (Sigma-Aldrich) was mixed with 6 g glycerol in a 50 ml centrifuge tube. After stirring on a magnetic stirrer for 1 h, 6 ml Milli-Q water was added, and the stirring continued for another 2 h. Then, 12 ml tris(hydroxymethyl)aminomethane (Tris)-HCl buffer (0.2 M, pH 8.5) was added, and the solution was water-bathed at 50 °C under constant agitation until the Mowiol was largely dissolved. Any remaining solids were removed by centrifugation at 7,500g for 30 min.

To prepare a sample slide, a cover slip was washed with pure ethanol and then Milli-Q water under ultrasonication, and then treated with 50 µl polylysine solution (0.1% in H_2O w/v). After 30 min, the polylysine was washed off with Milli-Q water, and the cover slip was air-dried. 20 µl of the UCNPs (diluted to 0.01 mg ml^{-1} in cyclohexane) were dropped onto the treated surface, which was immediately washed with 500 µl cyclohexane twice. After being air-dried, the cover slip was put over a clean glass slide spread with 10 µl as-prepared embedding medium, and any air bubbles were squeezed out by gentle force. The sample was kept at room temperature for another 24 h to ensure complete dryness before measurement.

Analytical interpretation of the photon-avalanche-like process. The photon avalanche (PA) phenomenon was first discovered in 1979 in Pr-doped $LaCl_3$ and $LaBr_3$ crystals[34], followed by reconfirmations in crystals and glasses doped with other lanthanides including Sm^{3+}, Nd^{3+}, Tm^{3+}, Er^{3+} and Ho^{3+} (refs 17, 20, 35). Later in the 90s various models were proposed to interpret the PA process. Two aspects of PA, namely (1) the intrinsic requirement of upconversion material to enable PA, and (2) the pumping condition in order to observe a PA threshold, have been shown with clear mathematical derivation[14–16,36]. These approaches were adopted here to explain the results obtained in this work.

To investigate the underlying cause of enhanced population inversion in highly-doped $NaYF_4$:Yb,Tm upconversion nanocrystals, consider the simplified energy level diagram illustrated in Extended Data Fig. 4a, which involves two energy levels associated with the sensitizer Yb^{3+} ions ($^2F_{7/2}$ and $^2F_{5/2}$, represented as S1 and S2, respectively) and three associated with the emitter Tm^{3+} ions ($^3H_6$, $^3H_5$/$^3F_4$ and $^3F_{2,3}$/$^3H_4$, represented as 1, 2 and 3, respectively). Assuming: (a) the excitation photons are absorbed by Yb^{3+} only; (b) energy transfer happens between Yb^{3+} on the excited level and Tm^{3+} on both the ground and the intermediate levels; (c) cross-relaxation happens between Tm^{3+} on the ground and the upper-excited levels; and (d) other non-radiative relaxation pathways are negligible, the following independent rate equations can be obtained

$$\frac{dn_{S2}}{dt} = Pn_{S1} - W_S n_{S2} - c_1 n_{S2} n_1 - c_2 n_{S2} n_2 \quad (1)$$

$$\frac{dn_1}{dt} = -c_1 n_{S2} n_1 + W_2 n_2 + bW_3 n_3 - kn_1 n_3 \quad (2)$$

$$\frac{dn_3}{dt} = c_2 n_{S2} n_2 - W_3 n_3 - kn_1 n_3 \quad (3)$$

where P is the absorption rate of Yb^{3+} ($P = \sigma\lambda I/hc$, in which λ is the excitation wavelength, I is the excitation intensity at λ, σ is the absorption cross-section of Yb^{3+} at λ, h is the Planck constant, and c is the speed of light); W_S is the intrinsic decay rate of excited Yb^{3+}; c_i is the upconversion coefficient between excited Yb^{3+} and Tm^{3+} on level i; W_i is the intrinsic decay rate of Tm^{3+} on level i; b is the branching ratio for Tm^{3+} decaying from level 3; k is the cross-relaxation coefficient; and n is the population of ions on an energy level satisfying

$$n_{S1} + n_{S2} = 1 \quad (4)$$

$$n_1 + n_2 + n_3 = 1 \quad (5)$$

Let $R_1 = c_1 n_{S2}$, $R_2 = c_2 n_{S2}$, and selecting equations (2), (3) and (5), we have

$$\begin{aligned} \frac{dn_1}{dt} &= -R_1 n_1 + W_2 n_2 + bW_3 n_3 - kn_1 n_3 \\ \frac{dn_3}{dt} &= R_2 n_2 - W_3 n_3 - kn_1 n_3 \\ n_1 + n_2 + n_3 &= 1 \end{aligned} \quad (6)$$

To solve equation (6) at the equilibrium state (that is, $dn_1/dt = dn_3/dt = 0$), eliminating n_1 and n_2 leads to

$$\begin{aligned} &An_3^2 + Bn_3 - R_1R_2 = 0 \\ &A = k(R_2 + W_3 + bW_3 - W_2) \\ &B = kW_2 - kR_2 + bW_3R_2 + R_1R_2 + R_1W_3 + W_2W_3 \end{aligned} \tag{7}$$

Therefore

$$n_3 = \frac{B}{2A}\left[\mathrm{sgn}(B)\left(1 + \frac{4AR_1R_2}{B^2}\right)^{1/2} - 1\right] \tag{8}$$

Note that the other root of the quadratic equation, which is negative, is omitted.

The analytical solution of equations (7) and (8) appears identical to that derived by Joubert *et al.*[14] when they modelled PA in $LiYF_4:Nd^{3+}$, except in their case R_1 and R_2 are constant (due to the sole dopant of Nd^{3+}) whereas here they are proportional to n_{S2}. However, the number of sensitizers in a single nanocrystal is limited; therefore under sufficient excitation intensity, it is reasonable to assume that the population of n_{S2} approaches its asymptotic limit, so that R_1 and R_2 can be treated as constants in equations (7) and (8). This allows the previous analyses to be adopted for the Yb–Tm upconversion system here.

To understand whether the upconversion material is capable of PA (the first aspect of PA mentioned above), assuming $AR_1R_2/B^2 \ll 1$, from equation (8) we have

$$n_3 \approx \begin{cases} R_1R_2/B & \text{when } B > 0 \\ -B/A & \text{when } B < 0 \end{cases} \tag{9}$$

It can be seen that, when $B > 0$, n_3 is inversely proportional to B; therefore any change in B has negligible impact on n_3. When $B < 0$, n_3 becomes proportional to B, so that the change in B will lead to an obvious difference in n_3. This $B < 0$ regime is where PA happens, allowing n_3 to increase dramatically towards population inversion.

According to the expression of B in equation (7), if an upconversion material offers $k < bW_3$, it always gives $B > 0$, therefore PA can never happen. On the other hand, only if $k > bW_3$, both regimes may exist for the material, and PA starts when B transits from positive to negative. The requirement of $k > bW_3$ is thus the precondition for PA.

This intrinsic requirement can be viewed in another way, illustrated first by Auzel and Chen[16]. For equation (6), at the beginning of the photon upconversion process, one can assume $n_1 \approx 1$. Therefore at the equilibrium state,

$$\begin{aligned} &-R_1 + W_2n_2 + bW_3n_3 - kn_3 = 0 \\ &R_2n_2 - W_3n_3 - kn_3 = 0 \end{aligned} \tag{10}$$

Equation (10) can be rewritten as

$$\begin{aligned} n_2 &= \frac{R_1}{W_2} + \frac{k - bW_3}{W_2}n_3 \\ n_3 &= \frac{R_2}{W_3 + k}n_2 \end{aligned} \tag{11}$$

Equation (11) can be translated as the block diagram shown in Extended Data Fig. 4b, which corresponds to a typical feedback system. It is explicit that $k > bW_3$ represents positive feedback, while $k < bW_3$ gives negative feedback. Thus, the precondition of an upconversion material for PA essentially means the cross-relaxation intensifies to a point that it begins to enhance rather than quench the populations of the excited levels.

Now we come to the second aspect of PA mentioned above, namely, the PA threshold. First, let $R_1 = 0$ in equation (7), then we have

$$\begin{aligned} &An_3^2 + B'n_3 = 0 \\ &A = k(R_2 + W_3 + bW_3 - W_2) \\ &B' = kW_2 - kR_2 + bW_3R_2 + W_2W_3 \end{aligned} \tag{12}$$

Therefore,

$$n_3 = \max\,[0, -B'/A] \tag{13}$$

Hence, the condition for n_3 to be a positive value is

$$-\frac{B'}{A} = \frac{(k - bW_3)R_2 - kW_2 - W_2W_3}{k(R_2 + W_3 + bW_3 - W_2)} > 0 \tag{14}$$

Since $k > bW_3$, this leads to the pumping threshold for PA

$$R_{2,\mathrm{th}} = \frac{(k + W_2)W_2}{k - bW_3} \tag{15}$$

So that for $R_2 \le R_{2,\mathrm{th}}$, $n_3 = 0$. Since the value of zero cannot be plotted on a log–log scale when we plot n_3 against R_2, the PA threshold is therefore distinct for the case of zero ground-level absorption[36].

When $R_1 > 0$, clear observation of the PA threshold depends on the deviation of n_3 from that in the case of zero ground-level absorption. This can be semi-quantified by the values of n_3 at the threshold $R_{2,\mathrm{th}}$. For $R_1 = 0$, $n_3(R_{2,\mathrm{th}}) = 0$; whereas for $R_1 > 0$, note that at $R_{2,\mathrm{th}}$ we have $B = R_1R_2 + R_1W_3$, and equation (8) becomes

$$\begin{aligned} n_3(R_{2,\mathrm{th}}) &= \frac{\sqrt{B^2 + 4AR_1R_2} - B}{2A} \\ &= \frac{\sqrt{(R_1R_2 + R_1W_3)^2 + 4R_1R_2k(R_2 + W_3 + bW_3 - W_2)} - (R_1R_2 + R_1W_3)}{2k(R_2 + W_3 + bW_3 - W_2)} \end{aligned} \tag{16}$$

Combining equations (15) and (16), $n_3(R_{2,\mathrm{th}})$ can be solved as

$$n_3(R_{2,\mathrm{th}}) = \frac{\left[\sqrt{1 + \frac{4kW_2W_3(1+b)(k - bW_3 + W_2)(k + W_3)}{(kW_2 + kW_3 + W_2W_3 - bW_3^2)^2}R_1} - 1\right]}{2kW_3(1+b)(k - bW_3 + W_2)} \tag{17}$$

Taking a first-order approximation, we have

$$\begin{aligned} n_3(R_{2,\mathrm{th}}) &\approx \frac{(k + W_3)W_2}{kW_2 + kW_3 + W_2W_3 - bW_3^2}R_1 \\ &= \frac{(k + W_3)W_2}{(k + W_3)W_2 + (k - bW_3)W_3}R_1 \end{aligned} \tag{18}$$

Therefore, n_3 will be close to zero at the threshold only if R_1 is very small, so that the threshold will distinctly appear. This aspect of PA, first explained by Goldner and Pellé in the context of laser action[36], indicates that non-resonant ground-level absorption is necessary for the threshold to be observed. In the same paper, they further revealed that resonant pumping for the ground level can give a higher population in the upper level and thus favour laser action.

Combining the two aspects of PA mentioned above, we find that, while observation of threshold behaviour provides sufficient experimental evidence for the positive feedback in PA, an upconversion material capable of such PA-like positive feedback does not necessarily show the threshold, unless under the condition of non-resonant ground-level absorption. In particular, for co-doped upconversion materials containing sensitizers and emitters, the ground-level absorption typically has a similar magnitude to the excited-level absorption (as both are via energy transfer from the sensitizers), so that a threshold is rarely observed.

Using the rate equations and parameters reported for $LiYF_4:Nd$[14], the numerical simulation results drawn as Extended Data Fig. 4c show similar behaviour of the excited-level populations when the pumping rate exceeds the threshold value, regardless of the presence/absence of the actual threshold (the latter case is simulated by fixing $\beta = R_1/R_2 = 1$ to represent resonant ground-level absorption). Similarly, using the model and parameters we find for our $NaYF_4$:Yb,Tm UCNPs, the threshold can be determined from the simulation by setting the ground-level upconversion coefficient far smaller than the excited-level upconversion coefficients (we chose $c_1 = 1$), as shown in Extended Data Fig. 5d. The behaviour of the excited-level populations again appears very similar when the pumping rate exceeds the threshold value, regardless of the presence/absence of the virtual threshold.

Numerical simulation of the Yb–Tm upconversion system. Assuming rapid non-radiative decays for $^3H_5 \rightarrow {}^3F_4$ and $^3F_{2,3} \rightarrow {}^3H_4$, and thus each pair being combined into one level, the energy level diagram of the Yb–Tm upconversion system in Fig. 3a is redrawn as Extended Data Fig. 5a, with rate parameters labelled on each pathway. The following model of rate equations is established

$$\begin{aligned} \frac{dn_{S2}}{dt} &= P_{980}n_{S1} - W_5n_{S2} - (c_1n_1 + c_2n_2 + c_3n_3 + c_4n_4)n_{S2} \\ \frac{dn_2}{dt} &= c_1n_{S2}n_1 - c_2n_{S2}n_2 - W_2n_2 + b_{32}W_3n_3 + b_{42}W_4n_4 \\ &\quad + b_{52}W_5n_5 + 2k_{31}n_1n_3 + k_{41}n_1n_4 \end{aligned}$$

$$\begin{aligned}\frac{dn_3}{dt} &= P_{808}(n_1 - n_3) + c_2 n_{S2} n_2 - c_3 n_{S2} n_3 - W_3 n_3 + b_{43} W_4 n_4 \\ &\quad + b_{53} W_5 n_5 - k_{31} n_1 n_3 + k_{41} n_1 n_4 + 2k_{51} n_1 n_5 \\ \frac{dn_4}{dt} &= c_3 n_{S2} n_3 - c_4 n_{S2} n_4 - W_4 n_4 + b_{54} W_5 n_5 - k_{41} n_1 n_4 \\ \frac{dn_5}{dt} &= c_4 n_{S2} n_4 - W_5 n_5 - k_{51} n_1 n_5\end{aligned} \tag{19}$$

where P_{980} is the absorption rate of Yb^{3+}; P_{808} is the absorption/stimulated emission rate of Tm^{3+} (so that the term of $P_{808}(n_1 - n_3)$ introduced into dn_3/dt represents the net effect of absorption and stimulated emission); W_5 is the intrinsic decay rate of excited Yb^{3+}; c_i is the upconversion coefficient between excited Yb^{3+} and Tm^{3+} on level i; W_i is the intrinsic decay rate of Tm^{3+} on level i; b_{ij} is the branching ratio for Tm^{3+} decaying from level i to level j satisfying $\sum_{j=1}^{i-1} b_{ij} = 1$; k_{ij} is the cross-relaxation coefficient between Tm^{3+} on level i and level j; and n is the population of ions on an energy level satisfying

$$\begin{aligned}n_{S1} + n_{S2} &= 1 \\ n_1 + n_2 + n_3 + n_4 + n_5 &= 1\end{aligned} \tag{20}$$

We use this rate-equations model of equations (19) and (20) to fit the transient response obtained from the 8% Tm-doped UCNPs under dual-laser excitation. The rate parameters yielded are summarized in Extended Data Fig. 5b, and the simulation results are plotted in Extended Data Fig. 5c, showing good consistency with the measurements.

The cross-relaxation coefficients are found to be orders of magnitude larger than the decay rates as well as the upconversion coefficients. In particular, it is seen that the precondition for PA for the lowest three energy levels (that is, $k_{31} > b_{31}W_3$) has been satisfied; whereas if k_{31} is reduced quadratically with the doping concentration, for 1% Tm-doped nanocrystals we have $k_{31}' = 2.3 \times 10^3$, so that $k_{31}' < b_{31}W_3$. These support the assertion that intense cross-relaxation in the PA-like process plays the key role in enhancing population inversion.

It should be noted that the modelling conducted here does not address all of the processes in the Yb–Tm upconversion system. On the one hand, Extended Data Fig. 2 indicates that both the blue peak at 480 nm and the red peak at 650 nm become negligible for high Tm^{3+} doping concentrations, suggesting substantial cross-relaxation involving the $^1G_4$ level. This may well include $(n_4, n_2) \rightarrow (n_3, n_3)$, $(n_4, n_3)/(n_3, n_4) \rightarrow (n_2, n_5)$ and $(n_4, n_4) \rightarrow (n_3, n_5)$, in addition to the sole $(n_4, n_1) \rightarrow (n_3, n_2)/(n_2, n_3)$ cross-relaxation process involving n_4 that has been considered in the rate equations of equation (19). On the other hand, our current system is not able to characterize Tm^{3+} emission bands outside the visible range, such as the one-photon emission at 1.8 μm and the five-photon emission at 350 nm. Nevertheless, the current modelling provides results reasonably close to the experimental data, which we believe is suited for illustrating the physical picture and forming a stepping stone for more precise investigation in the future.

Sample size. No statistical methods were used to predetermine sample size.

Data availability. The data that support the findings of this study are available from the corresponding authors upon reasonable request.

34. Chivian, J. S., Case, W. E. & Eden, D. D. The photon avalanche: a new phenomenon in Pr^{3+}-based infrared quantum counters. *Appl. Phys. Lett.* **35,** 124–125 (1979).
35. Joubert, M. F. Photon avalanche upconversion in rare earth laser materials. *Opt. Mater.* **11,** 181–203 (1999).
36. Goldner, P. & Pelle, F. Photon avalanche fluorescence and lasers. *Opt. Mater.* **5,** 239–249 (1996).

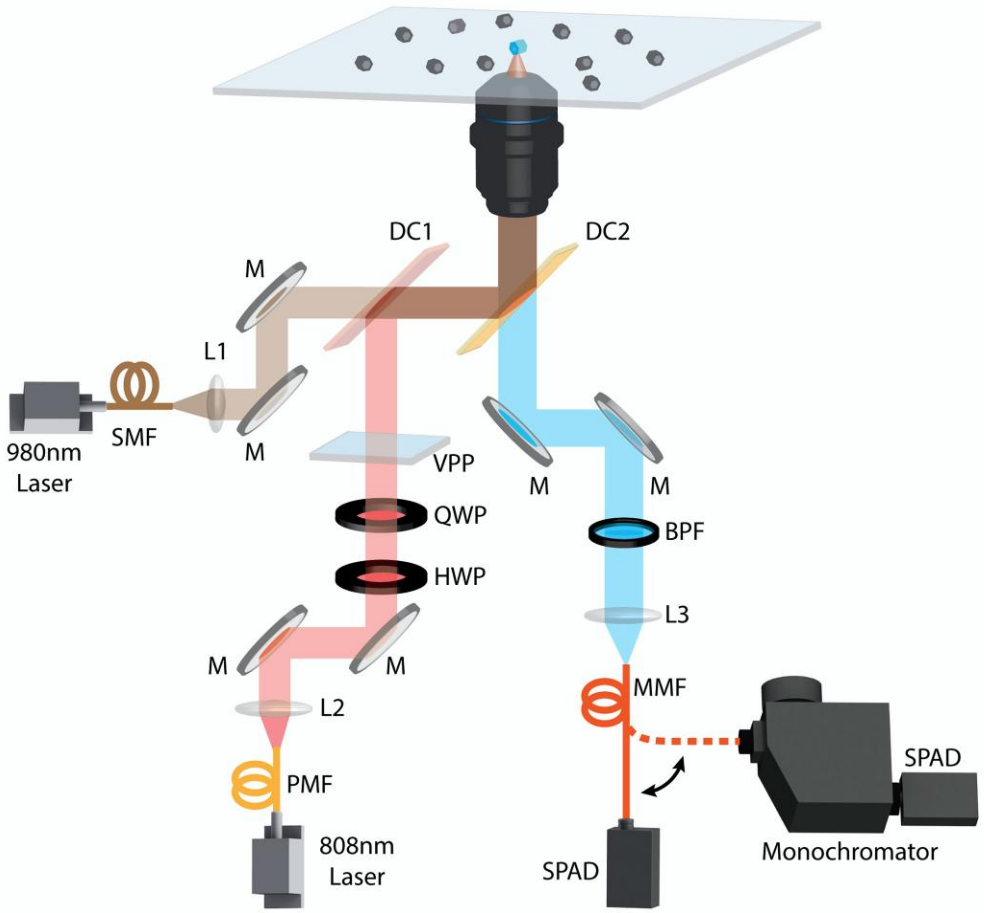

Extended Data Figure 1 | Optical layout of the dual-laser confocal/super-resolution microscope for probing $NaYF_4$:Yb,Tm nanocrystals. SMF, single-mode fibre; PMF, polarization-maintaining fibre; MMF, multi-mode fibre; DC1 and DC2, dichroic filters; L1, L2 and L3, collimation/collection lenses; HWP, half-wave plate; QWP, quarter-wave plate; VPP, vortex phase plate; SPAD, single-photon avalanche diode; M, mirror.

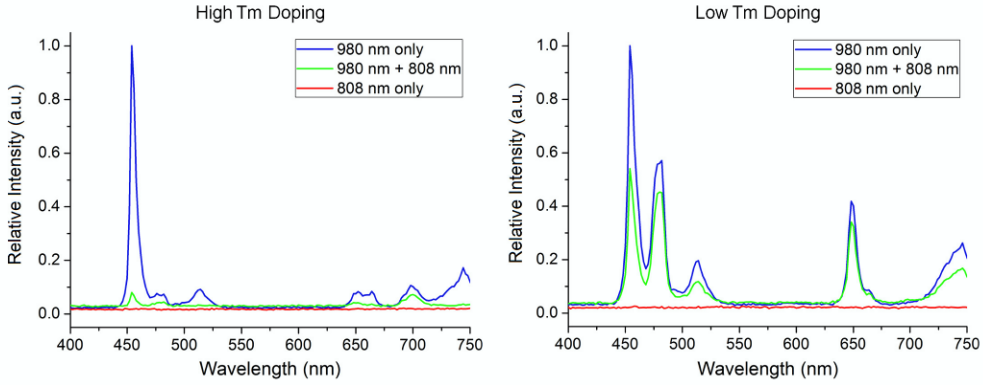

Extended Data Figure 2 | Upconversion emission spectra of 8% (left) and 1% (right) Tm-doped UCNPs. The 980 nm and 808 nm laser powers measured at the objective back aperture were 1 and 10 mW, respectively.

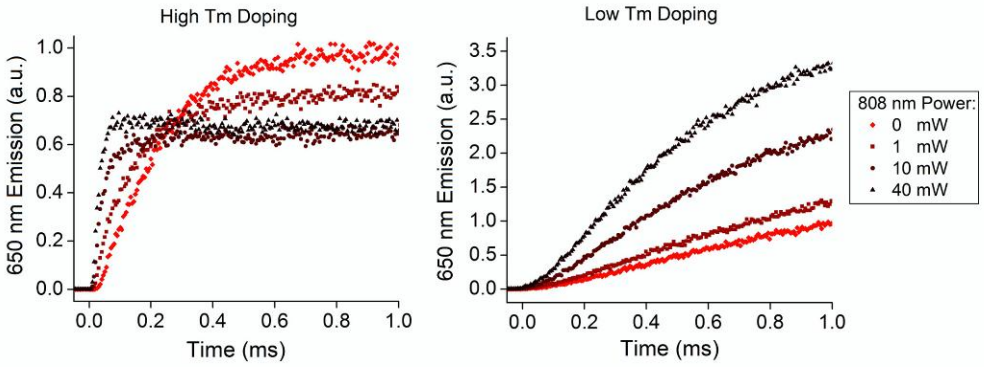

Extended Data Figure 3 | Transient responses of 650 nm upconversion emission under synchronous 980 nm and 808 nm pulses. Left, 8% Tm-doped UCNPs; right, 1% Tm-doped UCNPs. The 980 nm laser power was fixed at 1 mW, while the 808 nm laser power was varied from 0 to 40 mW (both measured at the objective back aperture).

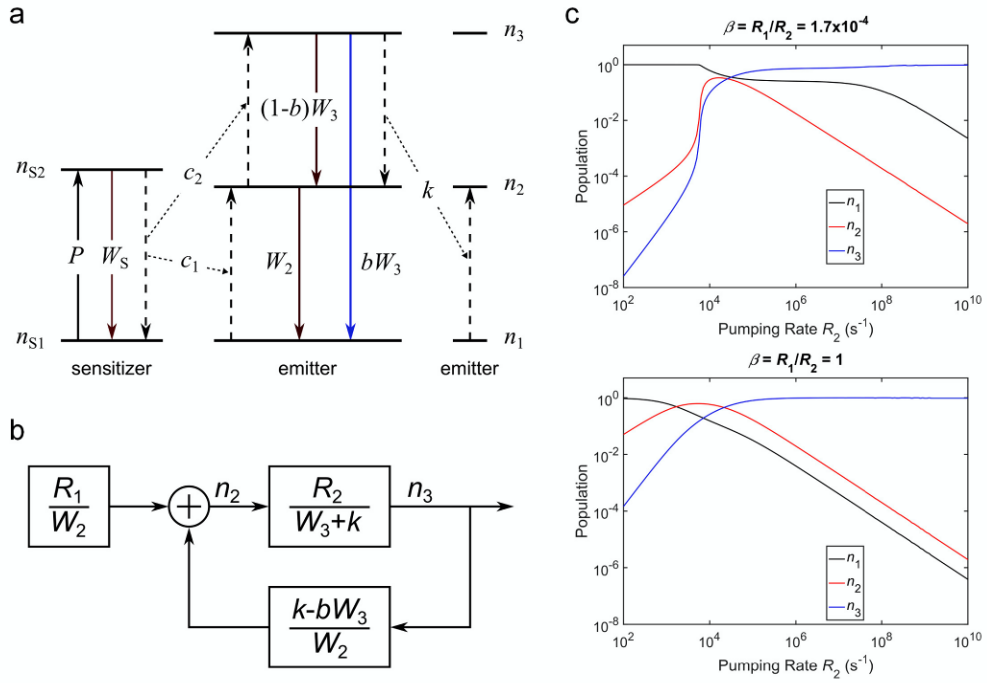

Extended Data Figure 4 | Modelling of the photon-avalanche-like process in upconversion materials. a, Simplified three-level energy diagram of an upconversion system containing sensitizers and emitters. **b**, Block diagram illustrating photon avalanche as a feedback process, with its type (positive or negative) determined by the sign of $(k - bW_3)$. **c**, Numerical simulation of the emitter populations based on the rate parameters reported previously[14]. Comparison between non-resonant ground-level pumping (top) and resonant ground-level pumping (bottom) shows that the threshold occurs only if non-resonant ground-level pumping is employed. See Methods for details.

a

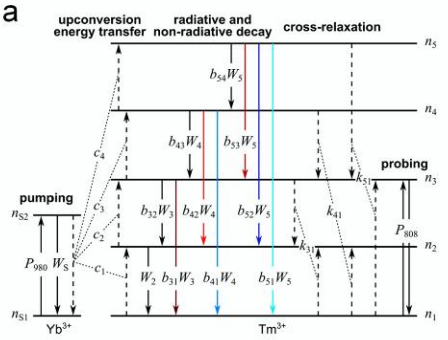

b

absorption rates (s^{-1})		decay rates (s^{-1})				
P_{980}	P_{808}	W_S	W_2	W_3	W_4	W_5
2.75×10^4	7.4×10^5	7.6×10^3	6.4×10^3	1.8×10^4	1.4×10^4	3.2×10^3

upconversion coefficients				cross-relaxation coefficients		
c_1	c_2	c_3	c_4	k_{31}	k_{41}	k_{51}
6.23×10^4	5.7×10^4	7.4×10^4	5.2×10^3	1.5×10^5	1.75×10^5	4.8×10^5

branching ratios								
b_{31}	b_{32}	b_{41}	b_{42}	b_{43}	b_{51}	b_{52}	b_{53}	b_{54}
0.27	0.73	0.18	0.24	0.58	0.24	0.23	0.20	0.33

c

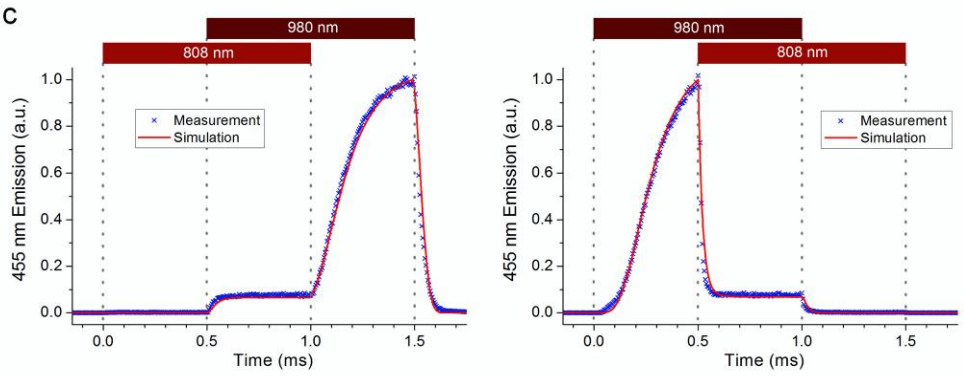

d

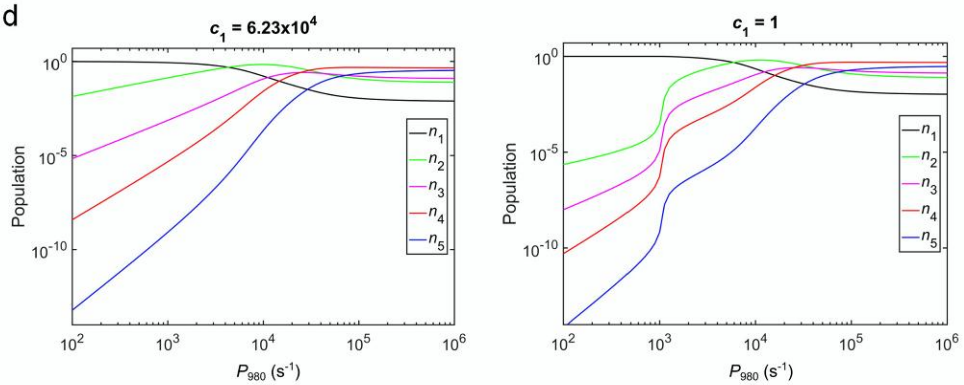

Extended Data Figure 5 | Simulation of the Yb–Tm upconversion system. a, Energy level diagram used for rate equation modelling. **b**, Rate parameters simulated for the 8% Tm-doped UCNPs. **c**, Comparison between the simulation and the experimental results for the 8% Tm-doped UCNPs under dual-laser excitation with different pulse sequences (left and right). **d**, Numerical simulation of the emitter populations under 980 nm pumping only, using the obtained c_1 value (left), and by artificially setting $c_1 = 1$ to reveal the threshold (right). Details of rate equation modelling are given in Methods.

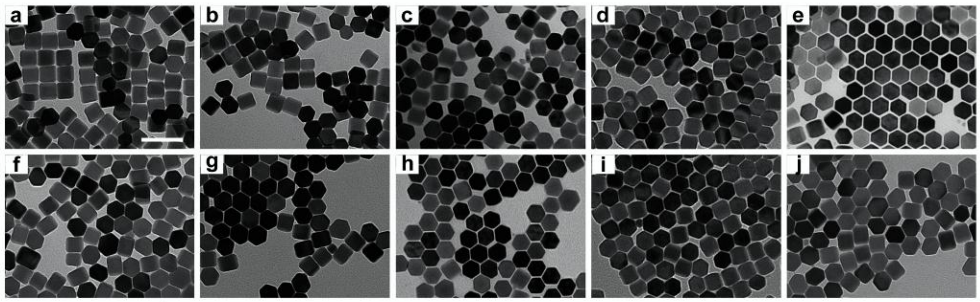

Extended Data Figure 6 | TEM images of the $NaYF_4$:Yb,Tm nanocrystals. The Yb doping concentration was fixed at 20 mol%, and **a**–**j**, the Tm doping concentrations are respectively 0.5, 1, 1.5, 2, 2.5, 3, 3.5, 4, 6 and 8 mol%. All nanocrystals have average sizes around 40 nm. Scale bar, 100 nm.

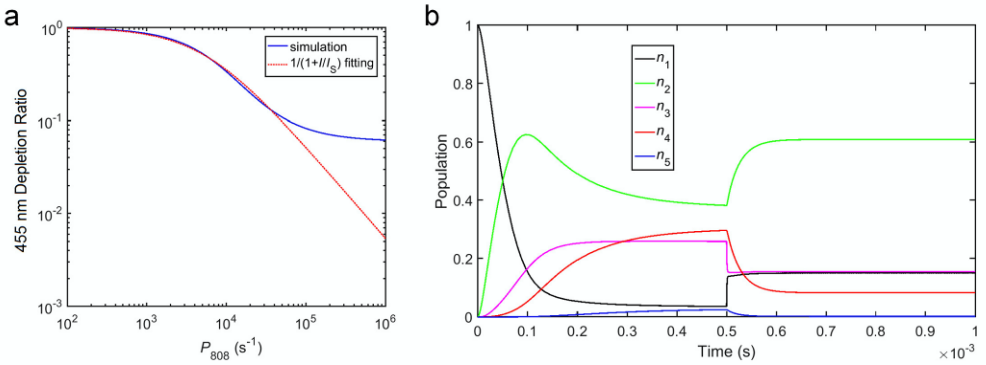

Extended Data Figure 7 | Simulation of the optical switching at 455 nm for 8% Tm-doped UCNPs. a, The 455 nm depletion ratio as a function of the 808 nm probing rate, which is simulated using the rate parameters listed in Extended Data Fig. 5b. The curve fits well to $1/(1+I/I_S)$ except for the high power range. **b**, Emitter populations as a function of time, again simulated using the rate parameters listed in Extended Data Fig. 5b. The 980 nm pumping is turned on at time = 0 s, while the 808 nm probing is turned on at time = 0.5 ms. Note the overlap between n_1 ($^3H_6$ ground level) and n_3 ($^3H_4$ intermediate level) once the 808 nm probing is turned on.

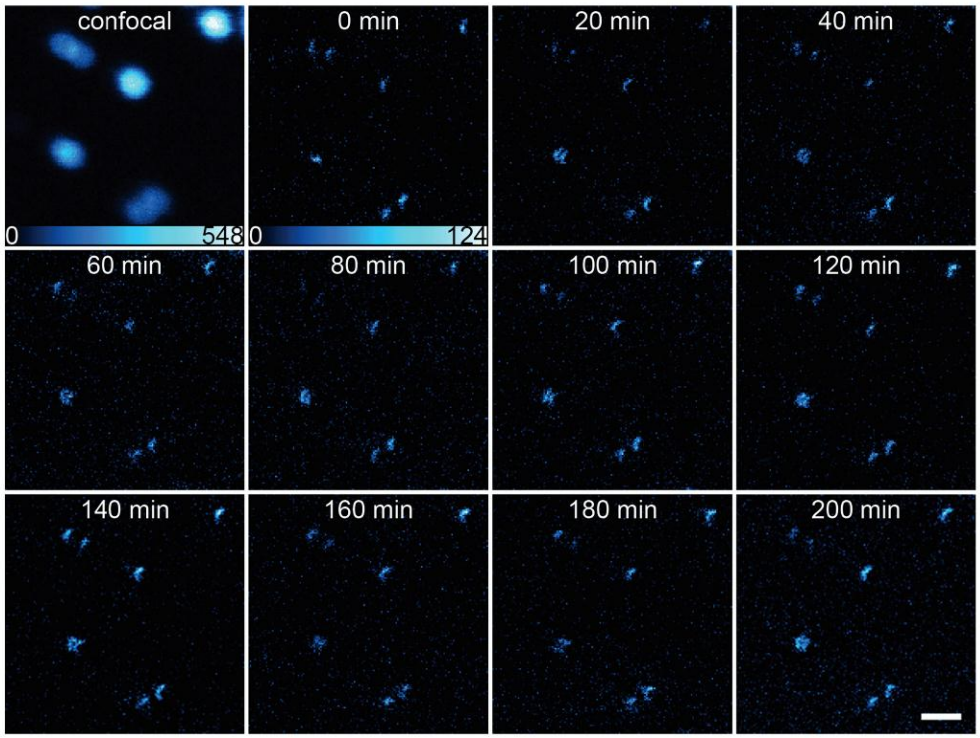

Extended Data Figure 8 | Time-series upconversion-STED images recorded for the same sample area under continuous laser excitation and scanning. The sample slide contains 40-nm UCNPs with 8% Tm and 20% Yb. The 455 nm upconversion emission photon count is colour coded. The 980 and 808 nm laser powers at the objective back aperture were 1 and 30 mW, respectively. The scan step is 20 nm and the pixel dwell time is 4 ms. Scale bar, 500 nm.

4.3 Remarks

We show that at high Tm^{3+} doping concentration, the cross-relaxation rates between Tm^{3+} emitters can increase sufficiently, efficiently establishing population inversion on their intermediate energy levels to the ground level. This largely reduces the intensity requirement for stimulated emission depletion, which is not achievable using conventional upconversion nanocrystals with low doping concentration. The depletion intensity was reduced by two orders of magnitude using 8% Tm^{3+} doped samples. This provides immediate opportunity for live cell super-resolution imaging upon robust biofunctionalisation of upconversion nanocrystals.

In principal, with CW excitation and depletion, the long lifetime does not affect the pixel dwell time. So the CW STED system could achieve real-time imaging speed with the upconversion nanocrystals no matter the milli- or microsecond lifetime. The millisecond level pixel dwell time used in our work is actually due to the brightness limitation on single nanocrystal. As discussed in the paper, "New crystal design and synthesis that will allow UCNPs with Tm doping concentration beyond 8% need to be explored, which will both enhance the brightness and shorten the lifetime of the upconversion luminescence, thereby shortening pixel dwell time".

As for most reported PALM and STORM systems, the acquisition time is still no less than tens of seconds level. The SIM has been reported to achieve video rate in 2009 by Gustafsson's team (*Nature Methods* 6, 339 - 342 (2009)), while the resolution in no higher than 100 nm. For PALM, STORM or SSIM, it requires at least three orders of magnitude of frames to achieve sub-100 nm resolution in one image, thus for video rate imaging these technologies need ultrafast camera like sCMOS camera and extremely optimized algorithm, which is also need to balance with the pixel numbers. A few groups has been trying to achieve the goal while no solid results are made fulfilling all conditions especially considering the low signal-to-noise ratio when fast imaging which typically causes extra artificial structure after PSF-fitting. As for STED, the speed limitation is mainly on scanning method which could be adapted from confocal ones. The different scanning method in confocal microscopy has been proved to achieve video rate easily, and with some method like multi focus the rate can be high than 1000 fps. In general, STED shows much more potential in real time imaging.

Chapter 5: Conclusions and Perspectives

5.1 Thesis Summary

Among the new generation of optical nanoscopy techniques, STED is the first and optically most straightforward method capable of 3-D super-resolution imaging potentially at video rate. However the extreme depletion intensity requirement of STED makes it challenging for live cell imaging. This thesis endeavours to overcome this challenge through a range of new developments of both the instrumentation and the luminescent probe aspects. In particular, we found that highly doped upconversion nanocrystalsa allow efficient depletion of their luminescence through amplified stimulated emission from their intermediate excited levels, which suggests a viable avenue to low-power biological-friendly STED super-resolution imaging. The key findings of the research reported here are:

1) A continuous wave STED (CW STED) microscopy based on a Ti:Sapphire oscillator was established, to provide wavelength tenability that allows optimisation of the depletion efficiency on conventional fluorescent dyes. The super resolution of ~71nm was achieved on 20 nm fluorescent nanoparticles. Three components of cytoskeletons and RNA were imaged in fixed cells with the CW STED super-resolution system. The results show that the synchronisation-free CW mode can reduce the system complexity and cost. However, the extreme intensity condition to achieve resolution enhancement cannot be alleviated through pure instrumentation.

2) Theoretical studies and numerical simulation of STED in fluorescent materials were conducted, with an effective model established to describe the stimulated emission depletion process in a simplified four-level system. The populations of the excited levels were monitored when varying the luminescence lifetime and excited-level cross-section in the simulation. It can be shown that for luminescent probes with long lifetime, the depletion power requirement can be largely reduced in principle.

3) Low-power STED-like super-resolution imaging was achieved using $NaYF_4$:Yb^{3+}/Tm^{3+} upconversion nanocrystals, based on a novel scheme that depletes an intermediate state to inhibit further upconverted emission. A variety of factors were investigated, showing that the doping concentration plays a critical role in effective depletion by this new scheme. For highly doped nanocrystals, the saturation intensity can be reduced by two orders of magnitude compared to conventional upconversion nanocrystals with low doping concentration. Super-resolution imaging of the highly doped nanocrystals was achieved, with sub-50 nm resolution using much lower depletion intensity in CW mode.

4) The physical mechanism for achieving the low power upconversion-STED operation using highly doped upconversion nanocrystals was thoroughly studied. A photon-avalanche-like effect, that is the strong inter-emitter cross-relaxation inside the photon upconversion system leading to population inversion between the intermediate energy levels to the ground level, was proved to be the key to the substantially reduced intensity requirement.

This thesis also suggests that, apart from advances in optical instrumentation, new nanophotonic probes are indispensable for pushing optical super-resolution techniques beyond their current scope. Collaborative approaches are becoming increasingly important to facilitate cross-disciplinary research and development, which may hold the key to unprecedented nanophotonic technologies for life sciences in future.

5.2 Future Directions

The fruitful results of this multidisciplinary research program suggest a broad range of opportunities in both conceptual advancement and engineering excellence. Three immediate opportunities have been identified, as follows:

Firstly, the depletion power requirement may be further reduced using the time-gating technique, which was previously the most effective approach to lower the power requirement for STED before our usage of upconversion nanocrystals. Up to one order of magnitude reduction was demonstrated on conventional fluorescent dyes by the previous time-gating STED (G-STED) method, which, however, is challenging to achieve due to the

strict temporal resolution needed for fluorescent lifetimes on the nanosecond scale. By contrast, upconversion nanoparticles provide micro- to milli-second luminescence lifetimes that are technically ideal for G-STED operation, which can also largely suppress the background noise arising from re-excitation of the probes, residual scattering of the excitation light, and/or biological autofluorescence.

Secondly, the upconversion-STED method demonstrated on Tm^{3+} doped nanocrystals is readily applicable to upconversion nanoparticles doped with other lanthanide emitters, such as Er^{3+} and Ho^{3+}. Like Tm^{3+}, they also have ladder-like levels with abundant transition pathways of similar energy, therefore intense cross-relaxation can easily happen once the doping concentration is sufficient, resulting in possible photon avalanche or photon-avalanche-like process to establish population inversion efficiently for low-power super-resolution imaging. Furthermore, in principle, the mechanism is not restricted for upconversion system but is potentially applicable to down-conversion lanthanide probes as well. Indeed, the first report of the photon avalanche phenomenon is on Pr^{3+}-based down-conversion system[1]. If suitable depletion scheme can be designed for down-conversion lanthanide probes, such as Eu^{3+} and Tb^{3+} complexes that can be easily modified to target biomolecules specifically, this will further broaden the scope of the STED-like method in biological application.

Finally, the newly demonstrated multiplexing capability using lanthanide nanocrystals with tunable luminescence lifetimes may be integrated, to further enhance the analytical throughput of the upconversion-STED method for simultaneous visualisation of multiple types of target biomolecules at super resolution. Using a combination of strategies, including varied doping concentrations, it has become practical to realise ten or more lifetime channels in a single colour band, which can either substitute the conventional spectra-based multiplexing at significantly reduced system complexity and cost, or build on top of the spectral channels to achieve high-dimension multiplexing capacity. Both of these will be extremely appealing to end users in biology and medicine. Preliminary experiments along this direction have been carried out during my PhD candidature, which are summarised in the next section.

5.3 Towards lifetime-based multiplexing super-resolution imaging – the preliminary results

Today all the optical super-resolution microscopy relies on fluorescent labelling, either specific or not, to disclose the morphologic and/or the locational information of biomolecules and subcellular components. However, since biological activities typically involve multiple types of targets, it remains virtually impossible to reveal their complicated interactions using conventional fluorescent probes, due to the fundamental challenge of spectral overlapping. Additionally, the use of multiple fluorescent wavelengths requires sophisticated system design, for example, for STED microscopy, to add different depletion wavelengths according to the chosen probes. This will increase the difficulty for alignment as well as instrumentation cost substantially, representing significant roadblocks to practical applications.

Time-domain multiplexing based on different decay lifetimes has been proposed to complement the spectral-domain multiplexing. However, lifetimes of conventional fluorescent probes are in the nanosecond range, which provides limited multiplexing capacity and is prone to autofluorescence interference. And sophisticated methods and instrumentation, mainly time-correlated single photon counting (TCSPC), is required to measure such short lifetimes.

Recently, our group proposed to overcome these challenges by using tunable luminescence lifetimes in the microsecond-to-nanosecond range based on lanthanide probes such as upconversion nanocrystals. We investigated the potential mechanisms for lifetime tuning in upconversion nanocrystals, and employed them for multiplexed confocal imaging, presenting a stepping stone for lifetime-multiplexed upconversion-STED technique in the future. The preliminary results are shown in Appendix II.

5.4 Future challenges for upconversion nanocrystals in live cell imaging

Upconversion nanocrystals hold promise as novel luminescent probes for numerous applications in nano-biophotonics, like immunoassays, bioimaging, and targeted drug delivery as carriers[2-7]. These applications of upconversion nanocrystals have been motivated by their attractive optical properties of excellent photostability, narrowband photoluminescence, efficient anti-Stokes emission and long luminescence lifetimes, which are needed to meet the requirements of multiplexed and background free detection at prolonged observation times. Therefore, upconversion nanocrystals may become new contrast agents for imaging with potential to enable biomedical research and guide clinical decisions. And the low power feature showed in this thesis would largely benefit the broadly use for upconversion nanocrystals in super-resolution imaging.

Although exhibiting promising features and application prospects, the use of upconversion nanocrystals is limited by the lack of robust bioconjugation protocols. Upconversion nanocrystals are typically synthesized in the presence of organic solvents, as capping ligands that control nanocrystal growth and stabilize them against aggregation, but form the hydrophobic surface. On the other hand, for most biological applications, additional surface modification of upconversion nanocrystals is necessary to render a hydrophilic functional surface so that the nanocrystals become soluble in aqueous solution for biological applications. Especially considering the non-free permeation size of the upconversion nanocrystals, surface modification is necessary for most cases.

Currently two major protocols are mainly adapted in surface modification for delivery of upconversion nanocrystals to live cells and biological systems[17]. One is based on silanization, and the other is based on hydrophobic-hydrophobic interaction, respectively.

In the silanization protocol, biocompatible silica can form shells around the nanocrystal core by hydrolysis of tetraethyl orthosilicate (TEOS). For most hydrophobic upconversion nanocrystals that are synthesized in organic solvents and capped by the hydrophobic ligands (e.g. oleic acid (OA) and oleylamine (OM)), the reverse microemulsion method is commonly used to functionalize the upconversion nanocrystals. Nowadays, the well-known silica chemistry allows precise control of silica growth resulting in tunable thickness. Alternatively, the hydrophilic upconversion nanocrystals can also be coated by silica shells using the *Stöber* method but this is more suitable for large cores with thicker silica layers. In general, silica-coated UCNPs have advantages in adapting existing

protocols for bioconjugation to targeted biomolecules though the additional silica layer increases the size. Furthermore, as another advantage, the porosity of silica shells can be easily controlled, facilitating the production of multifunctional nanocrystals by encapsulating the dyes, magnetic agents, or drugs [8-11]. For this method, the optimization for the amount and ratios of the used reagents, such as upconversion nanocrystals, linker, and antibody as well as the appropriate binding and washing buffers, is quite tricky and need to be further developed otherwise one could easily observed the generation of aggregates during centrifugal washing of unbound antibodies off upconversion nanocrystals.

In the hydrophobic-hydrophobic interaction, the conversion from hydrophobic to hydrophilic surface is based on the adsorption of an amphiphilic polymer onto the hydrophobic surface of nanocrystals to form a double layer of ligands. In this approach, the hydrophobic segment of amphiphilic polymer interacts with the hydrocarbon chain of the original surface ligands (e.g. OA or OM), so that the hydrophilic end points outwards aqueous phase. Typically, the amphiphilic polymers, such as poly(ethyleneglycol) (PEG)-phospholipids [12], OA-polyacrylic acid (PAA)-PEG [13], and poly(maleic anhydride-alt-1-octadecene) (PMAO) [14] are frequently used. Following the same principle, cyclodextrin (e.g. α-CD or β-CD) has been reported to be able to self-assemble onto OA capped UCNPs through a hydrophobic-hydrophobic interaction[15,16]. This amphiphilic strategy is popular since it reacts rapidly under mild conditions after stirring for a short time without laborious post-treatment procedures. However, for this method, the long hydrocarbon chains could usually result in crosstalk conjugation between any two nanoparticles.

Besides the further optimization of the surface medication protocols, the concern about the toxicity of upconversion nanocrystals is still an issue for both *in vivo* and *in vitro* applications. Similar to other chemicals or pharmaceuticals, for upconversion nanocrystals, the potentially harmful effects may originate not only from their chemical composition but also from their small size. The latter property enables the nanoparticles to bypass the biological barriers, thus allowing deep tissue penetration and the accumulation of the nanoparticles in a number of organs. In addition, nanoparticles are known to possess high surface chemical reactivity as well as a large surface-to-volume ratio, which may seriously affect their biocompatibility. As reported recently, OA-capped and silica-coated UCNPs

displayed a significant cytotoxicity (at 50-100ug/mL concentrations), leading to 20-30% reduction in cell viability after 24 hrs' exposure to UCNPs. In contrast, OA-free, DNA-modified or PEGCOOH functionalized UCNPs displayed minimal cytotoxicity (<10% reduction in cell viability) under the same conditions[17]. Notwithstanding the number of studies and existing government reports, knowledge on the general impact of engineered nanomaterials on human health is not well established, and thus risk assessment studies and more studies on hazard and exposure are required[18].

Reference

1 Kolesov R, Reuter R, Xia K et al. Super-resolution upconversion microscopy of praseodymium-doped yttrium aluminum garnet nanoparticles. Physical Review B 2011, 84, 153413.

2 Liu Q, Sun Y, Yang TS et al. Sub-10 nm Hexagonal Lanthanide-Doped NaLuF4 Upconversion Nanocrystals for Sensitive Bioimaging in Vivo. Journal of the American Chemical Society 2011, 133, 17122-17125.

3 Nyk M, Kumar R, Ohulchanskyy TY et al. High Contrast in Vitro and in Vivo Photoluminescence Bioimaging Using Near Infrared to Near Infrared Up-Conversion in TM3+ and Yb3+ Doped Fluoride Nanophosphors. Nano Letters 2008, 8, 3834-3838.

4 Wang Z, Liu CH, Chang LJ et al. One-pot synthesis of water-soluble and carboxyl-functionalized beta-NaYF4:Yb,Er(Tm) upconversion nanocrystals and their application for bioimaging. Journal of Materials Chemistry 2012, 22, 12186-12192.

5 Wang C, Cheng LA, Liu ZA. Drug delivery with upconversion nanoparticles for multi-functional targeted cancer cell imaging and therapy. Biomaterials 2011, 32, 1110-1120.

6 Liu JA, Bu WB, Pan LM et al. NIR-Triggered Anticancer Drug Delivery by Upconverting Nanoparticles with Integrated Azobenzene-Modified Mesoporous Silica. Angewandte Chemie-International Edition 2013, 52, 4375-4379.

7 Dong L, An D, Gong M et al. PEGylated Upconverting Luminescent Hollow Nanospheres for Drug Delivery and In Vivo Imaging. Small 2013, n/a-n/a.

8 Lee JE, Lee N, Kim H et al. Uniform Mesoporous Dye-Doped Silica Nanoparticles Decorated with Multiple Magnetite Nanocrystals for Simultaneous Enhanced Magnetic

Resonance Imaging, Fluorescence Imaging, and Drug Delivery. Journal of the American Chemical Society 2010, 132, 552-557.

9 Tsai CP, Hung Y, Chou YH et al. High-contrast paramagnetic fluorescent mesoporous silica nanorods as a multifunctional cell-imaging probe. Small 2008, 4, 186-191.

10 Kim T, Momin E, Choi J et al. Mesoporous Silica-Coated Hollow Manganese Oxide Nanoparticles as Positive T-1 Contrast Agents for Labeling and MRI Tracking of Adipose-Derived Mesenchyrnal Stem Cells. Journal of the American Chemical Society 2011, 133, 2955-2961.

11 Liong M, Lu J, Kovochich M et al. Multifunctional inorganic nanoparticles for imaging, targeting, and drug delivery. Acs Nano 2008, 2, 889-896.

12 Li LL, Zhang R, Yin L et al. Biomimetic surface engineering of lanthanide-doped upconversion nanoparticles as versatile bioprobes. Angew Chem Int Ed Engl 2012, 51, 6121-6125.

13 Cheng LA, Yang K, Zhang SA et al. Highly-Sensitive Multiplexed in vivo Imaging Using PEGylated Upconversion Nanoparticles. Nano Research 2010, 3, 722-732.

14 Jiang GC, Pichaandi J, Johnson NJJ et al. An Effective Polymer Cross-Linking Strategy To Obtain Stable Dispersions of Upconverting NaYF4 Nanoparticles in Buffers and Biological Growth Media for Biolabeling Applications. Langmuir 2012, 28, 3239-3247.

15 Liu Q, Chen M, Sun Y et al. Multifunctional rare-earth self-assembled nanosystem for tri-modal upconversion luminescence/fluorescence/positron emission tomography imaging. Biomaterials 2011, 32, 8243-8253.

16 Liu Q, Li C, Yang T et al. "Drawing" upconversion nanophosphors into water through host-guest interaction. Chemical Communications 2010, 46, 5551-5553.

17 Fu L, Morsch M, Shi B et al. Versatile Upconversion Surface Evaluation Platform for Bio-nano Surface Selection for Nervous System. Nanoscale 2017.

18 Gnach A, Lipinski T, Bednarkiewicz A et al. Upconverting nanoparticles: assessing the toxicity. Chemical Society Reviews 2015, 44, 1561-1584.

Appendix I

6.1 Two wavelength modulation on high dopant upconversion nanocrystals

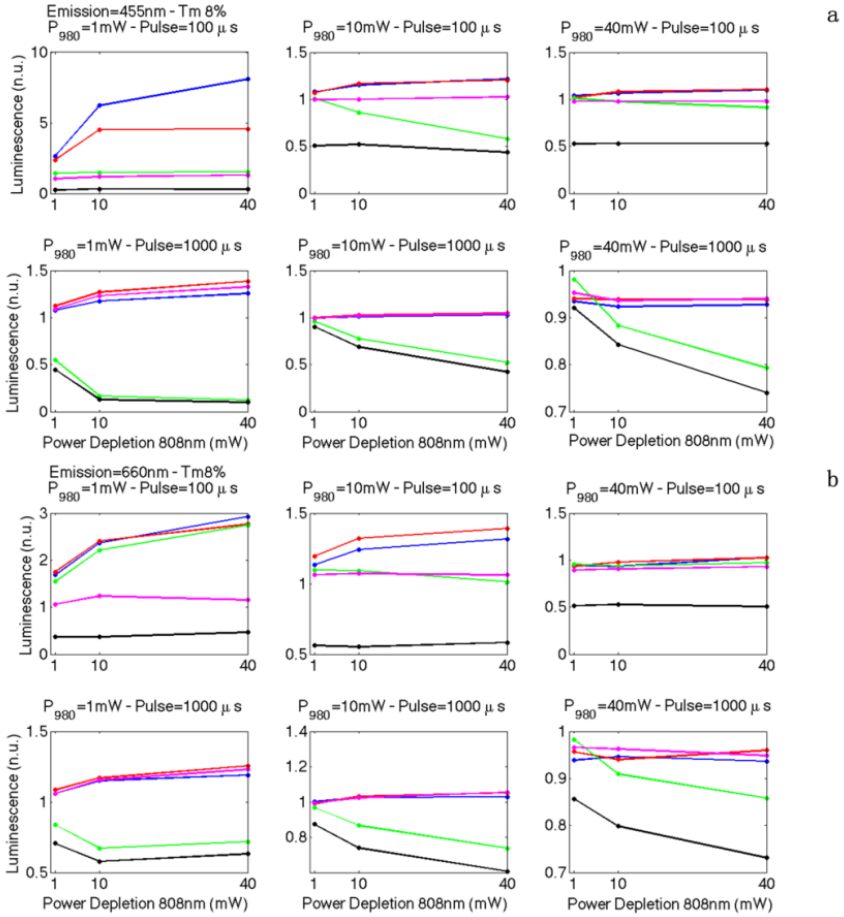

FIGURE 6-1 Luminescent peak intensity on $^1D_2$(a) and $^1G_4$(b) on 8% Tm^{3+} high dopant concentration nanocrystals under variable temporal delay condition between arrival of 808 nm and 980 nm pulses and different intensity conditions. Under 100 μs condition, blue:-100 μs; red:-50 μs; green: 0 μs; black: 50 μs; magenta: 100 μs; Under 1000 μs condition, blue:-1000 μs; red:-500 μs; green: 0 μs; black: 500 μs; magenta: 1000 μs

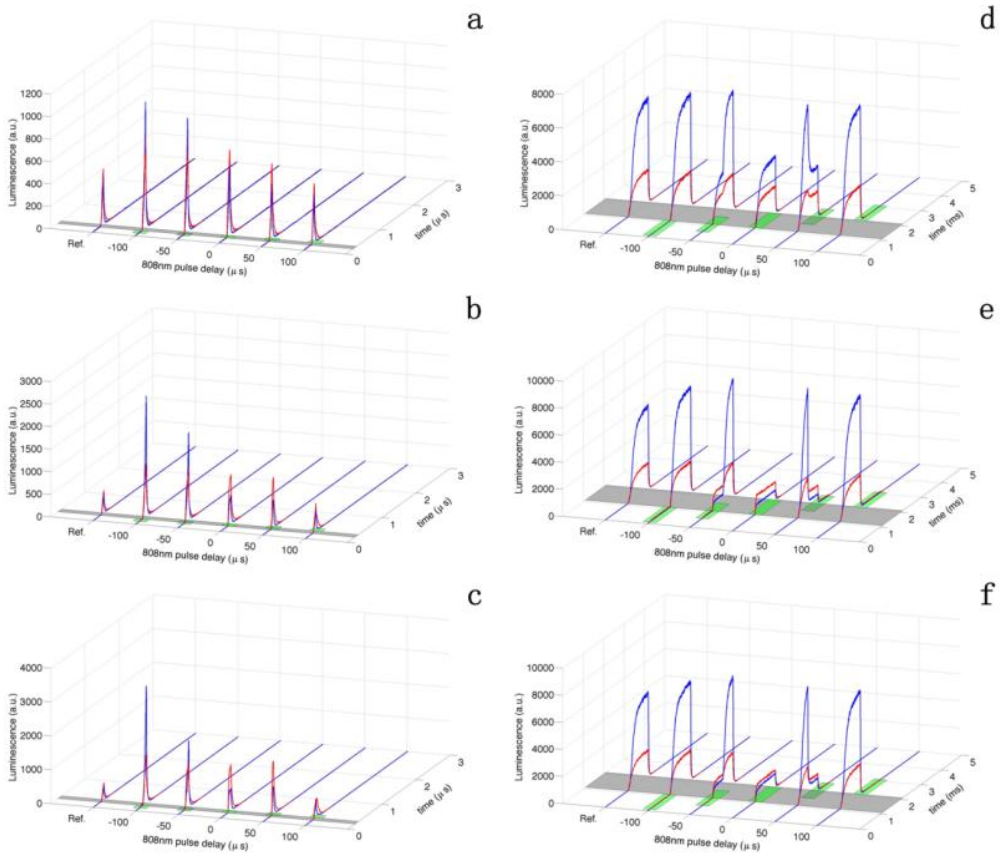

FIGURE 6-2 Transient responses of the $^1D_2$(blue curve) and $^1G_4$(red curve) emission from 8% Tm^{3+}-doped nanocrystals under synchronous illumination pulses of 980 nm and 808 nm. (a)(b)(c)The pulse duration time for 980 nm and 808 nm is 100 μs. And in the 3-D diagram, from left to right the temporal sequences for 808 nm are non-808 nm, ahead of 100 μs, ahead of 50 μs, totally overlapping, delayed 50 μs, delayed 100 μs, respectively; (d)(e)(f) The pulse duration time for 980 nm and 808 nm is 1000 μs. And in the 3-D diagram, from left to right the temporal sequences for 808 nm are non-808 nm, ahead of 1000 μs, ahead of 500 μs, totally overlapping, delayed 500 μs, delayed 1000 μs, respectively. The intensity of 980 nm is 0.6 MW/cm^2; (a)(d)The intensity of 808 nm is 0.76 MW/cm^2; (b)(e) The intensity of 808 nm is 7.57 MW/cm^2; (c)(f) The intensity of 808 nm is 30.3 MW/cm^2. Grey bar indicates the modulation period of 980 nm and green bar indicates the modulation period of 808 nm

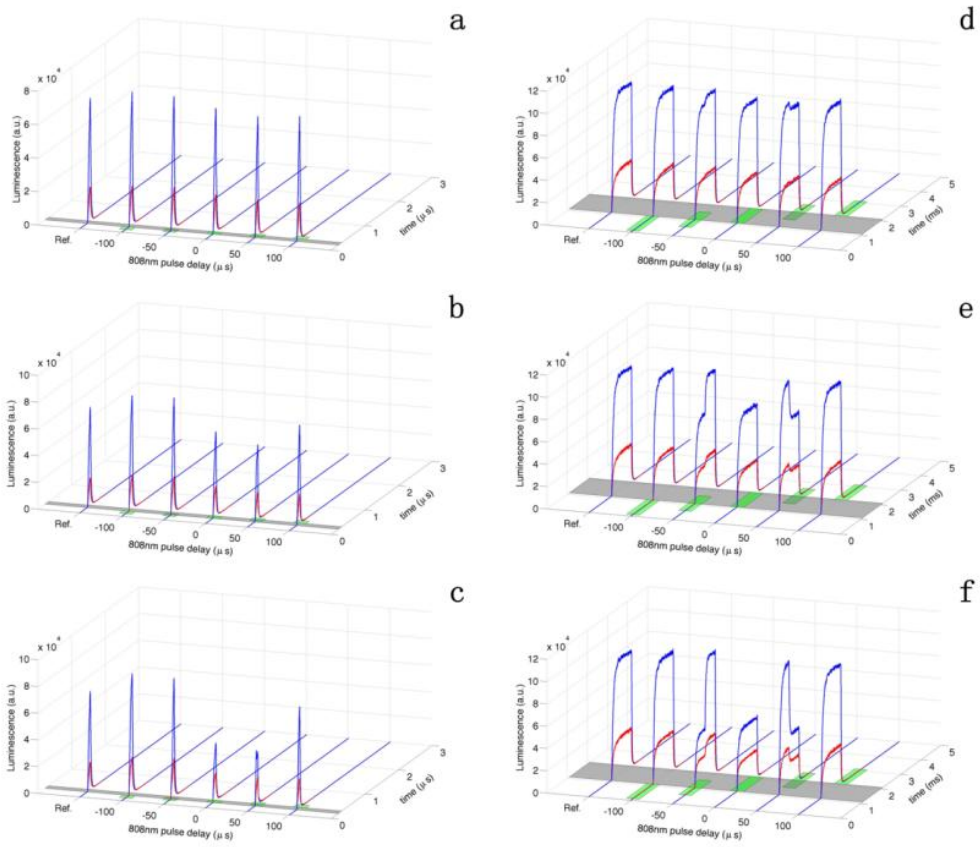

FIGURE 6-3 Transient responses of the $^1D_2$(blue curve) and $^1G_4$(red curve) emission from 8% Tm^{3+}-doped nanocrystals under synchronous illumination pulses of 980 nm and 808 nm. (a)(b)(c)The pulse duration time for 980 nm and 808 nm is 100 μs. And in the 3-D diagram, from left to right the temporal sequences for 808 nm are non-808 nm, ahead of 100 μs, ahead of 50 μs, totally overlapping, delayed 50 μs, delayed 100 μs, respectively; (d)(e)(f) The pulse duration time for 980 nm and 808 nm is 1000 μs. And in the 3-D diagram, from left to right the temporal sequences for 808 nm are non-808 nm, ahead of 1000 μs, ahead of 500 μs, totally overlapping, delayed 500 μs, delayed 1000 μs, respectively. The intensity of 980 nm is 6 MW/cm^2; (a)(d)The intensity of 808 nm is 0.76 MW/cm^2; (b)(e) The intensity of 808 nm is 7.57 MW/cm^2; (c)(f) The intensity of 808 nm is 30.3 MW/cm^2. Grey bar indicates the modulation period of 980 nm and green bar indicates the modulation period of 808 nm

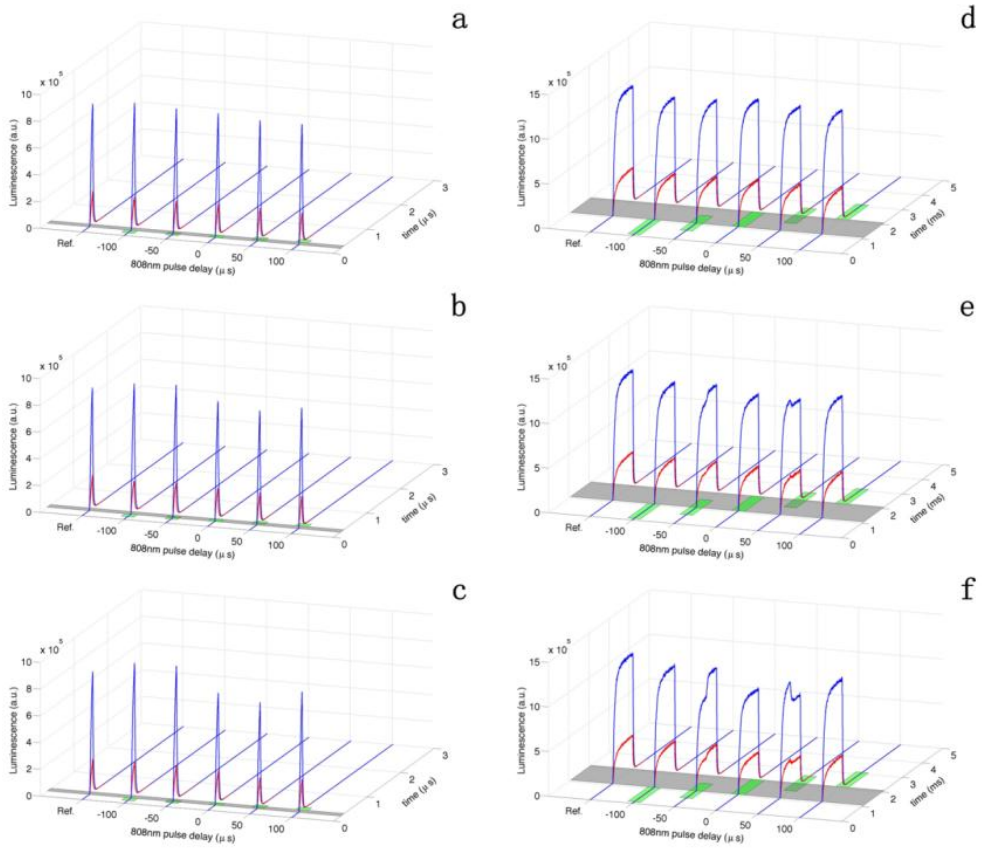

FIGURE 6-4 Transient responses of the $^1D_2$(blue curve) and $^1G_4$(red curve) emission from 8% Tm^{3+}-doped nanocrystals under synchronous illumination pulses of 980 nm and 808 nm. (a)(b)(c)The pulse duration time for 980 nm and 808 nm is 100 μs. And in the 3-D diagram, from left to right the temporal sequences for 808 nm are non-808 nm, ahead of 100 μs, ahead of 50 μs, totally overlapping, delayed 50 μs, delayed 100 μs, respectively; (d)(e)(f) The pulse duration time for 980 nm and 808 nm is 1000 μs. And in the 3-D diagram, from left to right the temporal sequences for 808 nm are non-808 nm, ahead of 1000 μs, ahead of 500 μs, totally overlapping, delayed 500 μs, delayed 1000 μs, respectively. The intensity of 980 nm is 24 MW/cm^2, (a)(d)The intensity of 808 nm is 0.76 MW/cm^2; (b)(e) The intensity of 808 nm is 7.57 MW/cm^2; (c)(f) The intensity of 808 nm is 30.3 MW/cm^2. Grey bar indicates the modulation period of 980 nm and green bar indicates the modulation period of 808 nm

6.2 Two wavelength modulation on low dopant upconversion nanocrystals

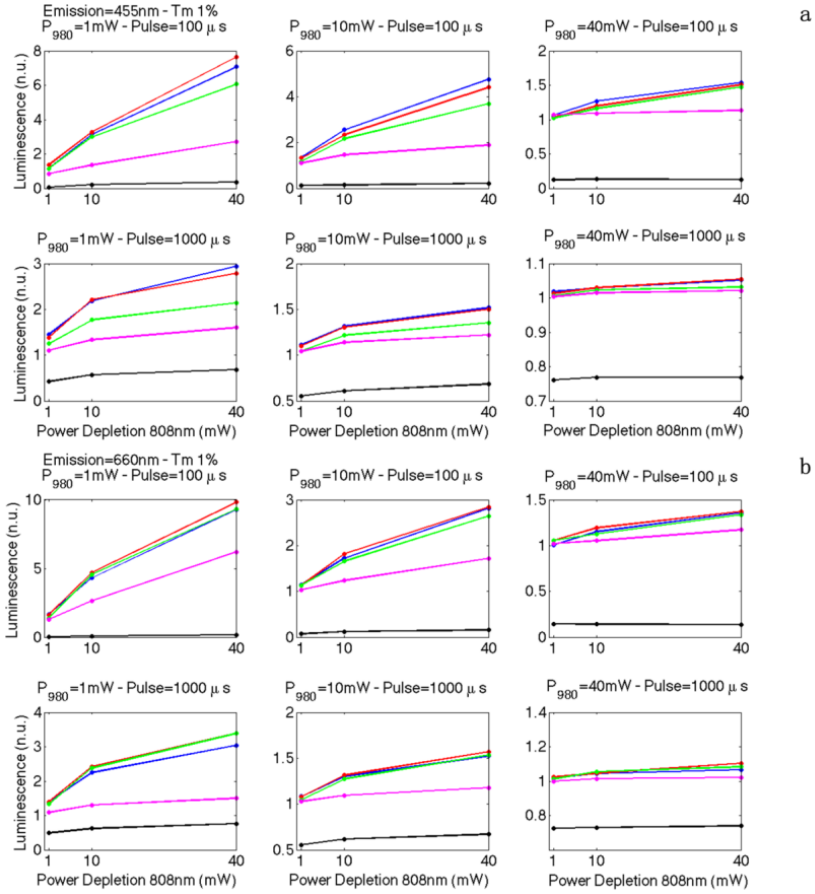

FIGURE 6-5 Luminescent peak intensity on $^1D_2$(a) and $^1G_4$(b) on 1% Tm^{3+} low dopant concentration nanocrystals under variable temporal delay condition between arrival of 808 nm and 980 nm pulses and different intensity conditions. Under 100 μs condition, blue:-100 μs; red:-50 μs; green: 0 μs; black: 50 μs; magenta: 100 μs; Under 1000 μs condition, blue:-1000 μs; red:-500 μs; green: 0 μs; black: 500 μs; magenta: 1000 μs

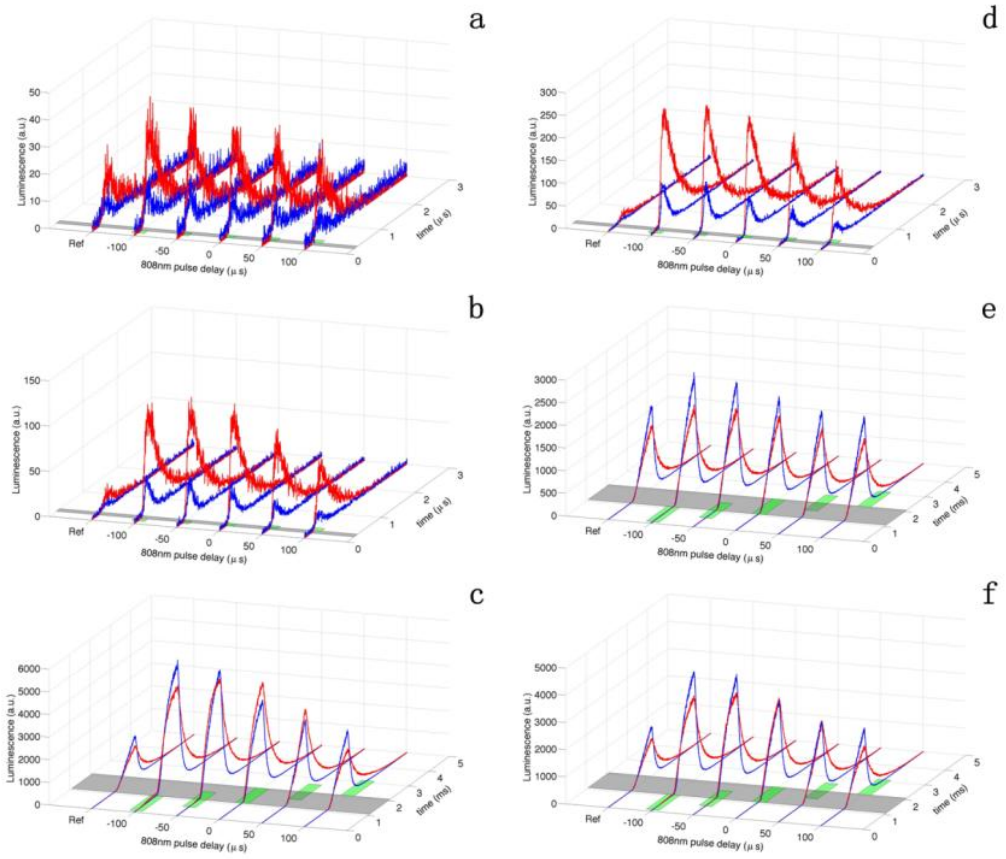

FIGURE 6-6 Transient responses of the $^1D_2$(blue curve) and $^1G_4$(red curve) emission from 1% Tm^{3+}-doped nanocrystals under synchronous illumination pulses of 980 nm and 808 nm. (a)(b)(c)The pulse duration time for 980 nm and 808 nm is 100 μs. And in the 3-D diagram, from left to right the temporal sequences for 808 nm are non-808 nm, ahead of 100 μs, ahead of 50 μs, totally overlapping, delayed 50 μs, delayed 100 μs, respectively; (d)(e)(f) The pulse duration time for 980 nm and 808 nm is 1000 μs. And in the 3-D diagram, from left to right the temporal sequences for 808 nm are non-808 nm, ahead of 1000 μs, ahead of 500 μs, totally overlapping, delayed 500 μs, delayed 1000 μs, respectively. The intensity of 980 nm is 0.6 MW/cm^2; (a)(d)The intensity of 808 nm is 0.76 MW/cm^2; (b)(e) The intensity of 808 nm is 7.57 MW/cm^2; (c)(f) The intensity of 808 nm is 30.3 MW/cm^2. Grey bar indicates the modulation period of 980 nm and green bar indicates the modulation period of 808 nm

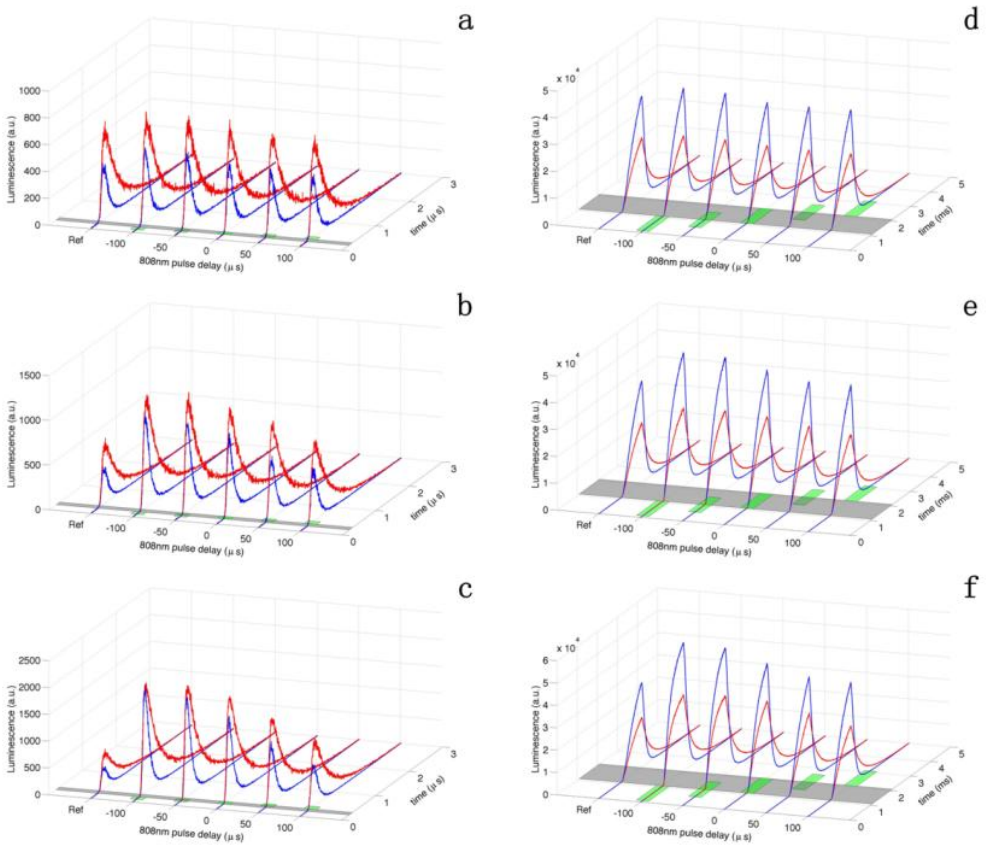

FIGURE 6-7 Transient responses of the $^1D_2$(blue curve) and $^1G_4$(red curve) emission from 1% Tm^{3+}-doped nanocrystals under synchronous illumination pulses of 980 nm and 808 nm. (a)(b)(c)The pulse duration time for 980 nm and 808 nm is 100 μs. And in the 3-D diagram, from left to right the temporal sequences for 808 nm are non-808 nm, ahead of 100 μs, ahead of 50 μs, totally overlapping, delayed 50 μs, delayed 100 μs, respectively; (d)(e)(f) The pulse duration time for 980 nm and 808 nm is 1000 μs. And in the 3-D diagram, from left to right the temporal sequences for 808 nm are non-808 nm, ahead of 1000 μs, ahead of 500 μs, totally overlapping, delayed 500 μs, delayed 1000 μs, respectively. The intensity of 980 nm is 6 MW/cm^2; (a)(d)The intensity of 808 nm is 0.76 MW/cm^2; (b)(e) The intensity of 808 nm is 7.57 MW/cm^2; (c)(f) The intensity of 808 nm is 30.3 MW/cm^2. Grey bar indicates the modulation period of 980 nm and green bar indicates the modulation period of 808 nm

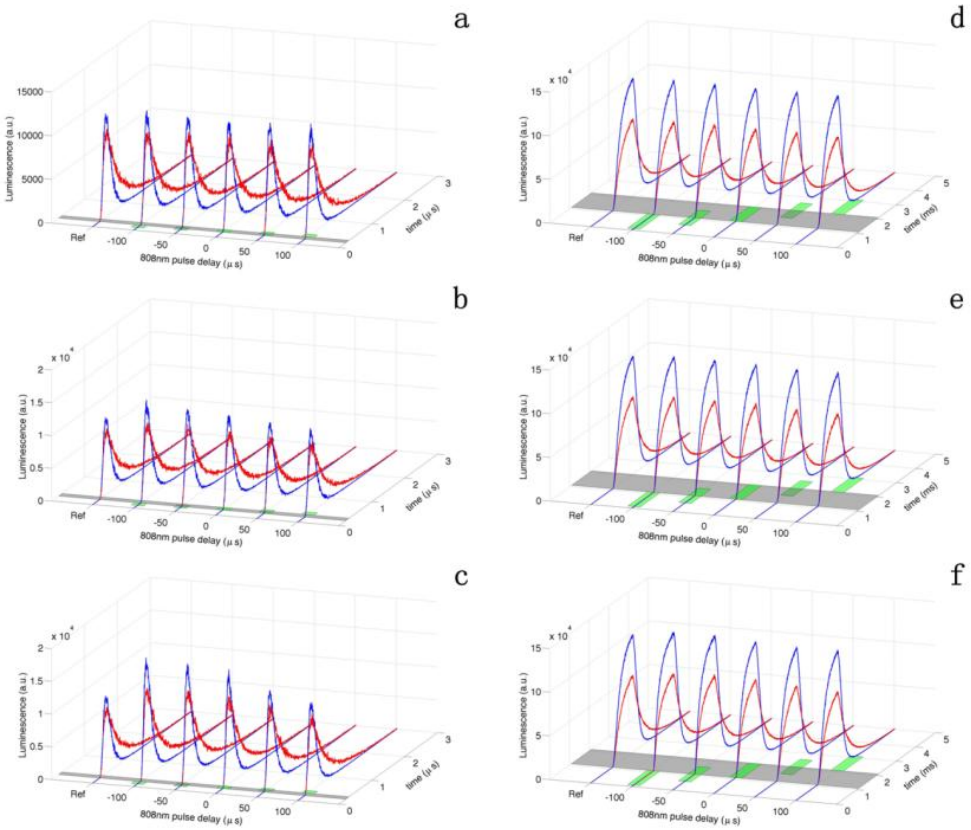

FIGURE 6-8 Transient responses of the $^1D_2$(blue curve) and $^1G_4$(red curve) emission from 1% Tm^{3+}-doped nanocrystals under synchronous illumination pulses of 980 nm and 808 nm. (a)(b)(c)The pulse duration time for 980 nm and 808 nm is 100 μs. And in the 3-D diagram, from left to right the temporal sequences for 808 nm are non-808 nm, ahead of 100 μs, ahead of 50 μs, totally overlapping, delayed 50 μs, delayed 100 μs, respectively; (d)(e)(f) The pulse duration time for 980 nm and 808 nm is 1000 μs. And in the 3-D diagram, from left to right the temporal sequences for 808 nm are non-808 nm, ahead of 1000 μs, ahead of 500 μs, totally overlapping, delayed 500 μs, delayed 1000 μs, respectively. The intensity of 980 nm is 24 MW/cm^2; (a)(d)The intensity of 808 nm is 0.76 MW/cm^2; (b)(e) The intensity of 808 nm is 7.57 MW/cm^2; (c)(f) The intensity of 808 nm is 30.3 MW/cm^2. Grey bar indicates the modulation period of 980 nm and green bar indicates the modulation period of 808 nm

Appendix II

7.1 Towards lifetime-based multiplexing super-resolution imaging – the preliminary results

7.1.1 Upconversion nanocrystals with tunable lifetimes

This section describes the temporal coding concept by exploring the lifetime properties of lanthanide-doped upconversion nanocrystals. We show that by changing the doping concentration, as well as the nanocrystal size and phase, the lifetime of upconversion nanocrystals can be precisely tuned in a large range from tens to several hundreds microsecond. We also developed a time-resolved confocal microscope that can decode lifetimes from individual upconversion nanocrystals, suggesting the possibility to create a new optical library of background-free, photo-stable and lifetime-tunable probes.

This work is presented as a published paper in the journal *Nature Photonics* in A.1.2. My contribution to the paper is to design and setup a single nanocrystal lifetime measurement confocal microscope, and to demonstrate the lifetime decoding on the selected Tm/Yb doped nanocrystals.

TABLE 7-1 Author contribution summary for Paper 3.

	Y. Lu	J. Z.	R. Z.	Y.Liu	D. L..	E.M. G.	X. Y.	P. X..	A. S.	J. L.	Y. S.	R.C. L.	Y. H.	J. S.	J.A. P.	J.P. R.	D. J.
Project design and management	•											•			•	•	•
System Setup	•			•													
Sample Preparation		•	•		•				•	•	•			•			
Data Collection	•	•		•			•										
Result Analysis	•			•				•					•				•
Manuscript and Figures	•	•	•			•											•

LETTERS
PUBLISHED ONLINE: 15 DECEMBER 2013 | DOI: 10.1038/NPHOTON.2013.322
nature photonics

Tunable lifetime multiplexing using luminescent nanocrystals

Yiqing Lu[1], Jiangbo Zhao[1], Run Zhang[1,2], Yujia Liu[1,3,4], Deming Liu[1], Ewa M. Goldys[1], Xusan Yang[3], Peng Xi[3], Anwar Sunna[2], Jie Lu[1,2], Yu Shi[1,2], Robert C. Leif[5], Yujing Huo[6], Jian Shen[7], James A. Piper[1], J. Paul Robinson[8] and Dayong Jin[1,2,8]*

Optical multiplexing plays an important role in applications such as optical data storage[1], document security[2], molecular probes[3,4] and bead assays for personalized medicine[5]. Conventional fluorescent colour coding is limited by spectral overlap and background interference, restricting the number of distinguishable identities. Here, we show that tunable luminescent lifetimes τ in the microsecond region can be exploited to code individual upconversion nanocrystals. In a single colour band, one can generate more than ten nanocrystal populations with distinct lifetimes ranging from 25.6 μs to 662.4 μs and decode their well-separated lifetime identities, which are independent of both colour and intensity. Such 'τ-dots' potentially suit multichannel bioimaging, high-throughput cytometry quantification, high-density data storage, as well as security codes to combat counterfeiting. This demonstration extends the optical multiplexing capability by adding the temporal dimension of luminescent signals, opening new opportunities in the life sciences, medicine and data security.

Multiplexing in biotechnology and life sciences refers to high-throughput technologies capable of simultaneous identification and quantification of multiple distinctive species[6–15]. Multiplexing molecular diagnostics impacts broadly on the bioinformatics areas of genomics[16,17], proteomics[18], metabolomics[19], cytomics[15] and personalized medicine[5,20], where personal gene expression profiling holds promise for individually targeted therapies. In data storage, the main goal of multiplexing is to increase the data storage capacity within spatially limited memory elements[1,21]. In security printing of banknotes, identity cards, trademark tags and so on, it helps to prevent forgery, tampering or counterfeiting, and thermochromatic, magnetic, multicolour fluorescent and optically variable colour-changing inks have been used for this purpose[2]. Multiplexing typically requires a matrix of optical codes, ideally carried by nano-/micro-sized objects, each of which should be accurately identifiable at high speed and in a low-cost fashion.

Fluorescence colour codes used in a broad range of fields have been one of the most popular methods for multiplexing. As one example, cytometry combined with fluorescence staining has been at the frontier of rapid detection of single cells for the last several decades. However, the crowded spectral domain limits the modern multi-colour flow cytometry to fewer than 20 channels, requiring three to five lasers, tens of filters and up to 20 light detectors[22]. The unavoidable spectral overlap requires complicated and tedious colour compensations. Thus, the outstanding challenge in multiplexing is to find ways of creating additional distinguishable coding dimensions, such as mass spectra[15], fluorescence lifetime[23] and Raman spectra[24]. These new dimensions become highly useful when the new identities can be accurately decoded (detected) by a simple, rapid and low-cost device.

In this Letter, we report a new multiplexing concept by manipulating the luminescence decay lifetimes to create a temporal coding dimension in a wide microsecond-to-millisecond range. Among typical materials that emit such long-lived luminescence, rare-earth doped luminescent nanocrystals are attracting significant attention with their applications in sensing, bioimaging, nanomedicine, solar cells and three-dimensional displays[25]. Recent advances in the synthesis of rare-earth doped upconversion nanocrystals, in particular, have led to accurate control of composite, crystal phase, morphology and emission colours[26]. Here, we have developed an approach to precisely tune the micro-/millisecond luminescence decays and produce individual populations of rare-earth doped nanocrystals with distinct lifetimes. Our results constitute a new optical coding and decoding dimension, which broadens the application of upconversion materials in nanoscale photonics.

Our lifetime multiplexing concept based on the tunability of lifetimes has been implemented following a simple scheme of co-doping sensitizer Yb^{3+} ions and blue-emitting Tm^{3+} ions at stepwise varied concentrations into the $NaYF_4$ nanocrystals (Supplementary Section 1.1). In this case, energy transfer from the sensitizer to the emitter ion at varying sensitizer–emitter distances provides lifetime tunability (Fig. 1). By using this approach we have been able to tune the lifetime of 40 nm $NaYF_4$:Yb,Tm nanocrystals in the blue emission band from 48 μs (4 mol% Tm) to 668 μs (0.2 mol% Tm). Thanks to the photostability of the nanocrystals and the background-free advantage of time-resolved detection, our purpose-built time-resolved confocal scanning system (Supplementary Sections 2.1 and 2.2) achieved a sufficiently high signal-to-background ratio (over 10^2) for lifetime measurement of a single nanocrystal's emission at 475 nm. Figure 1 shows confocal images of five typical groups of lifetime-encoded Tm-doped 'τ-dots', using pseudocolour to map the luminescence lifetime for each pixel.

These τ-dots emit luminescence in the microsecond range, about three orders of magnitude longer than the background autofluorescence (less than 10 ns), which can be easily suppressed through time-resolved measurements. We took advantage of this background-free readout for the rapid detection of single cells with our time-gated orthogonal scanning automated microscopy (OSAM)

[1]Advanced Cytometry Laboratories, MQ Photonics Research Centre and MQ BioFocus Research Centre, Macquarie University, Sydney, New South Wales 2109, Australia, [2]Department of Chemistry and Biomolecular Sciences, Macquarie University, Sydney, New South Wales 2109, Australia, [3]Department of Biomedical Engineering, College of Engineering, Peking University, Beijing 100871, China, [4]School of Biomedical Engineering, Shanghai Jiao Tong University, Shanghai, China, [5]Newport Instruments, 3345 Hopi Place, San Diego, California 92117-3516, USA, [6]Department of Electronic Engineering, Tsinghua University, Beijing 100084, China, [7]Olympus Australia, 82 Waterloo Road, North Ryde, New South Wales 2113, Australia, [8]Purdue University Cytometry Laboratories, Bindley Bioscience Center, Purdue University, West Lafayette, Indiana 47907, USA. *e-mail: dayong.jin@mq.edu.au

NATURE PHOTONICS DOI: 10.1038/NPHOTON.2013.322 LETTERS

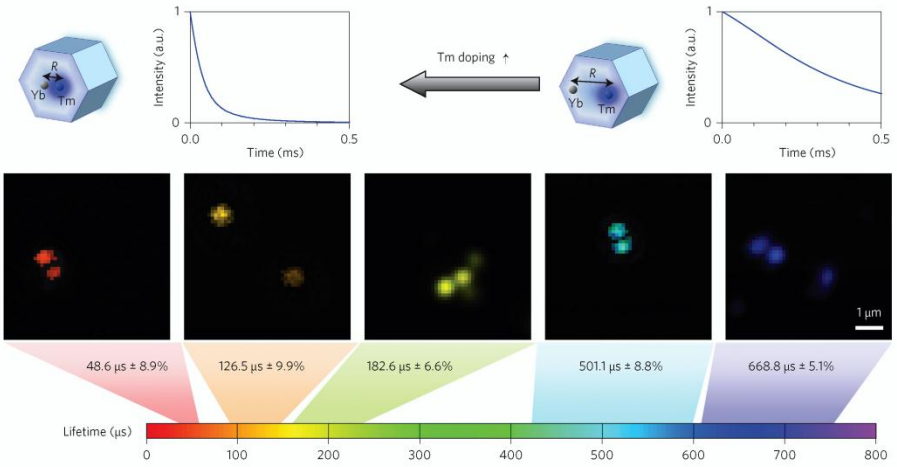

Figure 1 | Lifetime tuning scheme and time-resolved confocal images for $NaYF_4$:Yb,Tm upconversion nanocrystals. Each pixel was excited for 200 µs, followed by a delayed detection window of up to 3.8 ms to record its time-gated luminescence decay (40 ms exposure time to allow 10 times integration). The colour tone (hue) for each pixel represents its lifetime value decoded from the decay curve. The nanocrystals in the images from left to right have Tm doping concentrations of 4, 2, 1, 0.5 and 0.2 mol%, respectively, as well as 20 mol% Yb dopants.

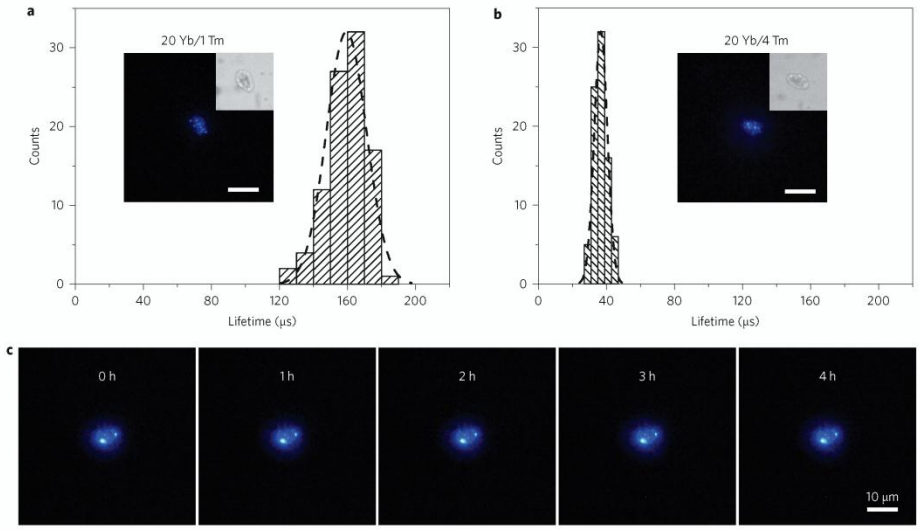

Figure 2 | Results for τ-dots-labelled *Giardia* cysts measured by the time-resolved scanning cytometry system. a,**b**, Lifetime histograms obtained from cysts labelled with different lifetime-encoded τ-dots (Yb/Tm co-doping concentration (mol%:mol%) of 20:1 for **a** and 20:4 for **b**). The scanning cytometry allows retrieval of each individual target cyst for luminescence as well as bright-field imaging confirmation. **c**, Typical recorded luminescence images for the same cyst under 4 h continuous laser excitation. All images were captured with a 100 ms exposure time.

platform[27], which was further developed to a next-generation time-resolved scanning cytometry system (Supplementary Section 2.3). The τ-dots with lifetime codes were surface-functionalized (Supplementary Sections 1.3 and 3), enabling bioconjugation to a number of different antibodies for simultaneously probing multiple rare-event pathogens (for example, *Giardia lamblia*, *Escherichia coli*

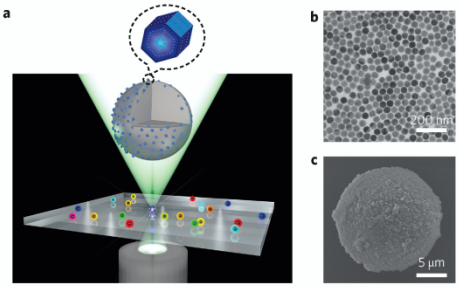

Figure 3 | Concept of τ-dots-encoded microspheres as the lifetime multiplexing suspension arrays. a, The synthesized monodispersed Tm upconversion nanocrystals can be embedded into the shell of porous microspheres, which can be decoded by the time-resolved scanning cytometry system, for example. **b**,**c**, Typical TEM image of the nanocrystals (**b**) and SEM image of a microsphere incorporating the nanocrystals (**c**).

O157:H7 and *Cryptosporidium parvum*) in beverages, food or within the hospital environment, in an effort to prevent disease or infection. Figure 2 presents a simple demonstration of two populations of *G. lamblia* cysts labelled with 1 mol% Tm τ-dots with a lifetime of ~160 μs and 4 mol% Tm τ-dots with a lifetime of ~40 μs (Supplementary Section 4.1), which were rapidly scanned using the time-resolved scanning cytometry system. The lifetime parameters yielded narrow population distributions (coefficients of variation (CVs) < 10%), offering superior detection accuracy and system simplicity compared with conventional high-throughput cytometry systems, which currently suffer from both crowded colours and fluctuating intensities. This result suggests the feasibility of 'digital cytometry' based on lifetime codes, without colour/intensity compensation requirements. The recorded τ-dots-stained *Giardia* images, over hours of continuous illumination, show no observable photobleaching effects (Fig. 2c). Moreover, our water-soluble τ-dots functionalized by different surface groups maintain their lifetime features across different biological application media (Supplementary Section 5) and intracellular environments (Supplementary Section 4.2). Small τ-dots can also be produced with sizes as small as ~10 nm (Supplementary Section 1.2). These results indicate that our lifetime-encoded τ-dots comprise robust labelling materials for bioimaging.

The τ-dots also relax the multiplexing constraints in suspension arrays, where the ensembles of microspheres are currently limited to only 100 colour- and intensity-coded channels (ten intensity levels at two colour emission bands)[28,29]. We have been able to create a new matrix of lifetime-coded microspheres by simply absorbing the as-prepared nanocrystals onto the shell of porous polystyrene microspheres (Fig. 3 and Supplementary Section 6). Both the lifetime and intensity of individual microspheres have been recorded during rapid scanning by our time-resolved scanning cytometry system. As shown in Fig. 4a, the emitter (Tm) variation within the range 0.2–8 mol% (with the sensitizer Yb fixed at 20 mol% and a nanocrystal size of ~40 nm) resulted in a remarkably large range of lifetimes from 25.6 μs to 662.4 μs in the blue band. Increasing the Yb concentration from 10 to 30 mol% (for Tm fixed at 1 mol% and nanocrystal size at ~40 nm) also significantly accelerated the blue emission decay from 206.7 μs to 120.2 μs.

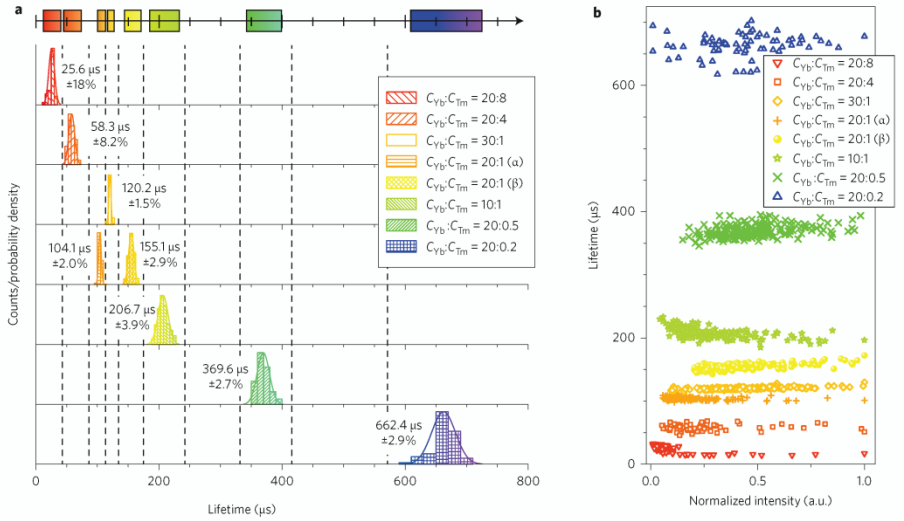

Figure 4 | Results for τ-dots-encoded populations of microspheres carrying unique lifetime identities. a, The mechanism of upconversion energy transfer, by adjusting the co-dopant concentration of the sensitizer/emitter, can generate eight lifetime populations of microspheres in the Tm blue-emission band. Symbols α and β represent cubic and hexagonal crystal phases, respectively. The numeral besides each histogram is the mean lifetime±lifetime CV from Gaussian distribution fitting. The blocks in the axis above represent the lifetime resources (±3σ) occupied by each population. The open spaces suggest more populations could be engineered. **b**, Two-dimensional (intensity versus lifetime) scattered plots showing that all lifetime populations are independent of the intensities of individual microcarriers.

NATURE PHOTONICS DOI: 10.1038/NPHOTON.2013.322 LETTERS

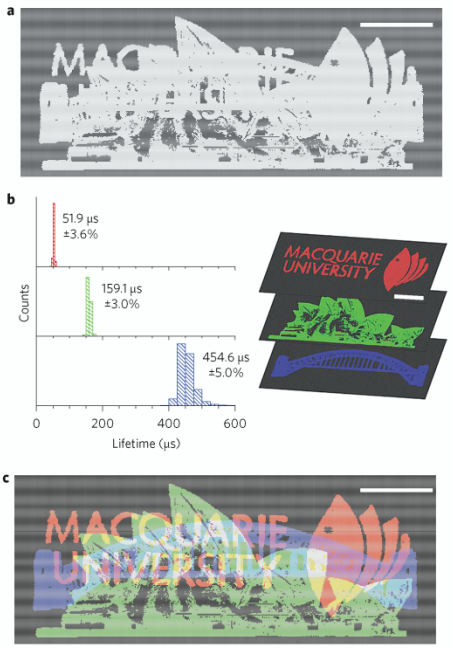

Figure 5 | Demonstration of lifetime-encoded document security and photonic data storage. a–c, Three overlapping patterns are printed with different Tm τ-dots: (C_{Yb}:C_{Tm}) 20:4 for the 'Macquarie University' logo, 20:1 for the Sydney Opera House image, and 20:0.5 for the Sydney Harbour Bridge image. Intensity-based luminescence imaging only gives a complex picture (**a**), but time-resolved scanning separates the patterns based on the lifetime components of every pixel (**b**), so that genuine multiplexing information contained in the same overlapping space of the document can be decoded (**c**; pseudocolour is used to indicate the luminescence lifetime for each pixel). Scale bars (all images), 5 mm.

We also found that cubic-phase crystals typically yield shorter lifetimes than the hexagonal phase due to an increased level of crystal defects and internal quenching[30,31]. By using this approach we have been able to tune the lifetime of 20 Yb/1 Tm (mol%/mol%) nanocrystals from 155.1 µs (40 nm in the hexagonal phase) to 104.1 µs (10 nm in the cubic phase). Interestingly, for each of these population groups, even though the intensity varies across two orders of magnitude (Fig. 4b), the lifetime CV can be as low as 1.5% (at most 3.9% for most populations other than the two with the shortest lifetimes, which have slightly larger CVs due to the small average values). These results show that the lifetime codes are independent of intensity, and therefore require no compensation, a further overwhelming advantage over the spectral-domain cytometry method. The narrow CVs helped us realize at least eight completely separate lifetime channels in the blue band, and there is sufficient potential for a total of ten channels or more (note the large gaps among the last three populations). We also synthesized core–shell nanocrystals with further increased lifetime values. For example, by coating our τ-dots with an inert shell, a thin layer of undoped $NaYF_4$ crystal structure (Supplementary Section 1.4), we significantly extended the typical lifetime of 20 Yb/0.5 Tm nanocrystals by ~32% (Supplementary Table 3).

The purpose-engineered multiplexing τ-dots carrying distinguishable lifetime codes will have further impact in the area of photonics, in particular for high-capacity data storage and data security, adding to the other optical dimensions currently available such as wavelength and polarization, as well as spatial dimensions. Figure 5 presents a blended picture superimposed by three overlapping images printed with τ-dots with Yb:Tm ratios of 20:4, 20:1 and 20:0.5 (mol%:mol%), respectively (Supplementary Section 7). Although normal luminescence colour imaging does not show what is concealed in the blended picture (Fig. 5a), our time-resolved scanning cytometry clearly decodes it into three individual images as a result of them having distinct lifetimes of 52, 159 and 455 µs (Fig. 5b). This result forms the basis for a new type of document encryption with our τ-dots as security inks; only authorized individuals who know the correct decoding rule of the luminescence lifetimes are able to access the secret information. Furthermore, a regular arrangement of such nanomaterials into submicrometre-scale units provides a new option for high-density data storage using lifetimes as digits. In particular, the presence/absence of one lifetime component can be used as one binary digit, allowing an 8-bit capacity to be achieved for each unit by simply using three types of lifetime-encoded τ-dots of the same colour. In either case, one outstanding virtue of our method is that the complexity of the decoding system is not increased, because no additional light sources, filters or detectors are required.

Based on the above demonstrations, we confirmed that the τ-dots-powered lifetime multiplexing method in the microsecond region has several significant advantages. (1) Multiple physical mechanisms with robust engineering capability can be used to fine-tune and create a series of distinguishable lifetime features without observable crosstalk between different channels (Supplementary Section 8). (2) Multiple emitters in a τ-dot provide non-bleaching and non-blinking luminescence to stabilize the lifetime feature across different application media, which is ideal for long-term tracking of multiplexed single τ-dots. (3) Time-resolved detection of exceptionally long luminescence in the microsecond domain completely eliminates any autofluorescence background from usually complex biological samples or embedding substrates. (4) Unlike fluorescence colours, the decoding of the luminescence lifetimes is independent of absolute intensity, so it is more tolerant of ambient background, electronic noise and varying collection efficiencies, as well as possible chromatic aberration associated with optical defocusing. (5) It is compatible with fluorescence lifetime imaging microscopy (FLIM)[32,33]; the amplified bright luminescence from single τ-dots and objects stained with them enables direct tracking of multiple photons for rapid lifetime measurement (Supplementary Section 2.1), which in the imaging perspective suggests a microsecond-to-millisecond region FLIM powered by our tunable τ-dots. (6) The upconversion τ-dots can absorb (stepwise) two or more low-energy photons, thus only requiring low-cost infrared diode excitation, so decoding instrumentation can be as simple as one laser diode and a single-element photodetector.

In summary, we have successfully demonstrated a new temporal-domain approach to multiplexing. We have introduced a family of nanotags as well as microcarriers with separate lifetime identities independent of colour and intensity. These were decoded without observable crosstalk. This work lays the foundation for future libraries of nano-/microprobes carrying more than 10,000 distinguishable codes (via a combination of colour, intensity and lifetime), unlocking the hidden potential of luminescence as a powerful analytical technique able to cope with the complexity challenges in life sciences and medicine. It also opens new

opportunities for high-density data storage as well as document security against forgery.

Received 16 May 2013; accepted 31 October 2013; published online 15 December 2013

References

1. Zijlstra, P., Chon, J. W. M. & Gu, M. Five-dimensional optical recording mediated by surface plasmons in gold nanorods. *Nature* **459,** 410–413 (2009).
2. Jeevan, M. M. *et al.* Security printing of covert quick response codes using upconverting nanoparticle inks. *Nanotechnology* **23,** 395201 (2012).
3. Li, Y. G., Cu, Y. T. H. & Luo, D. Multiplexed detection of pathogen DNA with DNA-based fluorescence nanobarcodes. *Nature Biotechnol.* **23,** 885–889 (2005).
4. Lin, C. X. *et al.* Submicrometre geometrically encoded fluorescent barcodes self-assembled from DNA. *Nature Chem.* **4,** 832–839 (2012).
5. Lu, J. *et al.* MicroRNA expression profiles classify human cancers. *Nature* **435,** 834–838 (2005).
6. Schena, M., Shalon, D., Davis, R. W. & Brown, P. O. Quantitative monitoring of gene-expression patterns with a complementary-DNA microarray. *Science* **270,** 467–470 (1995).
7. Thomson, J. M., Parker, J., Perou, C. M. & Hammond, S. M. A custom microarray platform for analysis of microRNA gene expression. *Nature Methods* **1,** 47–53 (2004).
8. Nicewarner-Pena, S. R. *et al.* Submicrometer metallic barcodes. *Science* **294,** 137–141 (2001).
9. Pregibon, D. C., Toner, M. & Doyle, P. S. Multifunctional encoded particles for high-throughput biomolecule analysis. *Science* **315,** 1393–1396 (2007).
10. Braeckmans, K. *et al.* Encoding microcarriers by spatial selective photobleaching. *Nature Mater.* **2,** 169–173 (2003).
11. Han, M. Y., Gao, X. H., Su, J. Z. & Nie, S. Quantum-dot-tagged microbeads for multiplexed optical coding of biomolecules. *Nature Biotechnol.* **19,** 631–635 (2001).
12. Wang, F. *et al.* Tuning upconversion through energy migration in core-shell nanoparticles. *Nature Mater.* **10,** 968–973 (2011).
13. Cunin, F. *et al.* Biomolecular screening with encoded porous-silicon photonic crystals. *Nature Mater.* **1,** 39–41 (2002).
14. Cao, Y. W. C., Jin, R. C. & Mirkin, C. A. Nanoparticles with Raman spectroscopic fingerprints for DNA and RNA detection. *Science* **297,** 1536–1540 (2002).
15. Bendall, S. C. *et al.* Single-cell mass cytometry of differential immune and drug responses across a human hematopoietic continuum. *Science* **332,** 687–696 (2011).
16. Lander, E. S. *et al.* Initial sequencing and analysis of the human genome. *Nature* **409,** 860–921 (2001).
17. Bartel, D. P. MicroRNAs: genomics, biogenesis, mechanism, and function. *Cell* **116,** 281–297 (2004).
18. Pawson, T. & Nash, P. Assembly of cell regulatory systems through protein interaction domains. *Science* **300,** 445–452 (2003).
19. Nicholson, J. K. & Lindon, J. C. Systems biology—metabonomics. *Nature* **455,** 1054–1056 (2008).
20. Van't Veer, L. J. & Bernards, R. Enabling personalized cancer medicine through analysis of gene-expression patterns. *Nature* **452,** 564–570 (2008).
21. Li, X., Lan, T.-H., Tien, C.-H. & Gu, M. Three-dimensional orientation-unlimited polarization encryption by a single optically configured vectorial beam. *Nature Commun.* **3,** 998 (2012).
22. Perfetto, S. P., Chattopadhyay, P. K. & Roederer, M. Seventeen-colour flow cytometry: unravelling the immune system. *Nature Rev. Immunol.* **4,** 648–655 (2004).
23. Cui, H. H., Valdez, J. G., Steinkamp, J. A. & Crissman, H. A. Fluorescence lifetime-based discrimination and quantification of cellular DNA and RNA with phase-sensitive flow cytometry. *Cytometry A* **52A,** 46–55 (2003).
24. Watson, D. A. *et al.* A flow cytometer for the measurement of Raman spectra. *Cytometry A* **73A,** 119–128 (2008).
25. Gnach, A. & Bednarkiewicz, A. Lanthanide-doped up-converting nanoparticles: merits and challenges. *Nano Today* **7,** 532–563 (2012).
26. Wang, F. *et al.* Simultaneous phase and size control of upconversion nanocrystals through lanthanide doping. *Nature* **463,** 1061–1065 (2010).
27. Lu, Y., Xi, P., Piper, J. A., Huo, Y. & Jin, D. Time-gated orthogonal scanning automated microscopy (OSAM) for high-speed cell detection and analysis. *Sci. Rep.* **2,** 837 (2012).
28. Yang, L., Tran, D. K. & Wang, X. BADGE, BeadsArray for the detection of gene expression, a high-throughput diagnostic bioassay. *Genome Res.* **11,** 1888–1898 (2001).
29. Yurkovetsky, Z. R. *et al.* Multiplex analysis of serum cytokines in melanoma patients treated with interferon-alpha 2b. *Clin. Cancer Res.* **13,** 2422–2428 (2007).
30. Wang, F., Wang, J. & Liu, X. Direct evidence of a surface quenching effect on size-dependent luminescence of upconversion nanoparticles. *Angew. Chem. Int. Ed.* **49,** 7456–7460 (2010).
31. Zhao, J. *et al.* Upconversion luminescence with tunable lifetime in $NaYF_4$:Yb,Er nanocrystals: role of nanocrystal size. *Nanoscale* **5,** 944–952 (2013).
32. Bastiaens, P. I. H. & Squire, A. Fluorescence lifetime imaging microscopy: spatial resolution of biochemical processes in the cell. *Trends Cell Biol.* **9,** 48–52 (1999).
33. Heilemann, M. *et al.* High-resolution colocalization of single dye molecules by fluorescence lifetime imaging microscopy. *Anal. Chem.* **74,** 3511–3517 (2002).

Acknowledgements

The authors thank D. Birch for sample characterization and F. Chi for technical assistance. This project was financially supported by the Australian Research Council (DP 1095465), the China Scholarship Council and Macquarie University Postgraduate Research Scholarships. Y.Lu and D.J. acknowledge the International Society for Advancement of Cytometry for support as ISAC Scholars. P.X. acknowledges support from the '973' programme of China (2011CB707502, 2011CB809101). D.J. and A.S. acknowledge support through Macquarie University Vice-Chancellor's Innovation Fellowships.

Author contributions

D.J., J.A.P., R.C.L. and J.P.R. conceived the project. D.J. designed the experiments and supervised the research. Y.Lu, J.Z. and D.J. were primarily responsible for data collection and analysis. Y.Lu, E.M.G. and D.J. prepared figures and wrote the main manuscript text. Y.Lu, J.Z., R.Z., D.L. and D.J. were primarily responsible for the Supplementary Information. All authors contributed to data analysis, discussions and manuscript preparation.

Additional information

Supplementary information is available in the online version of the paper. Reprints and permissions information is available online at www.nature.com/reprints. Correspondence and requests for materials should be addressed to D.J.

Competing financial interests

The authors declare no competing financial interests.

7.1.3 Lifetime decoding of mixed upconversion nanocrystals

While lifetime imaging on individual batches of upconversion nanocrystals has been realised without much difficulty, a new challenge is introduced for samples containing a mixture of lifetime-engineered nanocrystals. This is because more than one lifetime values need to be resolved from the potentially multi-exponential decay curves if two or more nanocrystals with different lifetime codes coincide within the optical resolution. Dr Yiqing Lu and I demonstrated lifetime decoding with mixed samples on the single nanocrystal level. The first measurement was carried on using three types of nanocrystals with different dopant concentration – the Yb^{3+} was fixed at 20%, and Tm^{3+} to be 1%, 4% and 8%, respectively. As shown in Fig 7-1a, from confocal scanning, the nanocrystals looked just the same due to the identical emission wavelength. While with lifetime decoding, the three different nanocrystals can be clearly distinguished.

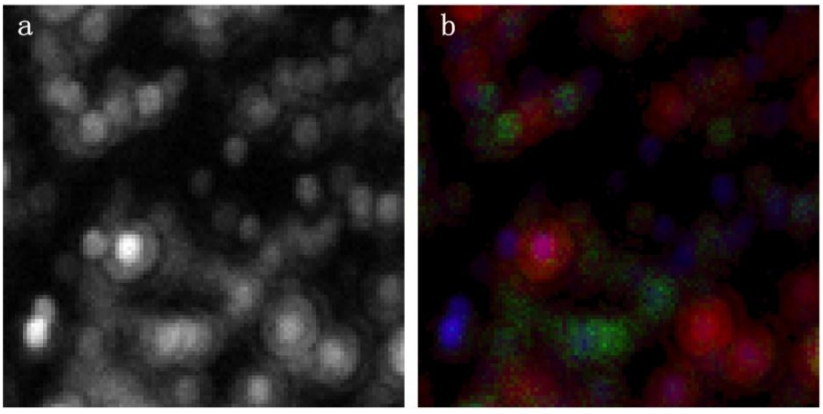

FIGURE 7-1 Demonstration of lifetime decoding mixed single nanocrystals sample. The sample was prepeared with three kinds of Tm^{3+}-doped upconversion nanocrystals. (a)Intensity-based confocal fluorescent imaging result on 455 nm emission; (b)Time-resolved scanning indicates the location of different nanocrystals based on the lifetime components. Pseudocolour is used to indicate the fluorescent lifetime for each nanocrystals. The red, green and blue color indicates the Tm^{3+} dopant concentration of 1%, 4% and 8%, respectively

We further carried on the measurement on five different nanocrystals with fixed 20% Yb^{3+} while Tm^{3+} of 0.2%,0.5%, 1%, 4%, 8% respectively, as shown in Fig 7-2.

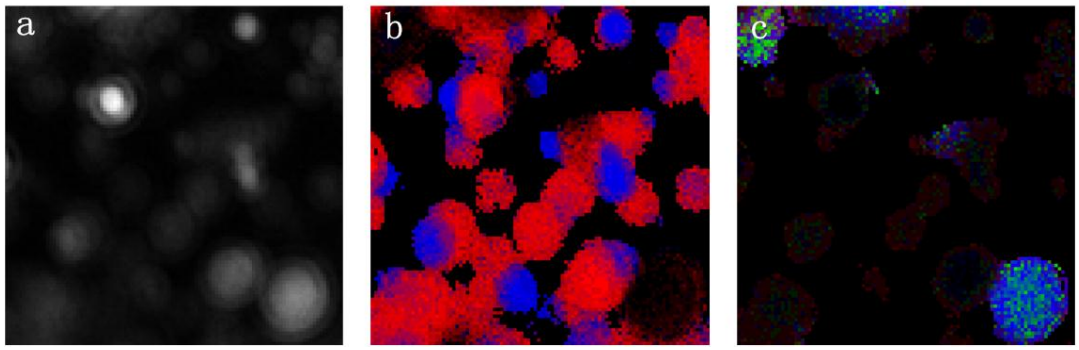

FIGURE 7-2 Demonstration of decoding single nanocrystals sample. Sample was prepeared with five kinds of Tm^{3+}-doped upconversion nanocrystals. Pseudocolour is used to indicate the fluorescent lifetime for each nanocrystals. (a)Intensity-based confocal fluorescent imaging result on 455 nm emission; (b)Time-resolved scanning indicates the location of two high dopant concentration nanocrystals based on the lifetime components. The blue and red color indicates the Tm^{3+} dopant concentration of 8% and 4%, respectively. (c)Time-resolved scanning indicates the location of three low dopant concentration nanocrystals based on the lifetime components. The blue, green and red color indicates the Tm^{3+} dopant concentration of 1%, 4% and 8%, respectively

We then carried on the similar experiments on binding of a target molecule on the beads. In our experiment, three kinds of upconversion nanocrystals doped with different Tm^{3+} concentrations of 1 mol%, 4 mol%, and 8 mol% were synthesized with their characterized lifetime values as 25.6 μs, 58.3 μs, and 206.7 μs, respectively. To functionalize these dots with capture DNA molecules, the nanocrystals were added into 300 μl chloroform, then mixed with 150 μl ultrapure H_2O solution containing 10 nmol pathogen DNA probes. After 2 hours incubation on a mixer, the upper layer solution was taken out and then centrifuged twice at 14000 rpm for 5 min. The final settlement was dissolved in ultrapure H_2O for pathogen DNAs detection. Each kind of nanocrystals has been conjugated with a pathogens DNA probe, including human immunodeficiency virus (HIV), Ebola virus (EV), and hepatitis B virus (HBV), so that the probe-functionalized nanocrystals will recognize and bind to their counterpart of specific target DNAs.

Streptavidin functionalized microspheres were prepared. 5 μL of 15 μm sized carboxylic microspheres (10% stock) were activated by 1-Ethyl-3-[3-dimethylaminopropyl] carbodiimide hydrochloride (EDC) in 2-(N-morpholino)ethanesulfonic acid buffer (MES, 50 nM, pH 6.0) for 15 min, and then incubated with 25 μg streptavidin for 2 hours at room temperature. The functionalized microspheres were harvested by centrifugation and then ready for target DNA capture.

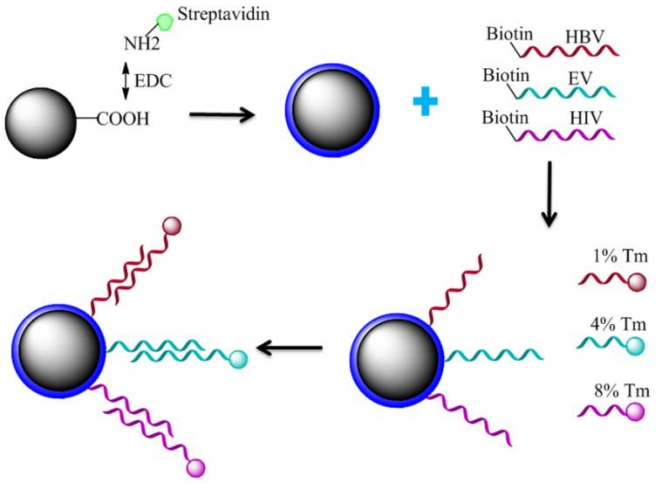

FIGURE 7-3 The schematic diagram of lifetime based reporter multiplexing detection of pathogen DNAs

Table 7-2 DNA sequences used in reporter multiplexing.

Name		DNA Sequence(5' to 3')*	Modification(5')
Capture Probe	HIV	TTT GGG *GTC ATG TTA TTC CAA ATA TCT*	Amino Modifier C12
	EV	TTT GGG *ATA CTG TTC TCC AAC ATT TAC*	
	HBV	TTT GGG *ATC ATC CAT ATA ACT GAA AGC*	
Target Probe	HIV	AGA *AGA TAT TTG GAA TAA CAT GAC*	Biotin
	EV	GGA *GTA AAT GTT GGA GAA CAG TAT*	
	HBV	TTG *GCT TTC AGT TAT ATG GAT GAT*	

The streptavidin coated microsphere was used to capture three different biotin modified pathogen DNAs including human immunodeficiency virus (HIV), Ebola virus (EV), hepatitis B virus (HBV) as shown in Table A-2 and Fig 7-3. Then the pathogen DNAs loaded microspheres were reacted with the probe conjugated Tm^{3+} Super dots in the 2 × saline-sodium citrate (SSC) hybridization buffer. After 2 hours reaction, the mixture was centrifuged twice at 8000 rpm for 5 min, and then the purified microspheres were spread into a slide for the lifetime measurement.

As shown in Fig 7-4, the lifetimes of single nanocrystal probes were resolved by the purpose-built time-resolved laser scanning microscope, indicating the presence of three pathogen DNAs on the microsphere surface. The red dots represent the HBV pathogen DNAs, the green dots represent EV pathogen DNAs, and the blue dots represent HIV pathogen DNAs. The NIR excitation and time-resolved detection with single nanoparticle sensitivity suggests the feasibility for quantitation of multiplexed nucleic acids in bead assay, which is not possible for conventional techniques.

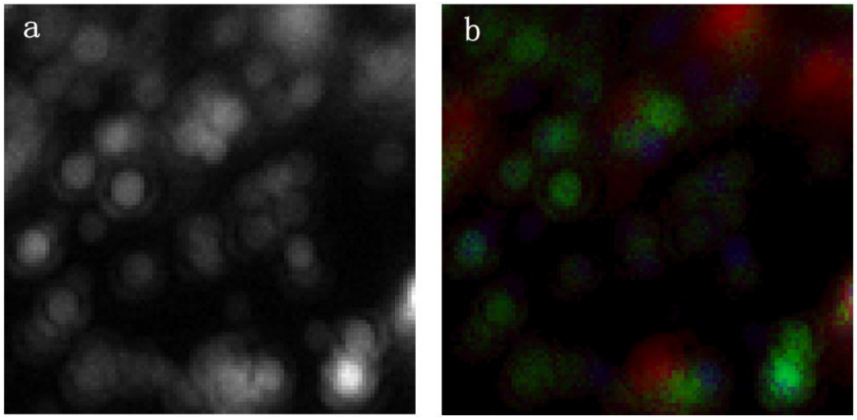

FIGURE 7-4 The time-resolved localization of lifetime-encoded SUPER dots on microsphere surface to detect pathogen DNAs. A). The fluorescence intensity of each single nanocrystal. B), The time-resolved distribution of different populations of lifetime-encoded nanocrystals, showing the presence of three pathogen DNAs on the microsphere surface. The scale bar is 100 nm. Pseudocolour is used to indicate the fluorescent lifetime for each nanocrystals. The red, green and blue color indicates the Tm^{3+} dopant concentration of 1%, 4% and 8%, respectively

7.1.4 Remarks

We have successfully demonstrated the capability of lifetime multiplexing using rare-earth upconversion nanocrystals. This offers the potential to apply lifetime multiplexing in STED to achieve super-resolution imaging on a number of lifetime channels, enabling simultaneous identification of separately labelled biological features at high throughput.